The Dissertation Committee for Seyed Omid Razavi Certifies that this is the approved version of the following dissertation:

Experimental Investigation of the Wellbore Strengthening Phenomenon

Committee:

Eric van Oort, Supervisor

Michael Engelhardt

Nicolas Espinoza

Jon Olson

Maša Prodanović

Experimental Investigation of the Wellbore Strengthening Phenomenon

by

Seyed Omid Razavi, B.Sc.; M.Sc.

Dissertation

Presented to the Faculty of the Graduate School of

The University of Texas at Austin

in Partial Fulfillment

of the Requirements

for the Degree of

Doctor of Philosophy

The University of Texas at Austin

August, 2016

Dedication

This dissertation is dedicated to my parents, Sussan and Mehran.

Acknowledgements

First and foremost, I would like to thank my supervisor, Prof. Dr. Eric van Oort. I appreciate all his contributions of time, ideas, and funding to make my PhD experience productive and stimulating. I am very grateful to Dr. Ali Karimi Vajargah for his scientific advice and knowledge and for many insightful discussions and suggestions. Appreciation is extended to the members of my PhD committee, Prof. Dr. Michael Engelhardt, Prof. Dr. Nicolas Espinoza, Prof. Dr. Jon Olson, and Prof. Dr. Maša Prodanović for their helpful advice and suggestions.

I would like to sincerely thank the lead sponsors of this joint industry project: ConocoPhillips and Schlumberger. The UT MudFrac equipment and the experiments done with it would not have been possible without an enabling donation by Schlumberger and the active involvement of Susan Rosenbaum and Jim Friedheim, to whom this project owes a great deal of gratitude. My very special thanks for their guidance and support go out to Dave Beardmore, Greg Mullen, Bob Pantermuehl, Gary Collins, Bret Borland, Ernie Onyia, Son Pham and Kyle Fontenot, either formerly or currently with ConocoPhillips; Jim Friedheim, Steve Young, and Quan Guo with Schlumberger. Additional financial support was provided by American Gilsonite Company, with special thanks to Dwight Strickland, Ted Stevens and Dario Montes.

I would like to thank the management and employees of Metarock Laboratories for their contribution in the design of the experimental set-up and technical support during the experiments. My special thanks go out to Munir Aldin, Robert Patterson, and Samir Aldin. Also, I acknowledge Greg Vardilos, Robert Joha, Sudarshan Govindarajan, Oswaldo Nunez, and David Ghobar for their help in conducting the experiments.

I thank Besmir "Bez" Buranaj Hoxha, Dr. Katy Aughenbaugh, and Dr. Sriramya Duddukuri Nair for their help in supplying the materials required for the experiments and preparing the drilling fluids. Tesse Smitherman is thanked for her considerable help with the administrative work. I also thank Jessica S. Holmes for editing parts of this dissertation.

In the end, I would like to thank my family. I thank Aunt Azam and Uncle Saeed for supporting me during my PhD. I am deeply grateful to my brother, Arvin, my mother, Sussan, and my father, Mehran, for their support, encouragement, and unconditional love.

Experimental Investigation of the Wellbore Strengthening Phenomenon

Seyed Omid Razavi, PhD

The University of Texas at Austin, 2016

Supervisor: Eric van Oort

An experimental approach was employed to study the Wellbore Strengthening (WBS) phenomenon. A state-of-the-art experimental set-up was designed to carry out high-pressure borehole fracturing tests on cylindrical rock samples. The experimental set-up offers full control over borehole, confining, and pore pressures. Fracturing experiments were conducted on three different rock types, namely Berea sandstone, Castlegate sandstone, and Mancos shale. Several injections were performed on each sample to characterize the values of the fracture initiation pressure (FIP) and the fracture propagation pressure (FPP) and thereby characterize the WBS phenomenon. Typical experimental variables include the applied confining pressure, type of base fluid (water-based or synthetic-based), and concentration, type, and particle size distribution (PSD) of the lost circulation material (LCM) used to achieve WBS benefits. Post-fracturing analysis was conducted by using techniques such as computerized axial tomography (CAT) scan and petrographic imaging to investigate the geometry of induced fractures and formed seals. The experimental results show that the FIP is mainly a function of the rock fracture toughness and stress concentration around the borehole, and independent of the drilling fluid used. The FPP, however, is mainly affected by the formulation of the drilling fluid and can be significantly enhanced by adding LCM. The obtained FPP values are compared with the large-scale fracturing experiments conducted at the Drilling Engineering

Association (DEA) 13 investigations. Excellent agreement was observed between the DEA 13 and UT MudFrac experimental results. Furthermore, it is shown that FPP changes linearly with the minimum horizontal stress (S_{hmin}), and the results of fracturing experiments using a relatively small borehole size at low confining pressures can be extrapolated to predict the FPP of large-scale fracturing experiments, and possibly field applications. The effect of LCM concentration on strengthening effects is investigated. It was found that although a minimum concentration of LCMs is required for effective WBS, FPP does not increase significantly for concentrations above a certain upper threshold value. Moreover, for any rock with a given set of rock strength and failure parameters, there exists an optimum PSD to maximize WBS benefits. Optimum PSD appears to be of primary importance for WBS, almost independent of LCM type. The experimental results presented in this dissertation are in clear disagreement with wellbore stress augmentation (WSA) mechanisms such as stress caging (SC) and fracture closure stress (FCS) which were previously proposed to explain the WBS phenomenon. Furthermore, they clearly favor the fracture propagation resistance (FPR) explanation to WBS. Existing guidelines to design WBS treatments such as the one-third rule, the Vickers criteria, and the ideal packing theory are evaluated. It is shown that none of these theories properly represents the physics of fracture sealing. To remedy this situation, a new family of design curves is introduced to determine the optimum PSD for WBS applications.

Table of Contents

List of Tables

List of Figures

CHAPTER ONE: INTRODUCTION

1.1 Definition of Wellbore Strengthening

The drilling margin (or mud window) is defined as the difference between the fracture pressure and either the pore pressure or the mud pressure required for mechanical wellbore stability, whichever of the two is higher (Karimi Vajargah and van Oort, 2015). The margin shrinks in geo-pressured formations or in open-hole zones with production depleted formations present. Note that both situations often occur at the same time in more mature deepwater drilling environments. A narrow drilling margin complicates well delivery by posing severe lost circulation, well control or well instability risks that (in extreme cases) may lead to losing the well and having to drill costly sidetracks (see e.g., Gradishar et al., 2013).

WBS is an effective technique to help negotiate challenging wells with a narrow drilling margin (van Oort et al., 2011). It can be defined as the extension of the drilling margin through enhancement of the fracture pressure. Fracture pressure enhancement is usually achieved by solid plugging of near-borehole fractures. The plugging agents used in this method are certain particulate solids known as LCM or lost prevention material (Fuh et al., 1992). As explained by van Oort et al., 2011, the term “wellbore strengthening” is actually a misnomer. WBS treatments are singularly aimed at elevating the effective fracture pressure which in turn raises the drilling margin, and are not designed to enhance the rock’s (matrix) strength as the WBS term may imply. Although to a driller the borehole would appear stronger in its ability to resist high equivalent circulating densities after a WBS treatment, the phenomenon should more properly be referred to as “drilling margin extension”. However, given the historic precedents and shared understanding of what is meant by “wellbore strengthening”, this term is exclusively used throughout this

dissertation. For the sake of simplicity, we use acronyms extensively in the remainder of this dissertation. A comprehensive list of all used acronyms is provided in Glossary.

1.2 Importance of Wellbore Strengthening

To illustrate the significance and value of WBS, we looked at its potential impact on simplifying and slimming down deepwater casing designs. Figure 1 presents a comparison of infinite kick, "bottom up" casing designs for the cases of conventional drilling, use of Dual Gradient Drilling (DGD), drilling with an effective WBS technique, and drilling using both DGD and WBS for the situation of a very narrow drilling margin, as often encountered in geo-pressured deepwater environments. The benefits of DGD over conventional drilling are immediately clear by observing that the non-linear mud gradient profiles offered by the former fit the available margin much better than the constant profiles of conventional drilling, resulting in the omission of two casing strings in this case. We compare this result with the case where we have elevated the fracture gradient throughout the well consistently by only 0.5 pound per gallon (ppg) through effective WBS, showing that a simplification of the casing program similar to the DGD case appears possible. When both DGD and WBS techniques are used, the casing program can be further simplified and the well may be constructed by using only two casing strings.

The aim of this simple exercise is to show that WBS should be ranked in the same category as Managed Pressure Drilling (MPD) and DGD in its ability to get complex wells with challenging drilling margins drilled. But whereas the latter usually require significant changes and additions to rig hardware as well as changes to the rigs themselves, WBS may be more simply and cost-effectively achieved by targeted additions of the right WBS materials to mud systems coupled with strategies to maintain these material at sufficient

concentrations in the mud system (see e.g. van Oort et al., 2007 and 2011). WBS is simply an enabler for extending the capabilities of conventional drilling techniques. Moreover, since WBS works on favorably extending the drilling margin while MPD/DGD creates a more advantageous annular pressure profile that better fits the available margin, the two technologies can be used synergistically to significant cumulative benefit (Jacobs, 2014).

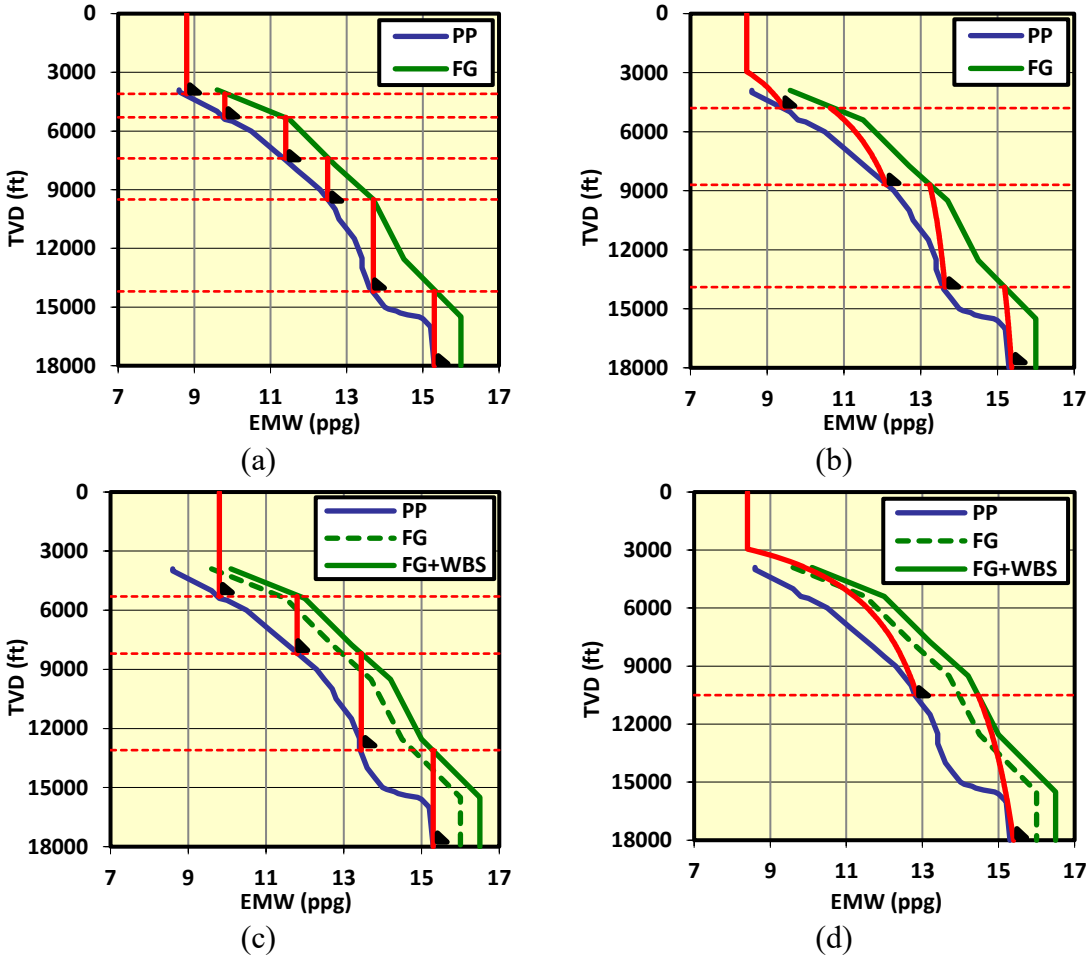

Figure 1 – Comparison of infinite kick "bottom up" casing designs: (a) conventional drilling; (b) DGD; (c) drilling with effective WBS; (d) drilling with DGD and effective WBS. Dotted horizontal red lines and black triangles indicate recommended casing setting depths, solid red lines indicate annular pressure profiles.

1.3 Outline

This dissertation is laid out in six chapters and eight appendices:

- Chapter 2 presents a theoretical background and review of literature in the field of WBS. A detailed description of the fundamentals of initiation and propagation of drilling induced fractures (DIF) is presented. Major previous experimental studies of WBS are reviewed. Also, theoretical models for fracture initiation and propagation pressures are revisited. A succinct overview of the existing guidelines to design WBS treatments is presented.
- Chapter 3 discusses the major issues in the modelling and application of the WBS phenomenon in the drilling industry. It is shown that there is an evident need for further experimental investigation of this phenomenon. Also, the research objectives of this dissertation are stated.
- Chapter 4 introduces the designed experimental set-up: The UT MudFrac system. The properties of the tested rock and fluid samples are reported. A detailed description of the employed testing procedure to measure the FIP and FPP is presented. The results of validation experiments are also shown. A portion of this chapter was presented at the 2015 SPE Annual Technical Conference and Exhibition in Houston, Texas (Razavi et al., 2015).
- Chapter 5 presents the results of experimental studies, conducted on both permeable and impermeable rock samples. Furthermore, the obtained results for FIP and FPP are analyzed and compared with well-known theoretical and experimental studies. In addition, the existing design guidelines for bridging particles are evaluated and a novel design method for LCM PSD is introduced. Portions of this chapter were presented at the 2016 SPE Western Regional Meeting in Anchorage, Alaska

(Razavi et al., 2016a), and at the 2016 ARMA Geomechanics Symposium in Houston, Texas (Razavi et al., 2016b).

- Chapter 6 summarizes the major contributions of this dissertation. It also states recommendations for future works in this field.
- Appendix I presents the supporting information for Section 5.1.1. The fracture propagation injection curves for Berea and Castlegate sandstone using various LCM PSDs are shown.
- Appendix II presents the supporting information for Section 5.1.2. The fracture propagation injection curves for Berea sandstone using various LCM types are shown.
- Appendix III presents the supporting information for Section 5.1.3. The fracture propagation injection curves for Berea and Castlegate sandstone using various LCM concentrations are shown.
- Appendix IV presents the supporting information for Section 5.1.5. The fracture propagation injection curves for Berea and Castlegate sandstone using drilling fluids with or without LCM are shown.
- Appendix V presents the supporting information for Section 5.2. The fracture propagation injection curves for Mancos shale samples are shown.
- Appendix VI presents the supporting information for Section 5.4.1. The fracture propagation injection curves for synthetic based mud (SBM) without LCM are shown. Also, the values of average FPP using Oil Based Mud (OBM) without LCM – extracted from the DEA 13 final reports– are listed.
- Appendix VII presents the supporting information for Section 5.4.2. The fracture propagation injection curves for SBM with fine graphite-based LCMs are shown. Also, the values of average FPP using mineral oil based mud (MOBM) with

calcium carbonate-based LCM – extracted from the DEA 13 final reports – are listed.

- Appendix VIII presents the supporting information for Section 5.4.3. The fracture propagation injection curves for SBM with Gilsonite-based LCMs are shown. Also, the values of average FPP using MOBM with Gilsonite-based LCM – extracted from the DEA 13 final reports – are listed.

CHAPTER TWO: BACKGROUND

2.1 Initiation and Propagation of Drilling Induced Fractures

This section presents an introduction to initiation and propagation of DIFs by revisiting the fundamentals of Leak-Off Testing (LOT). LOT is the most reliable method used in the drilling industry to characterize the fracturing behavior of a formation (Postler, 1997, Okland et al., 2002, and van Oort and Vargo, 2008). In order to perform an LOT, the well is shut-in and slowly pressurized by injecting the drilling fluid into the borehole. The results of LOT are then typically reported by plotting the values of the borehole pressure against either the injection volume or time.

The schematics of an LOT on a brittle intact rock are shown in Figure 2. Since the rock is intact (i.e., there exists no natural fracture), the LOT is started with a fracture initiation phase. This phase is indicated by a linear pressure ramp-up to a maximum borehole pressure and followed by an immediate pressure drop. For a brittle rock, the maximum borehole pressure reached at the initiation phase is defined as the FIP (Okland et al., 2002). The FIP is the pressure required to create a small fracture in the vicinity of the borehole, and is equal to the pressure required to counterbalance the borehole tangential stress and rock tensile strength (Morita et al., 1990). It should be noted that in more ductile rocks the FIP is indicated by the point in which the pressure ramp-up curve deviates from linearity and the borehole pressure may further increase from the FIP to maximum value, known as the formation breakdown pressure (FBP) or uncontrolled fracture pressure (UFP). A detailed description of LOT in ductile materials is presented by van Oort and Vargo, 2008.

In order to avoid damaging the casing shoe, the LOT is typically stopped before reaching the fracture initiation phase. However, if the fluid injection is continued beyond

fracture initiation phase, the LOT reaches the fracture propagation phase (Okland et al., 2002). The fracture propagation phase is marked by consecutive cycles of pressure ramp-up to a local maximum in borehole pressure, followed by immediate pressure reduction due to fracture enlargement. The local pressure maxima at this stage correspond to the pressure required for re-opening and propagation of the induced fracture at the initiation phase, and is known as the FPP (Morita et al., 1996, and Okland et al., 2002, and). For permeable rocks drilled with solid-laden fluids, the FPP is primarily determined by two energy dissipation mechanisms. The first energy dissipation mechanism is related to the amount of energy required for creating new surfaces in the rock and it is closely associated with the rock fracture toughness and the geometry of the growing fracture (Morita et al., 1990, Morita and Fuh, 2012, and van Oort and Razavi, 2014). The second dissipation mechanism is closely related to the formation of an un-invaded "dry" zone close to the fracture-tip (Morita et al., 1990, Fuh et al., 1992, and Onyia, 1994). The existence of the dry zone was confirmed in previous experimental investigations (Morita et al., 1996, Dudley et al., 2000). These experimental investigations clearly showed that accumulation of solids along the fracture surface leads to formation of low-permeability pressure barriers (i.e., seals) which reduce the fluid pressure applied to the fracture tip. Thus, for each cycle of fracture propagation, some energy is required to break the formed seal and facilitate the pressure communication between the borehole and the fracture-tip.

Analysis of the large-scale fracturing experiments conducted in the DEA 13 investigation shows that the propagation phase typically includes two stages: transient and stable (the DEA 13 final reports: phase I (1985) and phase II (1988)). The transient propagation stage occurs immediately after the FIP and is related to the growth of short DIFs near the borehole. The transient propagation stage is indicated by a sharp decline in the FPP. It can be shown that the FPP in the transient stage (i.e., the transient FPP) is

primarily dominated by the first energy dissipation mechanism. This is because a significant amount of energy is required for propagation of short DIFs (van Oort and Razavi, 2014). However, this energy dissipation mechanism becomes less important with the enlargement of the DIF, since longer DIFs require less energy for tip advancement. The transient propagation stage is followed by the stable propagation stage, which is manifested by a relatively constant FPP. Unlike the transient stage, the FPP at the stable propagation stage (i.e., the stable FPP) is determined by the energy dissipation mechanism associated with the re-opening of the formed seals near the fracture tip. The change from the transient to the stable stage happens for two reasons: (1) the resistance to create new surface significantly reduces by enlargement of the fracture, and (2) formation of effective pressure barriers typically requires a minimum volume of fluid injection.

It should be noted that although exceeding the FIP leads to creating small DIFs near the borehole, it does not necessarily result in a major lost circulation problem. Major lost circulation problems typically occur when the borehole pressure remains above the FPP, which results in creating large fracture networks and potentially losing a great volume of drilling fluid. The stable FPP is by definition lower than the transient FPP and does not depend on the size of the DIF. Thus, the stable FPP may be used as a reliable (conservative) estimation of the fracture pressure to determine the drilling margin.

Unlike the FIP, which appears to be independent of the drilling fluid used (a statement independently verified in this thesis), the FPP is primarily dominated by the type and formulation of the drilling fluid (Onyia, 1994, Dudley et al., 2000). Furthermore, the FPP may be significantly enhanced by adding LCM to the drilling fluid. This FPP enhancement is more pronounced in the stable stage, since the stable FPP is primarily affected by the formation of seals along the fracture length. In Figure 2, the schematics of the stable FPP values before and after using a WBS treatment are compared. The stable

FPP is significantly increased by using WBS treatments. This also means that WBS can be defined as the extension of the stable FPP. Furthermore, comparison of the stable FPP before and after applying WBS indicates the attainable strengthening benefits of an LCM blend. This topic is further discussed in this dissertation.

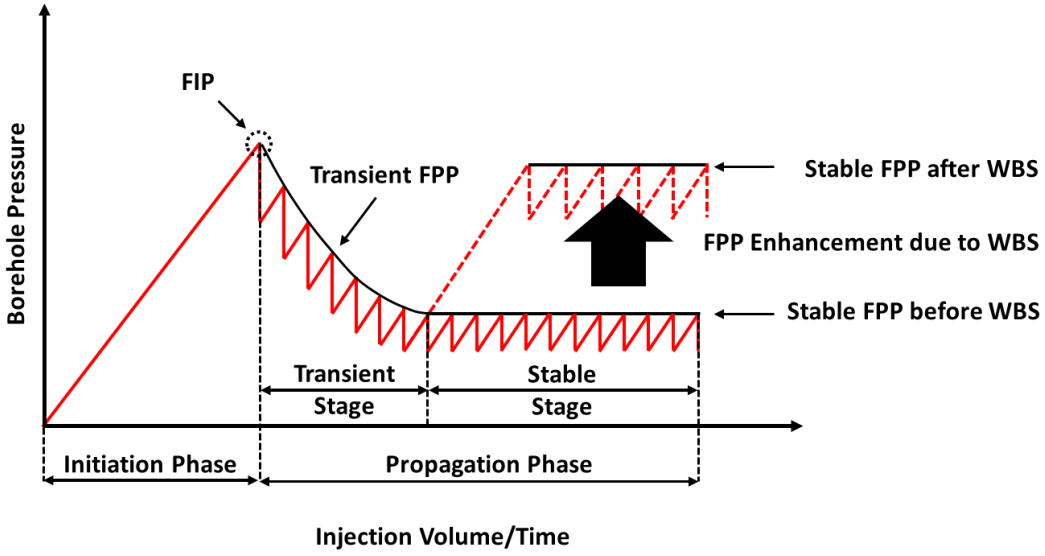

Figure 2 – Schematics of an LOT on a brittle intact rock.

2.2 Major Experimental Investigations

2.2.1 The Drilling Engineering Association 13 Investigation

The DEA 13 investigation remains the most relevant experimental study conducted into the initiation and propagation of DIF (the DEA 13 final reports: phase I (1985), and phase II (1988)). Large-scale fracturing experiments were performed on 30 inch cubical samples with a borehole diameter of 1.5 and 4 inches, under polyaxial stress conditions. Several fracturing injections were conducted on each sample, while varying the in-situ stresses, and the drilling mud type and density.

DEA 13 – Phase I (1985) included twenty-three large-scale fracturing experiments on Berea sandstone samples. The experiments were carried out using both water based mud (WBM) and OBM. Two distinct types of OBMs were tested: MOBM, and diesel oil based mud (DOBM). The tests were conducted at either 10 or 16 ppg mud density. Phase I experiments showed that the FIP is not affected by the mud type or density. The FPP, however, can be significantly affected by the drilling fluid system. In particular, the FPP was found to be strongly influenced by the mud type and density. Higher FPP values were observed when using WBM, compared to DOBM and MOBM. For WBM and DOBMs, fluids with 16 ppg density showed significantly higher FPP values compared to those with 10 ppg. For all the tested samples, the measured FPP values were significantly higher than the S_{hmin}. This difference between the FPP and S_{hmin} is due to the inherent fracture sealing capability of the drilling fluids (Morita et al., 1996). Drilling fluids typically have a high concentration of solids (mainly as the weighting agent), which is beneficial in sealing the DIFs. As explained before, these sealing capabilities may be further enhanced by adding LCM.

DEA 13 – Phase II (1988) experiments were conducted to investigate the effect of LCM on the FIP and FPP for WBM and OBM. In Phase II investigations, eleven tests were performed on cubical Berea sandstone samples. In order to study the effect of borehole diameter, one sample was tested with a 4 inch diameter borehole (while the rest were tested with a 1.5 inch borehole). All tests were conducted using 16 ppg mud density. Several LCM types were tested, including calcium carbonate and Gilsonite with concentrations of 40 and 80 pounds per barrel (ppb). The experiments clearly showed that the presence of LCMs does not affect the FIP. However, fluids loaded with calcium carbonate and Gilsonite particles provided significantly elevated FPP. No major difference in the FPP

was observed between the 40 and 80 ppb tests. Also, for identical drilling fluid and in-situ stresses, similar FPP values were observed for 1.5 and 4 inch diameter boreholes.

2.2.2 Global Petroleum Research Institute Project

Dudley et al. (2000) conducted the Global Petroleum Research Institute (GPRI) project, with the objective to minimize lost circulation events when using SBM. The GPRI project was aimed at improving the lost circulation control capabilities of invert oil emulsion muds, notably SBM. WBS experiments were performed on cylindrical samples under conditions of isostatic confining stress. The GPRI experiments confirmed the fundamental findings of the DEA 13 investigations on FIP and FPP. Moreover, fracture sealing capabilities of various types of lost circulation materials such as graphite, calcium carbonate, and cellulosic fibers were also investigated. The GPRI project postulated two distinct mechanisms for WBS generated by the use of LCMs: (1) fracture bridging performed by coarser particles, (2) impairment of the fracture hydraulic conductivity using finer particles. Thus, an ideal LCM blend should contain coarse bridging agents to form a seal in the fracture and finer particles to reduce the permeability of the formed seal.

2.2.3 Fracture Studies Joint Industry Project

The Fracture Studies Joint Industry Project (JIP) (2004-2014) was another notable attempt to better understand the WBS phenomenon and to find practical ways to exploit its benefits. Several papers have been published on the findings of this JIP since its start in the mid-2000's (see e.g., Kageson-Loe et al., 2008, Sanders et al., 2008, Guo et al., 2009 and 2014). Several experimental set-ups were used in the experimental investigations, including a fracture sealing tester and block testing equipment. The fracture sealing tester contained two parallel aluminum platens with adjustable opening to simulate fracture faces. Extensive experimental investigations were conducted to study the effect of LCM PSD,

type, and concentration on fracture bridging and reopening. Although the results provide valuable general insights into the fracture sealing capabilities of drilling fluids and LCM additives, the relatively simplistic experimental set-up complicate the extension of the results to a real-life rock fracturing scenario. In addition, fracturing experiments were performed using a block tester to characterize remedial WBS treatments on drilling induced- and natural fractures (Guo et al., 2014). Compared to the base-mud tests, measured FPP values for LCM-laden fluids were increased by more than 300 and 400 percent for induced and natural fractures respectively. These high FPP values for drilling induced fractures even exceeded the rock's initial FIP, which seemed unrealistically high and generally not in agreement with the previous investigations.

2.3 Theoretical Modelling of Drilling Induced Fractures

2.3.1 Fracture Initiation Models

Hubbert and Willis (1957) pioneered the theoretical modelling of the initiation of drilling induced fractures. Using the Kirsch's (1898) equations for stress distribution around the borehole, they derived a closed-form solution to estimate the FIP. Their work, which employs the theory of elasticity, states that borehole fracturing occurs if the borehole pressure exceeds the tangential stress of the borehole and the tensile strength of the rock. Haimson and Fairhurst (1969) modified the Hubbert and Willis linear elastic model to incorporate the effect of drilling fluid invasion into the wellbore wall. Both Hubbert and Willis' model and Haimson and Fairhurst's model are developed assuming a geometrically perfect circular borehole and ignores the fact that real boreholes contain pre-existing fractures, due to flaws in the rock fabric and geometrical imperfections in the borehole.

Rummel (1987) showed that a linear elastic model does not accurately characterize the FIP, since it ignores the effect of pre-existing fractures around borehole. Instead, the

FIP is best characterized using a fracture mechanics approach. Next, building on the pioneering works of Hardy (1973), Abou-Sayed et al. (1978), and Rummel and Winter (1983), Rummel proposed a closed-form solution for the initiation of hydraulically induced fractures. According to his solution, the problem of hydraulically induced fracture initiation can be reduced to the re-opening and growth of near-borehole micro-fractures, rather than creating fractures from a borehole with an idealized geometry (without pre-existing fractures). To derive his solution for the FIP, he used the principle of superposition to incorporate the effects of minimum and maximum horizontal stresses, borehole pressure, and pressure distribution within the fracture. This solution, however, requires additional parameters to determine the FIP, such as the length and internal pressure distribution of the pre-existing fractures. In the recent years, various researchers have improved upon the proposed fracture mechanics approach for the initiation of the DIFs. Detournay and Carbonell (1997) modified the model to incorporate the effect of pressurization rate. Also, Mehrabian et al. (2015), Mehrabian (2016), and Mehrabian and Abousleiman (2016) investigated the effect of near wellbore fractures and their orientation on the tangential stress redistribution around the borehole.

2.3.2 Fracture Propagation and Wellbore Strengthening Models

The DEA 13 (1985 – 88) and GPRI experiments (2000) showed that the FPP of DIFs is significantly affected by the base fluid and solid content of the drilling fluid used. Thus, conventional hydraulic fracturing models may not be used to explain the DIF propagation problem, since these models do not properly consider the effect of the solid content of the fracturing fluid. This problem becomes even more complicated when deliberately adding LCM to the drilling fluid. To date, two main models have been

proposed to explain the underlying physics of DIF propagation and WBS phenomenon, namely the FPR and the WSA models.

The primary version of the FPR model was introduced by Morita et al. (1990) and Fuh et al. (1992). According to their works, all drilling fluids have an inherent tendency to seal drilling-induced or natural fractures. This fracture sealing tendency is due to presence of solids in the drilling fluids which form bridges along the fracture aperture. The formed bridge then stabilizes the fracture and hence increases the formation resistance to further fracture propagation. The FPR model relies on the empirical evidence obtained from the DEA 13 experiments. These experiments showed that there exists a dry zone in the vicinity of the fracture tip which is not invaded by the drilling fluids. Also, a dehydrated mud zone was found behind the un-invaded zone. The dehydrated mud zone and un-invaded fracture zone form a pressure barrier which isolates the fracture tip from the borehole pressure. Furthermore, the fracture sealing benefits of drilling fluids may be significantly enhanced by adding plugging solid (i.e., LCM) to the drilling fluids. Onyia (1994) studied the effect of fluid loss characteristics of drilling fluid on the FPP by analyzing the DEA 13 results. His work showed that WBMs yield an inherently higher FPP than OBM and SBMs. This is because WBM forms an external filter cake during conditions of dynamic fluid loss within a growing fracture, which is more effective in pressure isolation of the fracture tip than the internal filter cake formed by the OBM and SBM. van Oort et al. (2007) introduced the idea of continuous WBS to maintain the optimum concentration and PSD of LCM during drilling. Morita and Fuh (2011) studied the effects of pore pressure build up, elastic moduli, borehole radius, and horizontal stress anisotropy. A more recent version of the FPR model was presented by van Oort et al. (2011) and van Oort and Razavi (2014). They showed that the FPR model mainly depends on the formation permeability and fluid loss properties of the drilling fluids, since solid plugging requires effective fluid filtration to the

formation matrix. Thus, stronger WBS effects are expected in highly permeable rocks. In contrast, conventional WBS techniques which relies on solid plugging are usually un-successful in impermeable formations. The formation stiffness, however, does not play a major role in FPP and WBS effects.

WSA states that the WBS phenomenon is due to the augmentation of the compressive stress perpendicular to the fracture face (Alberty and McLean, 2004, Aston et al. 2004, and Dupriest, 2005). According to the WSA model, the presence of the LCM in the drilling fluids allows for deliberate opening of the fracture, which leads to the elevation of either the hoop stress around the wellbore or the fracture closure stress. Two well-known versions of the WSA model include SC and FCS models. The SC model (Alberty and McLean, 2004, Aston et al., 2004 and 2007, and Zhang et al., 2016) states that WBS is due to augmentation of the borehole hoop (tangential) stress. The hoop stress augmentation is achieved by deliberate enlargement of the fracture aperture at the borehole face. Alberty and McLean (2004) employed a finite element analysis to indicate that a significant augmentation of wellbore tangential stress may be obtained due to fracture sealing. Zhang et al. (2016) presented a semi-analytical approach to incorporate the effects of horizontal stress anisotropy and borehole inclination angle. The FCS approach to WBS (Dupriest et al., 2005 and 2008), shares with the above-mentioned SC approach its emphasis of increasing formation stress, in this case the stress involved in closing a fracture. FCS is augmented by deliberately propping open fractures at some unspecified distance away from the wellbore. In both WSA versions (SC and FCS) the strengthening effects are proportional to the rock stiffness (i.e., Young's Modulus). Thus, for an identical opening of the fracture width, stronger WBS effects are expected in a stiffer rock. Furthermore, the crushing strength of the plugging solids (LCMs) is an essential parameter in this model

(Aston et al., 2004), i.e. high strength LCMs are required for WBS according to the WSA models.

FPR and WSA may seem two plausible explanation for the underlying physics of WBS phenomenon. However, when designing a WBS treatment, adopting either of the two models will result in significantly different LCM size and type, and application technique. In Table 1, we compare the differences between the WBS treatments designed based on the WSA and FPR models. A primary version of this table was presented by van Oort et al., 2011. Unlike FPR model, which recommends continuous WBS during drilling, the WSA model implies that WBS treatments should be performed in a start-stop fashion using dedicated squeezes. This means that each time a certain borehole section has been drilled and/or a lost circulation incident happens, the regular drilling operations has to be stopped. Next, the drilling fluid is circulated out and a hesitation squeeze pill with high LCM content is circulated into the wellbore and a hesitation squeeze is performed. Some WSA models, namely the FCS model, prescribes performing repeat squeezes to layer material in the fracture in order to reach the optimum strengthening benefits. According to this approach, after injecting a certain (typically large) volume of the hesitation squeeze pill, the circulation needs to be stopped to let the formation “heal”. Subsequently, the circulation is resumed to inject the next hesitation squeeze pill. Injection of the hesitation squeeze pills is repeated until no further significant increase is observed in the fracture pressure. Then, the pill is replaced with mud and drilling operation is resumed. This process is not only cumbersome and time-consuming, but also highly expensive when practiced on offshore deepwater rig. An additional drawback is that formations are never protected during drilling because this type of strengthening is “after-the-fact” and has to happen repeatedly until the entire drilled section is secured behind casing and cement. There are no such

drawbacks and limitations according to the FPR mechanism, which allows for continuous protection of loss-prone formations suing continuous strengthening.

Another important difference between the FPR and WSA mechanisms concerns the strength of the LCM particles used to achieve optimum WBS effects. When using the FPR model, the particle strength of the LCM is relatively un-important, whereas the LCM material in WSA model should have sufficient crushing capacity to withstand the stress augmentation. Yet another difference between the two models is related to the location of seal formation. According to the WSA model, seals are formed either at the borehole face (SC) or along the fracture length with a small distance from the borehole (FCS). This typically requires using significantly coarse LCM, since the fracture mouth has a significantly large aperture. In contrast, according to the FPR model, the seal forms in the vicinity of the fracture tip. Thus, WBS can be achieved using relatively finer particles.

Parameter	Wellbore Stress Augmentation	Fracture Propagation Resistance
Application technique	Hesitation pill squeeze	Continuous in mud
Rock closure stress	Altered	Unaltered
Fracture tip isolation	Not required	Required
LCM particle strength	Important	Unimportant
Seal location	Near the borehole face	Near the fracture tip

Table 1 – Overview of the differences between the WBS treatments designed based on the WSA and FPR models

2.4 Design Guidelines for Wellbore Strengthening Treatments

Several design guidelines were introduced to determine the optimum PSD, concentration, type, and shape of the bridging particles. Abrams (1977) pioneered the design of bridging solids. His work led to the introduction of the well-known "one-third rule", also known as Abrams' rule. The one-third rule recommends the following guidelines for the size and concentration of bridging materials:

- The median particle size of the bridging additive should be equal to - or slightly greater than - one-third the median pore size of the formation.
- The concentration of the bridging size solids must be at least 5 percent by volume of the solids in the final mud mix.

Abrams' work was primarily aimed at reduction of formation damage due to reservoir impairment. However, the one-third rule can be applied to determine the size of bridging solids used for various particle plugging applications, including WBS. Building on Abrams' work, Vickers et al. (2006) employed the pore plugging apparatus (PPA) and return permeability testing to minimize fluid loss. His work resulted in the introduction of the "the Vickers criteria", which prescribes the following mass division diameters for the PSD of the bridging LCM blends:

- D_{90} = largest pore throat
- D_{75} < 2/3 pore throat
- D_{50} = 1/3 of the mean pore throat
- D_{25} = 1/7 of the mean pore throat
- D_{10} > smallest pore throat

In addition, the Vickers criteria recommend that the concentration of bridging material needs to be greater than 30 ppb for WBM (this may be reduced for oil-based mud).

This concentration, however, is lower than the 5 percent solid volume recommended by the Abrams' rule.

Fuh et al. (1993) patented a method for inhibiting the initiation and propagation of fractures by using LCM of a specific size. Their method was derived from the DEA 13 investigations (1985 – 1988) and several field applications, which employed LCMs for WBS purposes. The patent prescribes adding 30 to 50 ppb of LCM with a critical size ranging from 250 to 600 microns to the drilling fluid. The preferred LCM types are nut shells or calcined petroleum coke.

Dick et al. (2000) conducted another major effort for the selection of bridging particles by adopting the "ideal packing theory" from the paint industry to practical oilfield use. Originally, the ideal packing theory was introduced by Andreasen and Anderson (1930) who proposed a power law relationship between the cumulative volume (CV) and the particle size for effective bridging. The exponent value in the power law relationship typically ranges between 0.5 and 1. Kaeuffer (1973) states that ideal packing occurs when the CV varies linearly with the square root of the particle size (which means the exponent value is equal to 0.5). More recently, Chellappah et al. (2012) improved upon this power law model by employing PPA testing and suggesting that the optimum value of exponent is closer to 1 than to 0.5.

CHAPTER THREE: PROBLEM STATEMENT AND OBJECTIVES

3.1 Problem Statement

The importance of WBS to complex well construction is discussed in Section 1.2. Given its potential, it is crucial that the WBS phenomenon, its merits as well as its limitations are properly understood and can be reliably exploited for well construction purposes. We are, unfortunately, not yet there from a scientific and industry perspective. For instance, there exists no common agreement on the underlying physics of the WBS phenomenon in the drilling industry. As described earlier, since the introduction of LCM to the drilling industry, several different (and sometimes contradictory) mechanisms have been proposed to explain this phenomenon while confusion reigns supreme, even (or perhaps particularly) among subject-matter experts. Furthermore, none of the proposed models properly incorporate the effects of the formation properties, the drilling fluid formulation, and the LCM blend used. More importantly, there are currently few engineering models and guidelines that allow for effective and reliable exploitation of WBS for well construction purposes (e.g. to optimize casing setting depths).

Given the complexity of WBS, experimental investigation is essential to help clarify the true nature of this phenomenon and identify practical ways to optimally utilize it for well construction optimization purposes. To date, several experimental investigations have been conducted to study the WBS phenomenon. However, none of these investigations presents a systematic and comprehensive study of all major factors which affect WBS phenomenon. The DEA 13 investigation (the DEA 13 final reports: phase I (1985), and phase II (1988)) was a fundamental step to characterize the sealing capabilities of the drilling fluids. However, the scope of the conducted experiments in this investigation was limited in terms of the concentration, PSD, and type of the LCMs tested. Also, some

of the popular present-day WBS materials (e.g. graphite, fiber) favored in current field operations were not yet available at the time of the investigation. No framework was introduced to extend the results of fracturing experiments to full-scale wells. Interpretation of the conducted experimental results are complicated by several factors such as the tested borehole diameter, applied in-situ stresses and pore pressure, and fluid formulation. The GPRI project (Dudley et al., 2000) significantly improved our knowledge of the underlying physics of the WBS phenomenon. However, there are several issues which were not addressed during this project. For instance, the FPP values were measured based on single fracture propagation cycles, due to lack of pressure control to maintain constant confining pressure during the propagation injection. Relying on a single cycle of fracture propagation for FPP measurement can be significantly misleading because a number of propagation cycles is required to characterize the FPP accurately. Additionally, in the GPRI experiments, the majority of the fracture reopening and propagation injections were performed under the same in-situ stress conditions and the effect of confining pressure variation on FPP was not investigated. Moreover, no post-test analysis was performed on the possible relationship between the geometry of the formed fracture and the optimum LCM particle size distribution. Given the shortcoming of the DEA 13 and GPRI projects, it seems that more experimental work is required to study the WBS phenomenon in a systematic and realistic manner.

Regarding the existing guidelines to design WBS treatments, LCMs have become a standard part of fluid design for drilling formations with a narrow drilling margin. However, the drilling industry still lacks a comprehensive framework to optimally select LCMs for WBS applications. The LCM blends are usually designed using the general guidelines for bridging particles. However, the majority of these guidelines have not been developed exclusively for WBS purposes and the application of these guidelines for WBS

purposes have not been evaluated in realistic fracturing experiments. It seems that the drilling industry may benefit from a systematic investigation of LCM design parameters such as PSD, concentration, and type.

3.2 Objectives

The research objectives of this dissertation include:

- Development of a reliable experimental approach to study the initiation and propagation of DIFs. The developed experimental approach may then be employed to conduct a systematic investigation of the WBS phenomenon.
- Studying the dependence of WBS effects on various formation properties such as permeability, stiffness (Young's modulus), tensile strength, fracture toughness, and Unconfined Compressive Strength (UCS).
- Investigation of the underlying physics of the WBS phenomenon through an in-depth post-fracturing analysis of the tested samples. CAT scan and petrographic imaging techniques are used to study the geometry of the DIF and formed seals. The results of this investigation may also be used to examine the proposed models for WBS.
- Parametric studies to investigate the effects of LCM concentration, type, PSD and fluid injection volume on strengthening. The results of these parametric studies are used to re-evaluate the existing guidelines to design WBS treatments and to introduce a novel guideline to maximize strengthening benefits.
- Analysis of the FIP in various formation types and studying its dependence on the tangential stress and borehole geometry. The results of this study are used to re-evaluate the existing theories for FIP and characterize the geometry and pressure distribution of pre-existing fractures in the vicinity of the borehole.

- Analysis of the FPP in various formation types and using different stress conditions. The obtained results are compared the large-scale fracturing experiments conducted in the DEA 13 investigation, to study the effects of the in-situ stresses, borehole size, and geometry of the fractures. This comparison is also beneficial to the development of a framework to extend the results of fracturing experiments to full-scale boreholes drilled in field applications.
- Studying the fracturing behavior of impermeable formations. This includes performing a feasibility study to determine whether conventional WBS techniques, which relies on the use of LCMs, can be successful in strengthening impermeable formations (e.g., shale).

CHAPTER FOUR: EXPERIMENTAL

4.1 Experimental Set-up: The UT MudFrac System

A state-of-the-art experimental set-up was designed and manufactured for in-depth WBS investigations. The UT MudFrac system (Figure 3a-b) is a dual flow-loop/pressure-intensifying system. Cylindrical rock samples of 4 inch in diameter and 6 inch in length were used. A 1/2 inch borehole was drilled and flow lines were then inserted 2.5 inch into each end of the sample, leaving a 1 inch section of the rock exposed for fracture initiation. The flow lines were epoxied to the rock sample to prevent pressure communication between the borehole and the vessel. The sample was isolated by using two steel end-caps in the axial direction and a rubber sleeve in the radial direction (Figure 4a-b).

A progressive cavity pump was used to circulate the drilling fluid through the flow-loop. In addition, a rotary vane water pump was used to saturate the rock sample, to examine the connections for leakage before running the test, and to flush the flow-lines after each test. Since the pressure required for fracture initiation and propagation injections was beyond the working pressure range of the mud pump, a pressure intensifying system consisting of a fluid accumulator and a positive displacement pump was employed. The accumulator is essentially a fluid container, which separates the pressurizing fluid (water) and drilling fluid. The fluid accumulator was installed between the injection pump and the flow loop. Before each injection, the accumulator was filled with the drilling fluid while the fluid was circulating through the flow loop. Once the accumulator was filled with enough fluid to perform the fracture initiation or propagation injection, pressure was intensified by shutting in the flow loop and extending the injection pump piston to apply hydraulic pressure to the borehole.

(a)

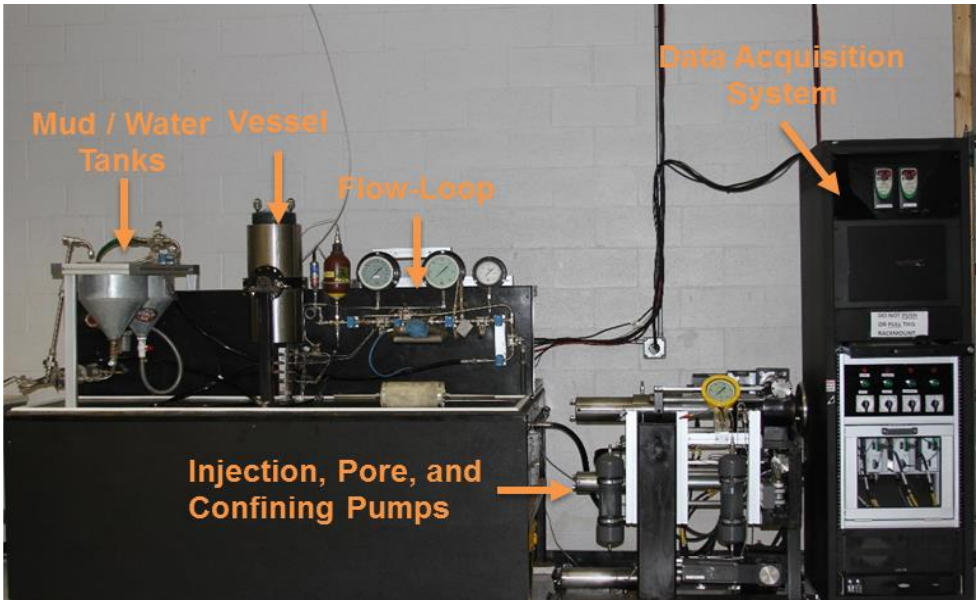

(b)

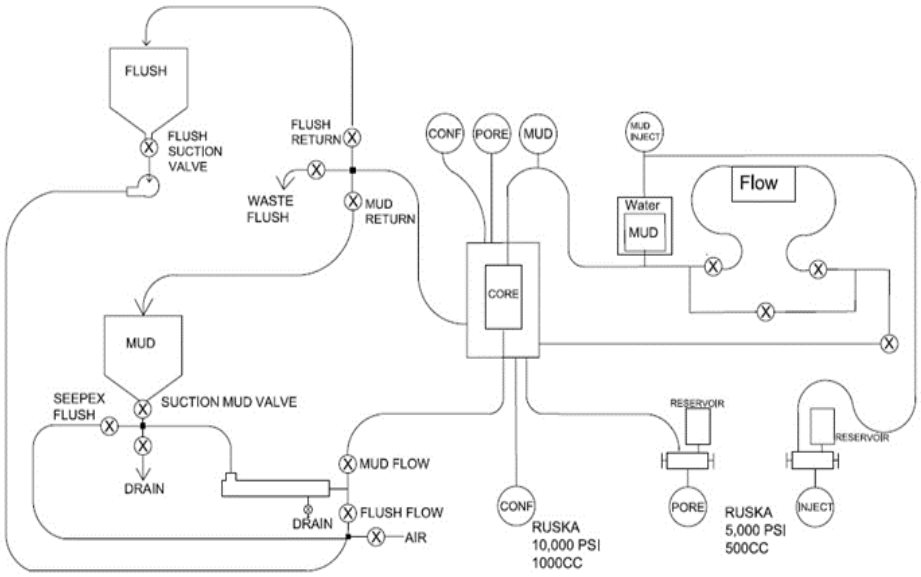

Figure 3 – The UT MudFrac system: (a) photograph with overlay, indicating essential equipment components; (b) schematics of the dual flow-loop/pressure-intensifying system.

The UT MudFrac System applies isostatic stress to the sample by compressing the confining fluid (water) in the vessel (Figure 4c). Permeable rock samples were tested under isostatic stress condition. In addition to the confining pressure, fracturing experiments on

shale samples were performed under approximately 1000 psi axial stress to prevent sample failure due to lamination. It should be noted in the absence of the sufficient axial stress, the shale samples may fail along the bedding plane and not due to fracture initiation and propagation. This can complicate the interpretation of the experimental results. In order to apply the axial stress on the sample, a clamping tool was designed for shale experiments (Figure 4d).

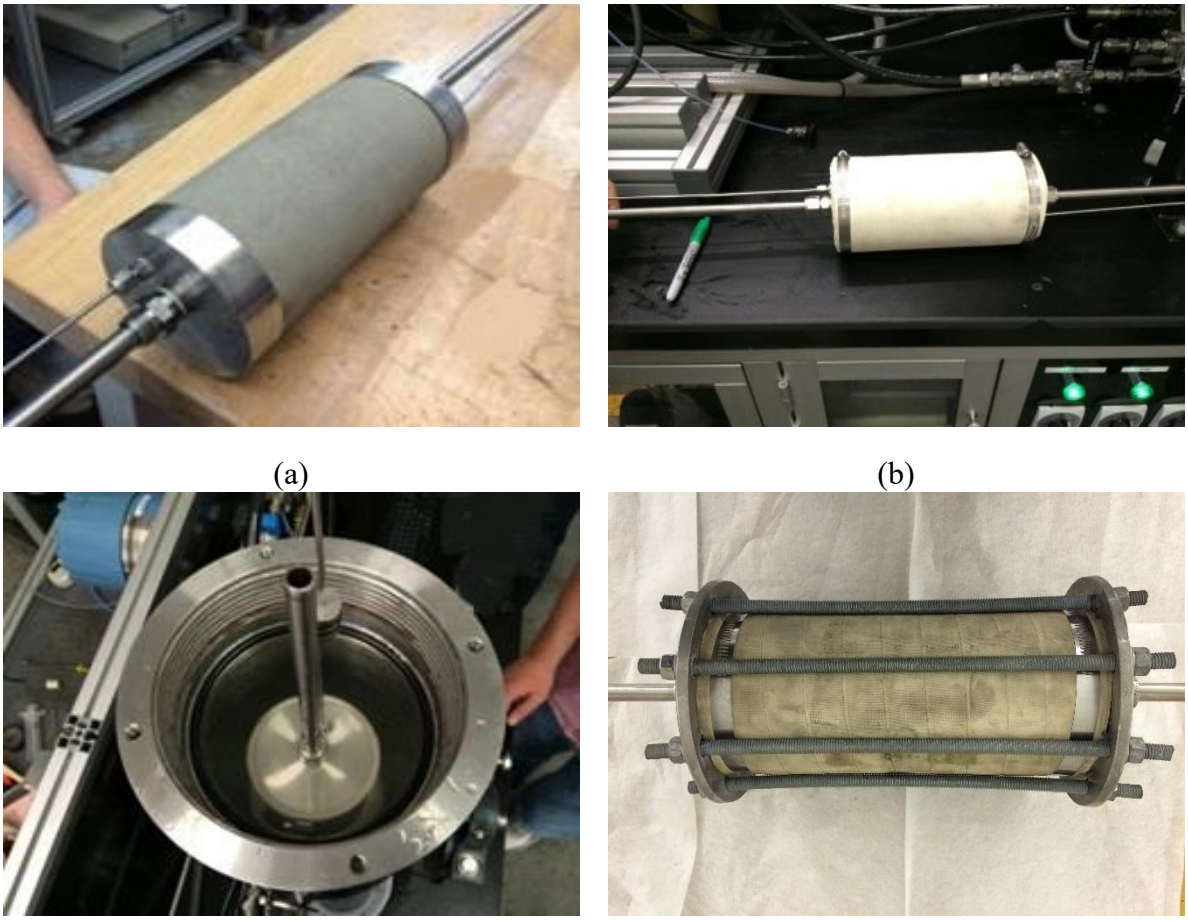

(a) (b)

(c) (d)

Figure 4 – Cylindrical rock sample used in the UT MudFrac system: (a) rock sample with end caps; (b) sample mounted in the radial confining sleeve; (c) sample loaded into the test vessel; (d) clamping tool used for shale experiments.

Positive displacement pumps were used to control borehole injection pressure, pore pressure, and confining pressure. Utilizing proportional integral derivative control algorithms and high performance motion control hardware, the system can accurately control several independent process variables (e.g., the pressure and flow-rate of injection, pore, and confining pumps). In addition, safety shut downs were hard-coded in the process control system. The data acquisition system records mud density, temperature, pressure and flow rate in real-time.

4.2 Rock and Fluid Samples

Three types of rocks were selected to represent permeable and impermeable formations: Berea Sandstone (permeable), Castlegate Sandstone (permeable), and Mancos Shale (impermeable). The material properties of the samples were presented in Table 2. Permeability, porosity, and UCS values were provided by the supplier of the rock samples (Kocurek Industries Inc.). The elastic moduli (Young's modulus and Poisson's ratio), Brazilian tensile strength, and fracture toughness values of Berea sandstone and Castlegate sandstone were measured separately and in the direction perpendicular to the bedding plane of the samples. Castlegate sandstone samples have a significantly higher permeability than Berea sandstone samples, as indicated in Brine and Gas permeability values. Berea sandstone samples are significantly stiffer than Castlegate sandstone samples, as indicated in the measured Young's modulus. Also, Berea sandstone samples have a higher Brazilian tensile strength and fracture toughness. The selected rock types provide the opportunity to investigate the effect of stiffness and permeability on the WBS effects.

Two WBMs (Glycol-based and KCl-based) and one SBM were used as the base fluid systems to perform experiments. All tests were conducted using 12 ppg mud density.

Barium sulfate (Barite) was used as the weighting agent. Commercial grades of graphites, cellulosic fibers and Gilsonites that are routinely used in field practice for lost circulation control purposes were used in this investigations. Rheological properties of the drilling fluids were measured before and after each experiment. Typical values of plastic viscosity, yield point, and 10 seconds gel strength for the three base mud systems were presented in Table 3.

Measured Property	Berea Sandstone	Castlegate Sandstone	Mancos Shale
Brine Permeability (md)	105	750	$<10^{-6}$
Gas Permeability (md)	300	900	$<10^{-6}$
Porosity (percent)	18	28	3.7 – 7.9
UCS (psi)	6500	2400	8000
Young's Modulus (psi)	2.0×10^6	0.3×10^6	-
Poisson's Ratio	0.25	0.3	-
Brazilian Tensile Strength (psi)	404	150	-
Fracture Toughness ($psi\sqrt{in}$)	237	291	-

Table 2 – Typical properties of the rock samples in this study: brine permeability, gas permeability, and porosity values were provided by the supplier of the rock samples (Kocurek Industries Inc.), and UCS, Young's modulus, Poisson's ratio, Brazilian tensile strength, and fracture toughness values were measured independently and perpendicular to the bedding plane

Drilling Fluid System	SBM	KCl-Based WBM	Glycol-Based WBM
Plastic Viscosity (cp)	24	24	42
Yield Point (lb/100ft^2)	21	21	17
10-Sec Gel Strength (lb/100ft^2)	9	6	13

Table 3 – Typical rheological properties of the drilling fluid systems used for WBS experiments

4.3 Testing Procedure: Measurement of the FIP and FPP

Each fracturing experiment with the UT MudFrac system included one fracture initiation and five fracture propagation injections on an intact rock sample. Fracture initiation injection was performed by pressurizing the borehole at a rate of 0.1 cc/sec and under either 10 or 100 psi confining pressure. Subsequently, fracture propagation injections were carried out on the sample at a rate of 0.1 cc/sec and under 100, 200, 300, 400, and 500 psi confining pressures. All experiments were conducted at room temperature.

The results of a fracturing experiment on a Berea sandstone sample are presented in Figure 5, in which injection, pore, and confining pressures are plotted against the injection volume. The fracturing experiment was conducted at 10 psi of confining pressure. Since the pore line was open to the atmosphere, pore pressure readings remained very close to the atmospheric pressure during the injection (i.e., pore pressure build-up was dissipated through the pore line). Fracture initiation was started by shutting in the flow loop and intensifying pressure in the wellbore by injecting additional drilling fluid into the closed loop at the rate of 0.1 cc/sec. The FIP is marked by a distinct peak in the injection pressure (approximately 730 psi), and followed by a sudden drop in the injection pressure and a

simultaneous jump in confining pressure. Subsequently the fracturing experiment reached the propagation phase, which is marked by consecutive cycles of injection pressure ramp-up to a local maximum, followed by a sudden pressure drop. As discussed in Section 2.1, these local peaks in the borehole pressure correspond to instants of fracture re-opening and propagation. Two stages of fracture propagation were observed: a transient and a stable stage. The transient propagation stage is indicated by a decreasing trend in the consecutive local pressure maxima (as marked in Figure 5). As discussed in Section 2.1, the decline of FPP during the transient stage is due to propagation of fracture in the radial direction. The induced fracture reached the outer surface of the rock sample at approximately 41 cc injection volume, as indicated by pressure communication between the injection and confining pumps. This is the injection volume which correspond to the beginning of the stable propagation stage. As expected, the FPP became relatively constant during the stable stage. Since the induced fracture reached the outer surface of the sample, the stable FPP in our experiments was only affected by the pressure required for re-opening of the formed seals and fracture propagation along the sample length. Thus, the measured FPP during the stable stage presents a lower-bound estimation of the actual stable FPP in the field. This is because the actual stable FPP in the field requires additional pressure for tip advancement in the radial direction. However, for large DIFs, the difference between the measured and actual FPP is negligible. This is because a long DIF requires a lower pressure for tip advancement (van Oort and Razavi, 2014). Also, when using LCM, the pressure required to break the formed seals and reopen the fracture increases significantly, which makes the effect of tip advancement even less important. Hence, the stable FPP in our experiments may be used as a conservative (lower-bound) estimation of the FPP to study the fracturing behavior of various rock samples, drilling fluid systems, and LCM blends.

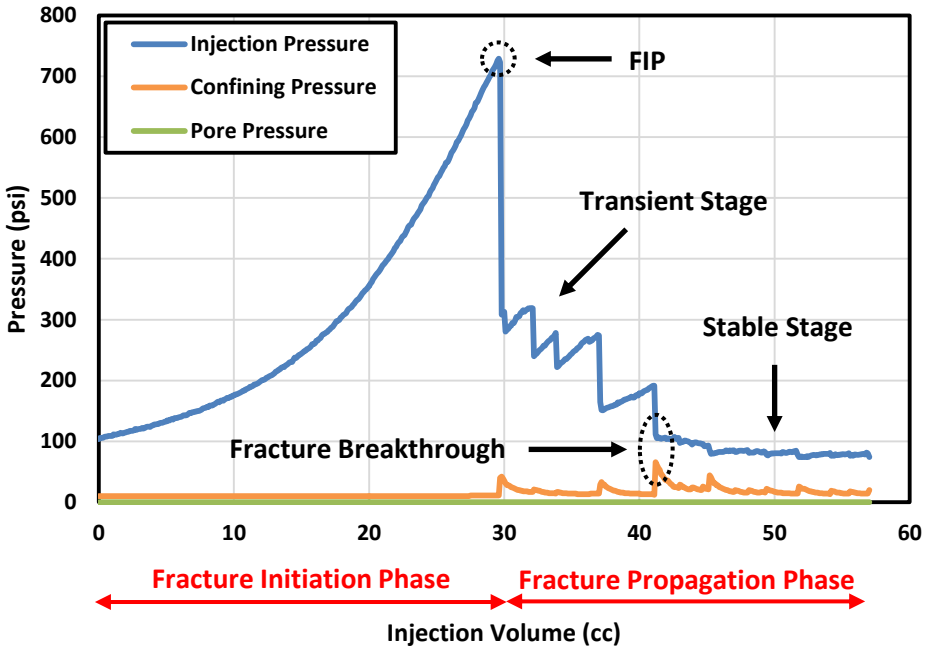

Figure 5 – Fracturing experiment on a Berea sandstone sample. Note that the fracturing experiment includes two phases: initiation and propagation. The FIP is marked by a peak in the injection pressure. The propagation phase includes two stages: transient and stable. Fracture breakthrough occurred at approximately 41 cc injection volume, as indicated by the pressure communication between the injection and confining pumps.

Fracture propagation injections were carried out to characterize the stable FPP at various confining pressures. Figure 6 presents five fracture propagation injections conducted at 100, 200, 300, 400, and 500 psi confining pressures. Each fracture propagation injection included several consecutive cycles of injection pressure ramp up to a local maximum (i.e., the FPP), followed by an immediate pressure drop. As discussed before, each of these cycles correspond to moments of fracture re-opening and propagation. Our experiments showed that a single re-opening and propagation cycle does not provide a reliable estimate of the stable FPP. Instead, the stable FPP is best characterized by performing several consecutive cycles. Thus, for each propagation injection, a certain

injection volume is required to reliably determine the stable FPP. This also indicates that a minimum volume of fluid filtration is required for seal formation along the fracture length. Furthermore, performing consecutive fracture propagations is an effective method to identify any experimental artifacts caused by flow-line clogging, which may result in unrealistically high FPP values. In order to perform consecutive fracture re-opening/propagation cycles, it is crucial for the pressure control system to re-adjust to the original confining pressure immediately after each cycle. The UT MudFrac System has the capability to automatically control the confining pump and maintain a constant confining pressure throughout the propagation injections. A relatively slow injection rate is also desirable to provide enough time for the confining pump to adjust the confining pressure after each cycle. For this experimental set-up, it was found that 0.1 cc/sec is the best suitable injection rate to perform the fracture propagation injection. In Figure 6, the FPP for each propagation cycle is marked using a red circle. In order to obtain a reliable estimation of the stable FPP value, the average stable FPP value was determined by calculating the arithmetic mean of local pressure maxima. The obtained average stable FPP values are then shown in Figure 6 using a red dashed line. It should be noted that the average stable FPP value refers to the average value of the local maxima in the injection pressure curve. Therefore, minor fluctuations in the injection pressure are disregarded as they do not reflect a realistic estimation of the stable FPP. Also, as discussed in this section, the propagation injections conducted in this study measured the FPP in the stable stage. Thus, for the sake of simplicity, the term “average FPP” is used exclusively to refer to the average stable FPP in this dissertation.

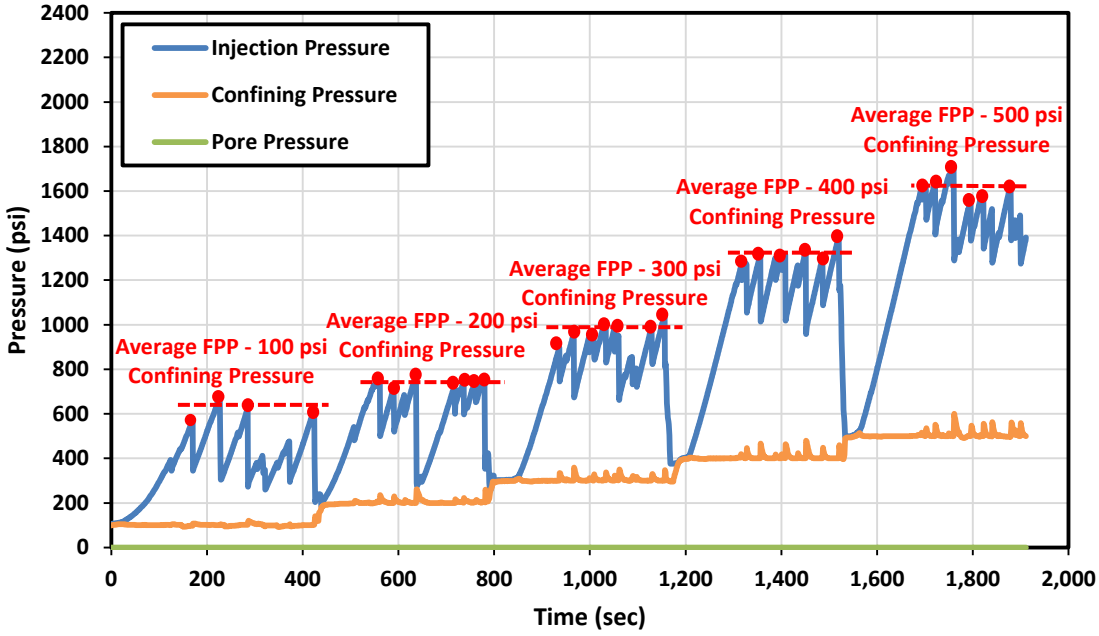

Figure 6 – Fracture propagation injections on a Berea sandstone sample using 100, 200, 300, 400, and 500 psi confining pressures. The local peaks in the injection pressures, which correspond to moments of fracture re-opening and propagation, are marked using red dots. For each confining pressure, the average FPP is indicated using a red dashed line.

Two distinct regimes of fracture growth were identified during the fracturing experiments. Initially, a fracture was created perpendicular to the borehole and grew relatively quickly to the boundaries of the sample (Figure 7a). Since no horizontal stress anisotropy was applied to the sample, the fracture direction in horizontal plane was determined predominantly by the orientation of pre-existing micro-fractures and strength variation in the intact samples. Subsequently, the created fracture grew in height (i.e., along the sample length) during the fracture reopening and propagation injections (Figure 7b). In order to study the geometry of the created fracture during fracture initiation and transient propagation stage, in a number of experiments, fluid injection was stopped immediately after the fracture breakthrough and the sample was unloaded and photographed (Figure 7c).

As expected, the created fracture propagated in the radial direction and reached the boundaries of the sample. However, the created fracture has a limited height, as shown Figure 7c. In contrast, it was observed that when the fluid injection was continued after the fracture breakthrough the fracture propagated along the length of the sample (Figure 7d).

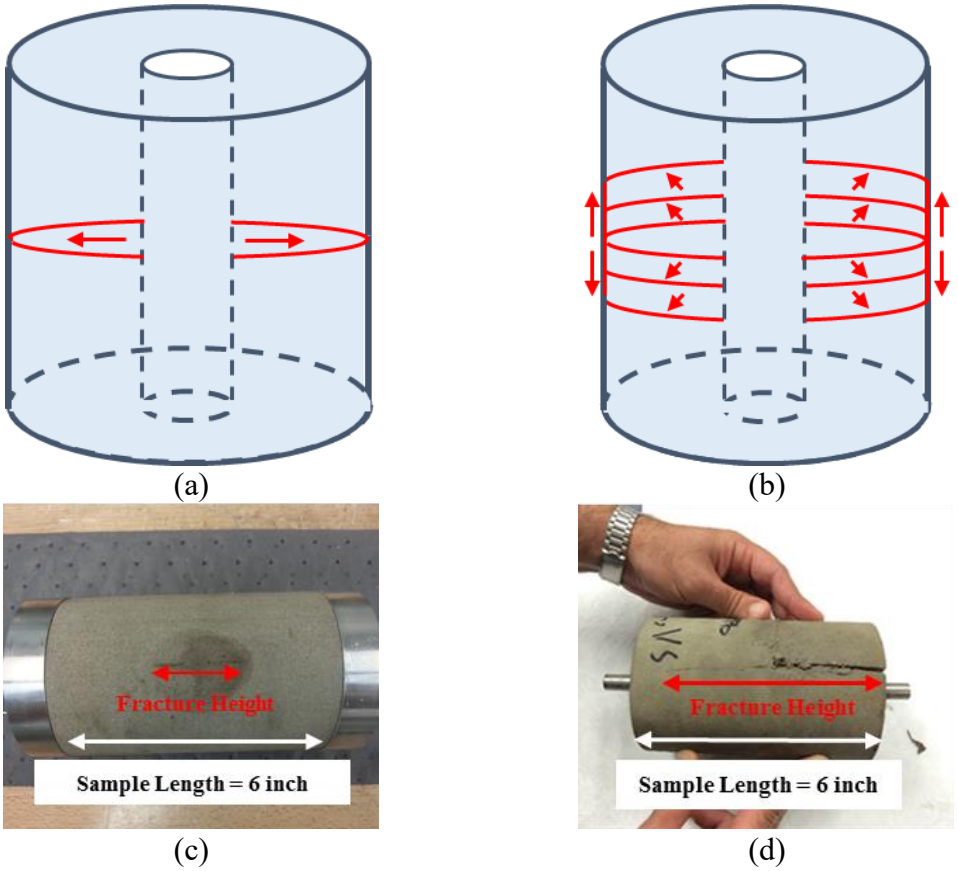

Figure 7 – Fracture growth during fracture initiation and propagation phases. (a) The schematic of fracture growth during fracture initiation and transient fracture propagation stage: the created fracture initially grew in the radial direction. (b) The schematics of fracture growth during stable fracture propagation stage: fracture propagated along the sample length. (c) Fractured sample after the fracture initiation and transient fracture propagation stage: note the limited fracture height at sample mid-length. (d) Fractured sample after the stable fracture propagation stage: the fracture propagated along the length of the sample.

4.4 Validation Experiments

Validation experiments were performed to critically examine sample preparation and testing procedure. Fracture initiation and propagation injections were conducted using SBM and Glycol-Based WBM fluids (without any LCM) on Berea sandstone samples. Subsequently, WBS experiments were conducted by adding 20 ppb of a graphite-based LCM blend (developed in a previous study by van Oort et al., 2011) to both tested fluids. Figure 8a shows the fracture initiation curves for the validations tests, including the results for both mud types with and without LCM. FIP was observed to be relatively constant for these tests taking into account the expected experimental error and the natural variation in strength among Berea sandstone samples. FIP is clearly independent of drilling fluid type or formulation. This is in full agreement with the results of the DEA 13 investigation (Onyia, 1994). In addition, the obtained results indicate that adding LCM materials to the base muds does not appear to change the near-wellbore tangential stress (hoop stress), since the FIP is the same for tests with or without LCM. The observed differences in the injection volume corresponding to the FIP are due to existence of air pockets in the testing equipment and variation in the compressibility of the tested fluids.

The results of fracture propagation injection at 500 psi confining pressures are compared in Figure 8b. The average FPP values for all validation experiments are presented in Table 4. Unlike FIP, the mud type and formulation can have a significant impact on FPP. The results show that a significant increase (>50% in our experiments) in FPP magnitude may be achieved by adding the proper LCM blends to the base fluid. In addition, the WBM shows higher FPP values than the SBM in both base test and strengthening tests (with LCM). As discussed in Section 2.3.2, this is because WBMs shield the pressure communication between the borehole and fracture tip more effectively

than SBMs. The obtained results from fracture propagation are again in full agreement with the DEA 13 (Onyia 1994) and the GPRI experiments (Dudley et al., 2000).

(a)

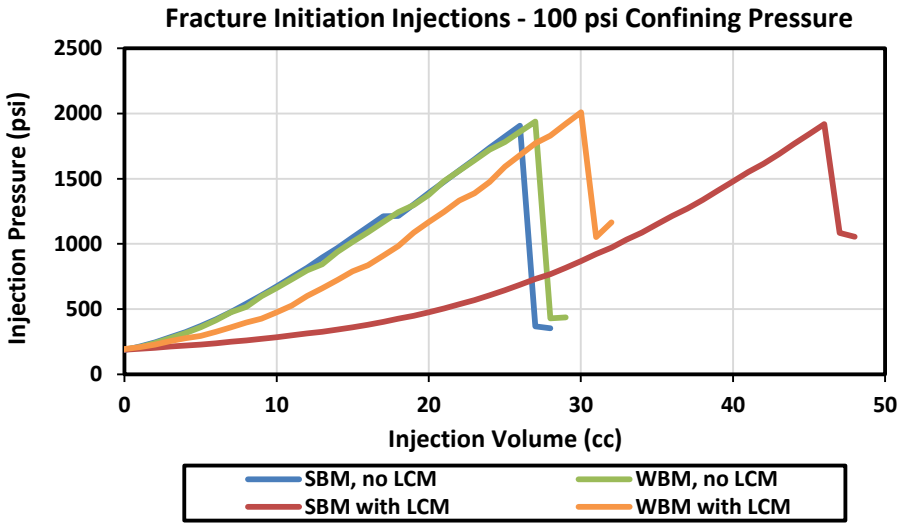

(b)

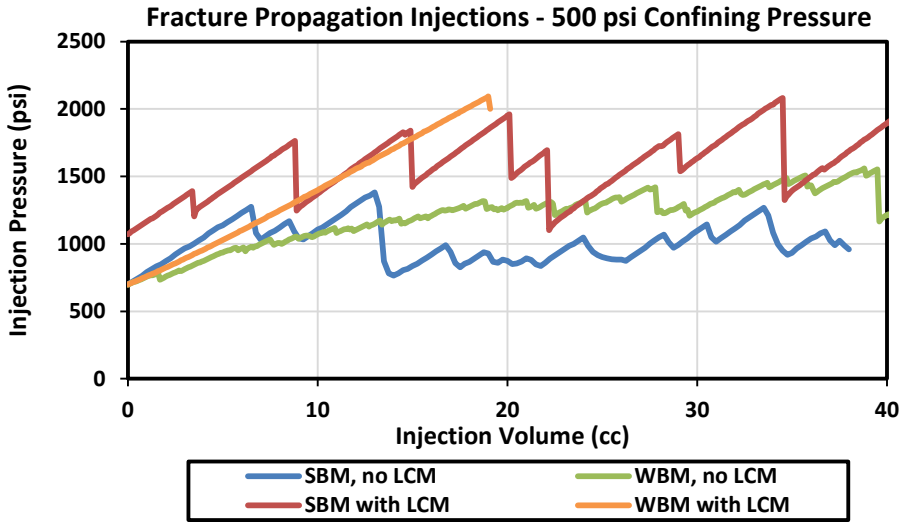

Figure 8 – Results of the validation experiments: (a) fracture initiation curves at 100 psi confining pressure; (b) fracture propagation curves at 500 psi confining pressure. All fracture initiation and propagation injections were conducted at 0.1 cc/sec.

Confining Pressure (psi)	Average FPP (psi)			
	SBM, no LCM	WBM, no LCM	SBM + LCM	WBM + LCM
500	1127	1424	1869	2097

Table 4 – Average FPP values measured in the validation experiments

CHAPTER FIVE: RESULTS AND DISCUSSION

5.1 Experimental Results in Permeable Formations

5.1.1 The Effect of LCM Particle Size Distribution

As discussed in the literature review section, PSD is one of the major parameters affecting the sealing capabilities of an LCM blend. To investigate the effect of PSD on WBS, three different grades of graphite-based LCMs were tested: unimodal fine and coarse grades were tested individually. They were also mixed (with a ratio of 10 to 7 for coarse and fine grades, respectively) to form a bimodal "medium" grade, which was also tested. A small amount (3 ppb) of a fine cellulosic fiber was added to all three grades. Figure 9 presents the PSD and cumulative PSD curves of the tested LCM grades. Particle size parameters such D_{10}, D_{25}, D_{50}, D_{75}, D_{90}, Standard Deviation (SD), relative span, and quartile ratio are given for each blend in Table 5. The medium and coarse blends have a similar SD, which is larger than the fine blend. The medium blend contains effective concentrations of both fine and coarse particles, due to its bimodal PSD. This is clearly indicated by the measured PSD parameters of the tested blends:

(1) The fine and medium blends have similar D_{10} and D_{25} values.

(2) The coarse and medium blends have similar D_{75} and D_{90}.

(3) The medium blend has the highest quartile ratio.

Parameter	D_{10} (µm)	D_{25} (µm)	D_{50} (µm)	D_{75} (µm)	D_{90} (µm)	SD (µm)	Relative Span $(\frac{d_{90}-d_{10}}{d_{50}})$	Quartile Ratio $(\frac{d_{75}}{d_{25}})$
Fine	23	44	83	157	300	196	3.34	3.57
Medium	31	81	217	463	641	284	2.81	5.72
Coarse	74	217	373	574	714	276	1.72	2.65

Table 5 – Particle size parameters of the tested graphite-based LCM blends

(a)

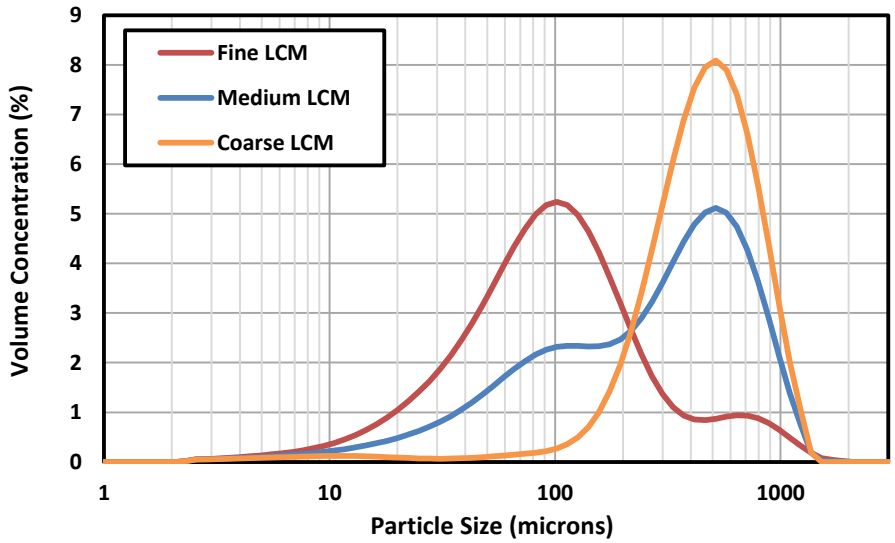

(b)

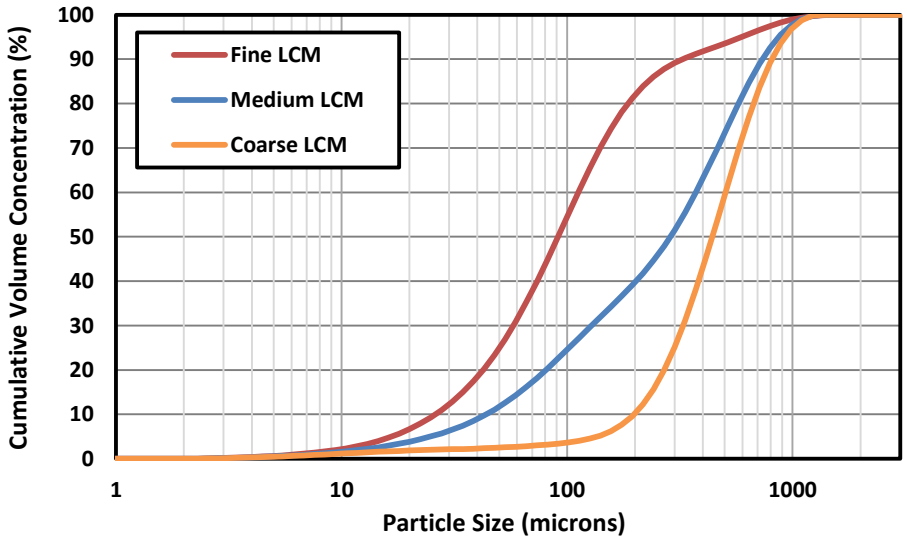

Figure 9 – Particle size analysis of the tested graphite-based LCM blends: (a) PSD of the LCM blends; (b) Cumulative PSD of the LCM blends.

Fracturing experiments were conducted using SBM base fluid (no LCM) and SBM with 20 ppb of fine, medium, and coarse LCM blends on Berea and Castlegate sandstone samples. Fracture propagation injection were performed at 100, 200, 300, 400, and 500 psi

confining pressures. Also, the value of average FPP was calculated for each confining pressure using the method explained in Section 4.3. Appendix I shows the fracture propagation injection curves for Berea sandstone (Figure A1a-e) and Castlegate sandstone (Figure A1f-j) at various confining pressures. In Figure 10, the average FPP is plotted against the confining pressure for Berea sandstone and Castlegate sandstone tests.

The experimental results indicate that, for both rock types, the medium grade LCM blend results in the highest FPP values compared to the fine and coarse grades, which give comparable results. This observation suggests that there exists a specific PSD (i.e., the medium LCM) which results in superior strengthening effects. Moreover, these results imply that any deviation from this specific PSD will lead to lower FPP values and strengthening effects. It is also clear that the LCM blend with a bimodal PSD provides higher strengthening effects, compared to LCM blends with a unimodal PSD. This important observation and its implications are explored further in this dissertation.

The dependence of the magnitude of the WBS effect on PSD has profound implications for field application. Not only do the optimum LCM PSD and concentration (see Section 5.1.3, the effect of LCM concentration) need to be determined for the mud formulations and mud weights employed as well as the rock formations drilled, they need to be rigorously maintained at optimum levels to achieve optimum strengthening benefits. However, most LCMs, typically in medium to coarser size ranges, undergo significant size degradation with applied shear, e.g. by shearing these materials through the nozzles of drill bits. It is important that this degradation is well-understood in real-time and managed accordingly. This subject is discussed in more detail by van Oort et al., 2016.

(a)

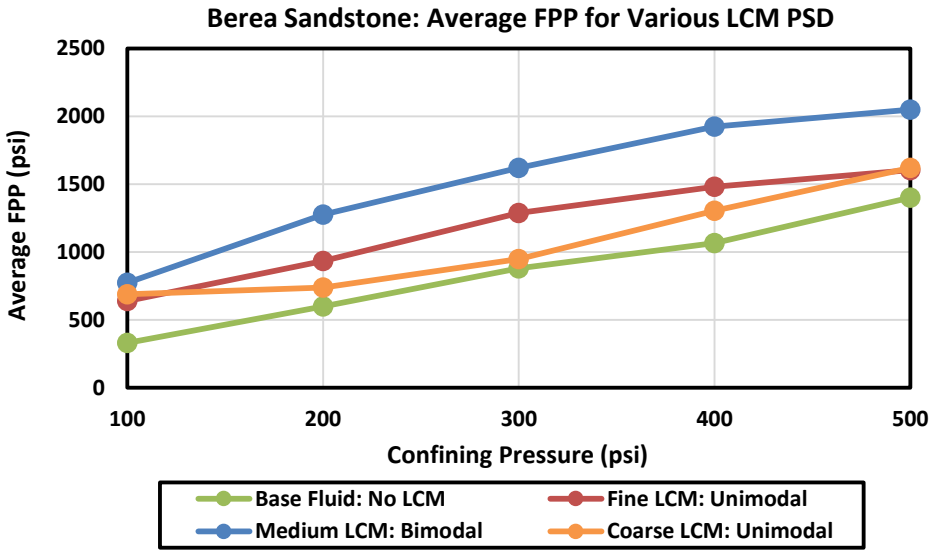

(b)

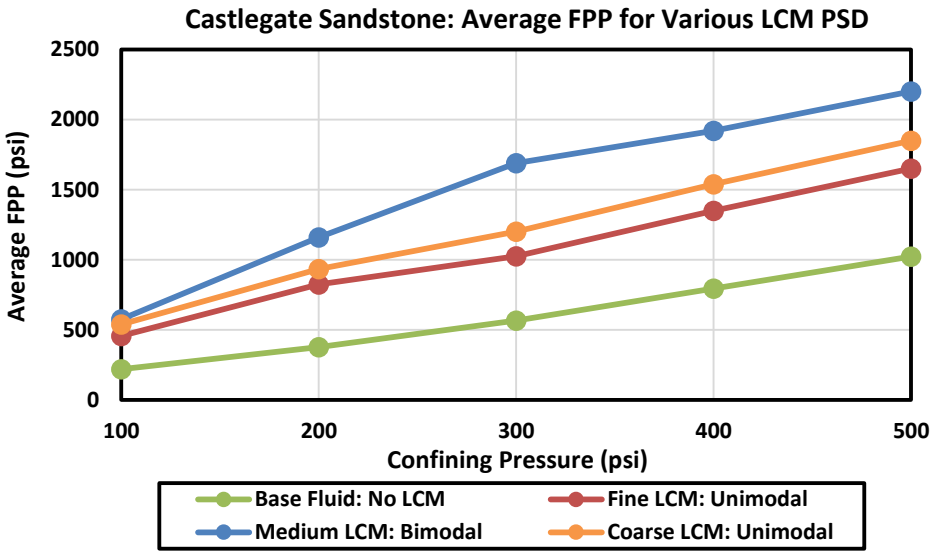

Figure 10 – Average FPP for Berea sandstone and Castlegate sandstone using various graphite-based LCM grades: (a) average FPP for Berea sandstone using base SBM (no LCM), and SBM with 20 ppb of fine, medium or coarse LCM blends; (b) average FPP for Castlegate sandstone using base SBM (no LCM), and SBM with 20 ppb of fine, medium or coarse LCM blends. Note that for both rock types, the bimodal medium LCM blend results in the highest FPP.

5.1.2 THE EFFECT OF LCM TYPE

To extend our findings on optimum LCM PSD, further tests were conducted using LCM blends which were not graphite-based. Gilsonite or Uintahite, a naturally occurring asphaltite, was selected for comparison. Two Gilsonite-based blends, labeled Gilsonite 1 and Gilsonite 2, were mixed to mimic the PSD of the optimum (medium) graphite-based blend. Figure 11 shows the PSD and cumulative PSD of these mixed Gilsonite-based blends. In Table 6, the particle size parameters of the Gilsonite blends are compared with those of the medium graphite-based blend. Note that all three blends have similar PSDs.

Two tests were conducted using Gilsonite 1 and Gilsonite 2 blends, with a concentration of 20 ppb on Berea sandstone samples. In Appendix II, the results of fracture propagation injections are presented and compared with the medium graphite-based blend (Figure A2). In Figure 12, the average FPP values are plotted against the confining pressure. Note that very similar FPP values may be observed using the Gilsonite-based blends and the medium graphite-based blend. This indicates that all three blends provide similar strengthening effects.

These experiments clearly show that the magnitude of the WBS effect is primarily determined by the PSD and to a much lesser extent by the type of LCM material. This may also explain why different scientists have reported favorable WBS results in field applications using a variety of different LCM types (e.g. Fuh et al. (1993), Alberty et al. (2008), etc.). The type of LCM may in fact be largely irrelevant (or at least less important) as long as the PSD is optimized.

(a)

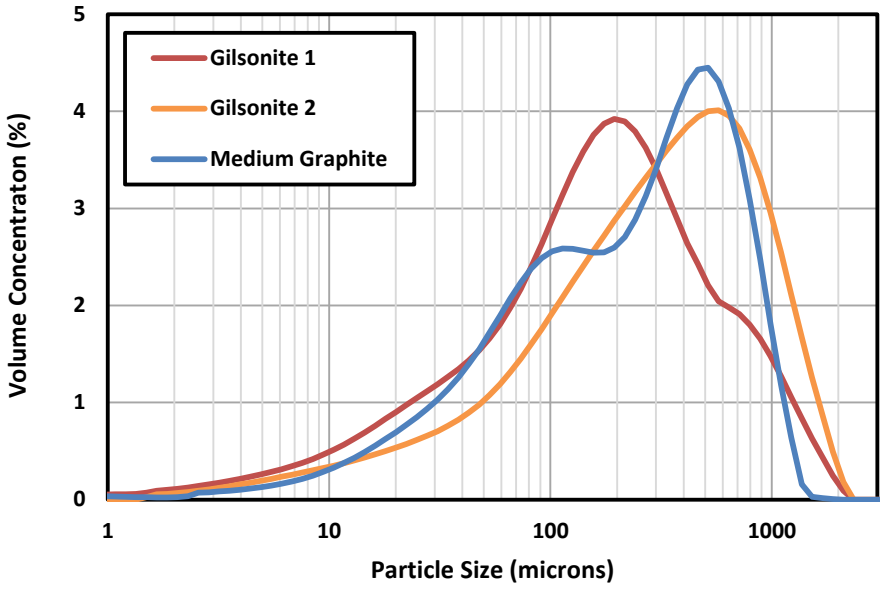

(b)

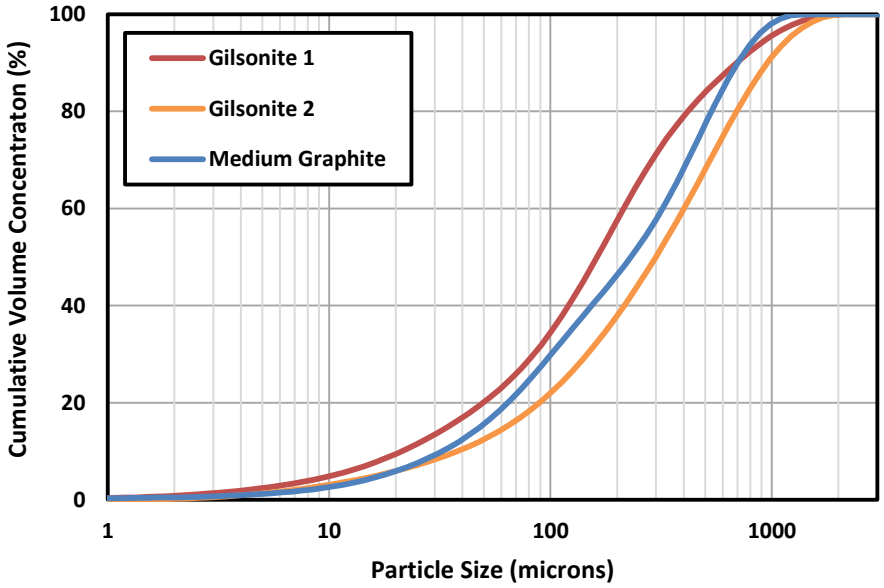

Figure 11 – Particle size analysis of the Gilsonite 1 and 2, and the medium graphite blends: (a) PSD of the tested blends; (b) cumulative PSD of the tested blends. Both Gilsonite blends have a PSD similar to that of the medium graphite blend.

Parameter	D_{10} (μm)	D_{25} (μm)	D_{50} (μm)	D_{75} (μm)	D_{90} (μm)	SD (μm)	Relative Span $(\frac{d_{90}-d_{10}}{d_{50}})$	Quartile Ratio $(\frac{d_{75}}{d_{25}})$
Gilsonite 1	21	66	157	335	641	328	3.95	5.08
Gilsonite 2	35	114	270	575	886	399	3.15	5.04
Medium Graphite	31	81	217	463	641	284	2.81	5.72

Table 6 – Particle size parameters of the medium graphite, Gilsonite 1 and 2 Blends

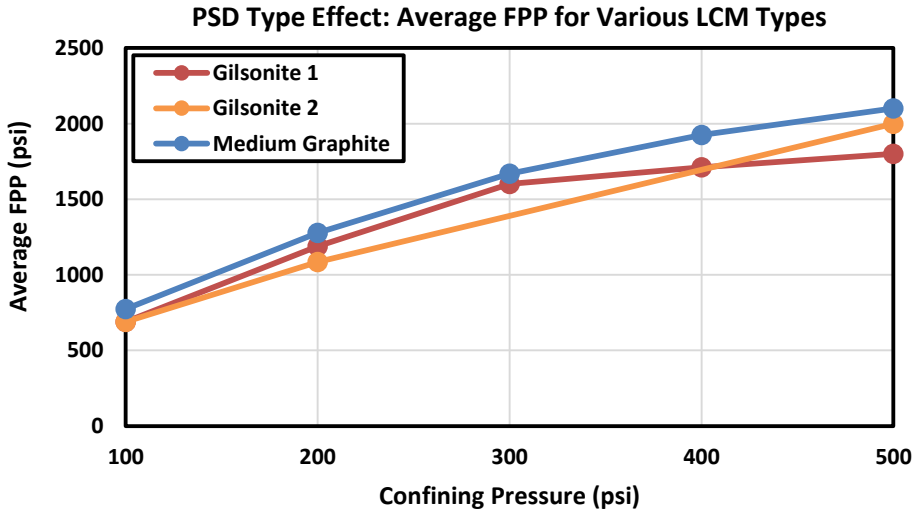

Figure 12 – Average FPP for the medium graphite, Gilsonite 1 and 2. Note that all three blends with similar PSD yield approximately equal average FPP. The results show that the FPP enhancement is primarily determined by the LCM PSD, not the LCM type.

5.1.3 The Effect of LCM Concentration

Considering practical application and plain economics, it is crucial to identify the optimum LCM concentration that achieves the maximum WBS effect. In this section, we investigate the optimum concentration for Castlegate sandstone and Berea sandstone using the medium graphite-based LCM blend discussed earlier. Fracturing experiments were

performed using SBM with the following LCM concentrations: 0 (no LCM), 10, 15, 20, and 30 ppb in Berea sandstone tests and 0 (no LCM), 5, 10, and 20 ppb in Castlegate sandstone tests. In Appendix III, the fracture propagation injections for Berea sandstone (Figure A3a-e) and Castlegate sandstone (Figure A3f-j) at various confining pressures are shown. Next, using the method explained in Section 4.3, the average FPP for each fracture propagation injection curve was determined. Figure 13 shows the average FPP against the confining pressure for Berea sandstone and Castlegate sandstone tests. For both rock types, increasing the LCM concentration results in higher FPP. However, beyond a certain concentration, no significant further increase in FPP was observed. In fact, for both rock types, there exists a certain LCM concentration threshold above which the FPP does not increase significantly. The obtained thresholds are the economic optimum LCM concentrations for field application. The optimum LCM concentrations for Castlegate sandstone and Berea sandstone are 10 and 20 ppb, respectively. Castlegate sandstone is significantly more permeable than Berea sandstone (as indicated in the brine and gas permeability values, Table 2). Therefore, it seems that the rock with higher permeability requires a lower optimum LCM concentration for strengthening. This is because a highly permeable rock has a higher fluid leak-off rate and associated solids screen-out rate. This facilitates plugging of solids in fractures. Therefore, effective strengthening benefits can be obtained using a relatively low LCM concentration. In contrast, a higher LCM concentration is required for successful solid plugging of fractures in formations with a lower permeability (theoretically reaching an infinite value for impermeable rocks, as discussed further below). Similar FPP values were observed in drilling fluids with LCM concentration equal to – or above – the optimum value in both Berea and Castlegate sandstone. This shows that both rock types have enough permeability for successful solid plugging of the fractures.

(a)

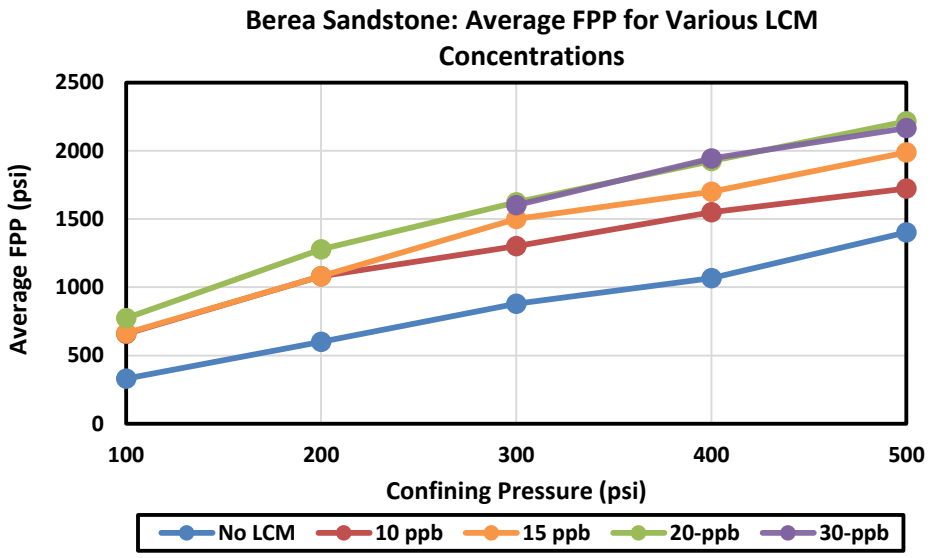

(b)

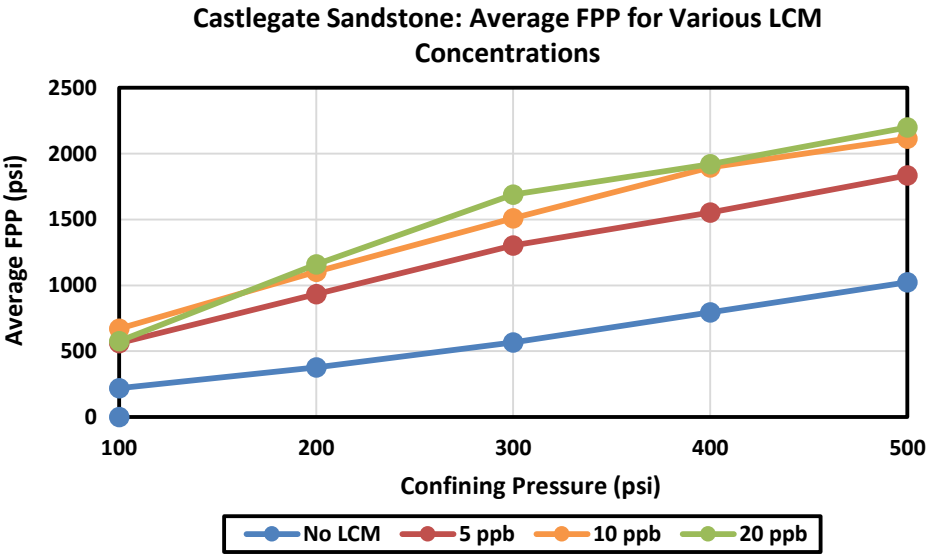

Figure 13 – Average FPP for Berea and Castlegate Sandstone using SBM loaded with various concentrations of medium graphite LCM: (a) average FPP for Berea sandstone using no LCM, 10, 15, 20, and 30 ppb LCM concentration; (b) average FPP for Castlegate sandstone using no LCM, 5, 10, 20 ppb of LCM concentration. The optimum LCM concentrations for Berea sandstone and Castlegate sandstone are 20 and 10 ppb, respectively.

5.1.4 THE EFFECT OF INJECTION VOLUME

There are contradictory views on the effect of injection volume in different WBS models / techniques. As discussed in Section 2.3.2, some WSA models, namely FCS, prescribe injecting a relatively large volume of LCM-laden fluids (pills) in a process known as a "hesitation squeeze" (Dupriest, 2005). It was discussed elsewhere (van Oort and Razavi, 2014) that from a theoretical standpoint large injection volume may result in a lower FPP. Instead, it is more effective to perform "continuous" WBS techniques to immediately arrest the propagation of the induced fractures.

In this study, we further investigate the effect of injection volume by conducting high-volume fracture propagation injections at 100 and 200 psi confining pressures. These injections were conducted using SBM with 20 ppb of medium graphite-based LCM on Berea sandstone samples. Furthermore, in order to evaluate the "healing" effect of LCM, the fracture propagation injections were repeated after 15 minutes at both confining pressures. Figure 14 shows the results of injection (borehole) pressure against the injection volume at 100 and 200 psi confining pressure. As shown in Figure 14, a minimum level of injection volume (approximately 20 cc) is required to reach the full sealing capacity of the LCM blend. However, injecting excess fluid beyond this level does not result in a higher FPP. In contrast, we observed a decreasing trend in the FPP in one of the fracture propagation injections (Figure 14a). The inspection of the sample after the experiment indicated that the excessive injection volume led to formation of a large fracture network which then resulted in loss of the sample integrity. Similar issues may occur by injecting a large hesitation squeeze volume in field applications. Furthermore, according to the obtained results, stopping the injection to "heal" the formation and repeating the injection does not result in a higher FPP value. Note that the Berea sandstone is largely inert and

does not react with drilling fluid in the same way that certain shales do. Therefore, no healing benefit is expected by stopping the circulation and waiting for "healing" to occur.

(a)

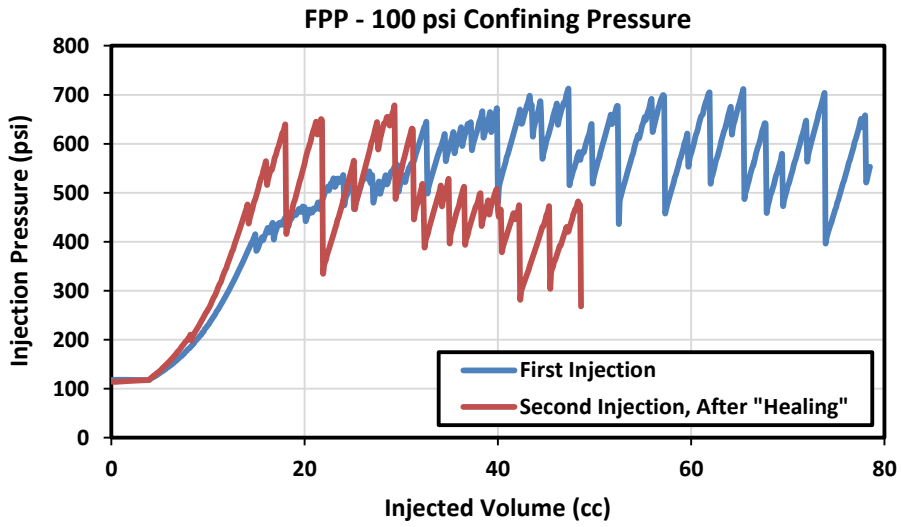

(b)

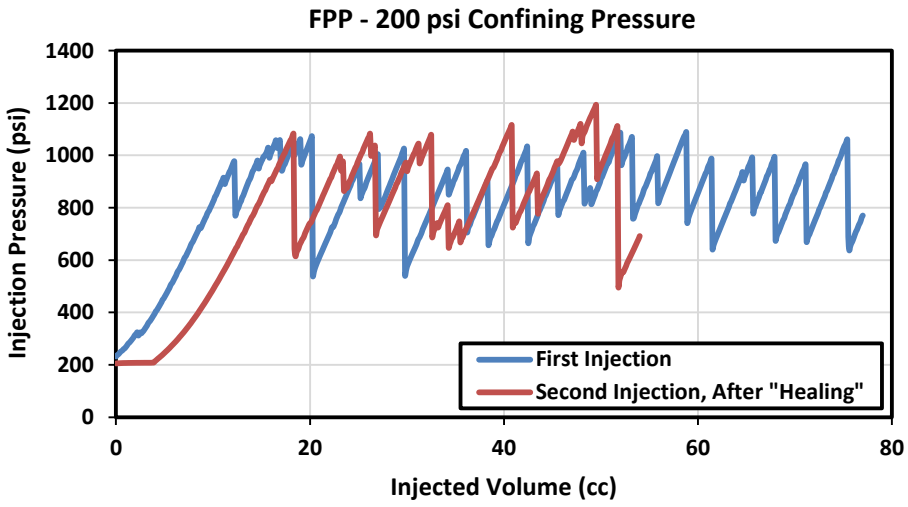

Figure 14 – Effect of the injection volume on the FPP: (a) fracture propagation injections at 100 psi confining pressure; (b) fracture propagation injections at 200 psi confining pressure. At both confining pressures, the second propagation injection was performed 15 minutes after the first injection to investigate the "healing" effect of the drilling fluid. No such effect was observed.

5.1.5 THE EFFECT OF FORMATION STIFFNESS

In this section, we study the effect of formation stiffness (Young's modulus) on maximum attainable strengthening benefits. As shown in Table 2, Berea sandstone is almost ten times stiffer than Castlegate sandstone. Thus, the effect of formation stiffness may be determined by comparing the fracturing behavior of these two rocks. The results of fracturing experiments using SBM without LCM and SBM with 20 ppb of medium graphite-based LCM are compared. The fracture propagation injection curves are shown in Appendix IV, Figure A4. In Figure 15, the obtained average FPP are plotted against the confining pressure for Berea sandstone and Castlegate sandstone. For base tests (SBM without LCM), Berea sandstone provided a slightly higher FPP than Castlegate sandstone. As expected, a significant increase in FPP was observed by adding LCM to the drilling fluid for both rock types. Furthermore, similar FPP values were observed for both rock types using SBM with LCM. In order to evaluate the effect of LCM more accurately, the obtained strengthening magnitudes were determined by calculating the difference between the FPP of SBM without LCM and SBM with LCM. Table 7 shows the obtained strengthening magnitude of the used LCM blends for both rock types. Overall, relatively similar strengthening magnitudes were observed in both rocks at lower confining pressures (100 and 200 psi). Moreover, Castlegate sandstone showed larger FPP enhancements at higher confining pressures. The obtained strengthening magnitudes may be used to evaluate the validity of the WSA model. As discussed in Section 2.3.2, the WSA model states that the strengthening effects are mainly dominated by the rock stiffness. Thus, according to this model, considerably larger strengthening effects are expected in Berea sandstone samples. However, no such difference between the strengthening magnitude in Berea and Castlegate sandstone was observed. In fact, the strengthening magnitudes in Castlegate sandstone were even higher at 300, 400, and 500 psi confining pressures.

Overall, the obtained experimental results indicate that the strengthening effects are mainly independent of the rock stiffness. This finding is in direct contradiction of the WSA model. Furthermore, it supports the FPR model which states that WBS is mainly independent of the rock stiffness.

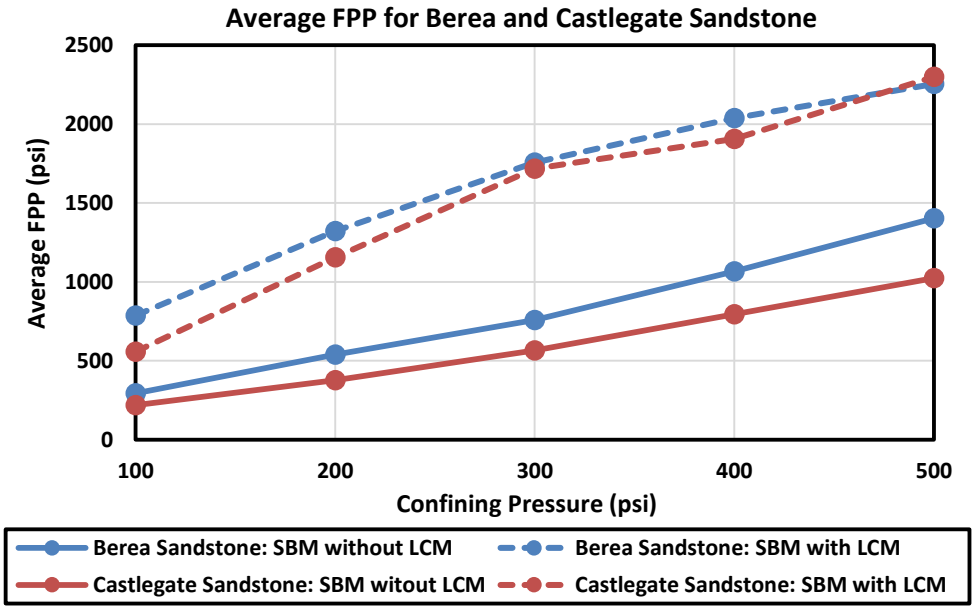

Figure 15 – Average FPP for Berea and Castlegate sandstone samples using SBM without LCM and SBM with 20 ppb of medium graphite-based LCM.

Confining Pressure (psi)	Strengthening Magnitude = $FPP_{SBM\ with\ LCM} - FPP_{SBM\ without\ LCM}$ (psi)	
	Berea Sandstone	Castlegate Sandstone
100	476	339
200	730	779
300	877	1151
400	971	1112
500	852	1275

Table 7 – The obtained strengthening magnitude using Berea sandstone and Castlegate sandstone

5.2 Experimental Results in Impermeable Formations

Fracturing experiments were performed on Mancos shale samples using various fluid systems to investigate the fracturing behavior of impermeable formations. Overall, four samples were tested using two SBMs (without LCM and with 20 ppb of graphite-based LCM) and two WBMs (Glycol-based and KCl-based). The test with LCM was conducted to evaluate the feasibility of applying conventional WBS techniques (which rely on LCM) to impermeable formations.

Figure 16 shows fracture initiation injection curves for four Mancos samples. A significant discrepancy in FIP values was observed in two shale samples, which were fractured using SBM without LCM and with LCM. However, it seems that the observed discrepancy in the FIP is due to heterogeneity of the samples (variation in the rock tensile strength), not the effect of applied LCM.

In Appendix V, the fracture propagation curves are shown for 100, 200, 300, 400, and 500 psi confining pressure. Using the procedure explained in Section 4.3, the average FPP values were calculated for each fracture propagation injection. The average FPP values are then plotted against the confining pressure in Figure 17a. The results show that in shale samples, WBMs do not appear to provide higher FPP values than SBMs. The results from the various tests were within a relatively tight band, with variations attributed to sample variability. Furthermore, addition of LCM did not increase the average FPP significantly. SBM with LCM showed slightly higher FPP at low confining pressure (100 psi). However, no major strengthening effects were observed at other confining pressures.

To further investigate the effect of LCM in impermeable formations, the average FPP values were compared in permeable and impermeable formations. Figure 17b illustrates the FPP values in Berea sandstone and shale samples using SBM without LCM

and with 20 ppb graphite-based LCM. Adding LCM to the drilling fluid has only minor effects on FPP enhancement in shale samples, whereas the effects on Berea sandstone is very significant. As explained by Morita et al. (1990) and van Oort and Razavi (2014), induced fractures in impermeable formations are highly unstable due to pore pressure build-up and lack of fluid leak-off through the rock matrix. The lack of fluid leak off also prevents formation of effective pressure barriers along the fracture surfaces. More research work is required to find viable WBS techniques for impermeable formations such as shales. It seems that effective WBS in shale requires radically different approaches which do not rely (or exclusively rely) on solid plugging of fractures.

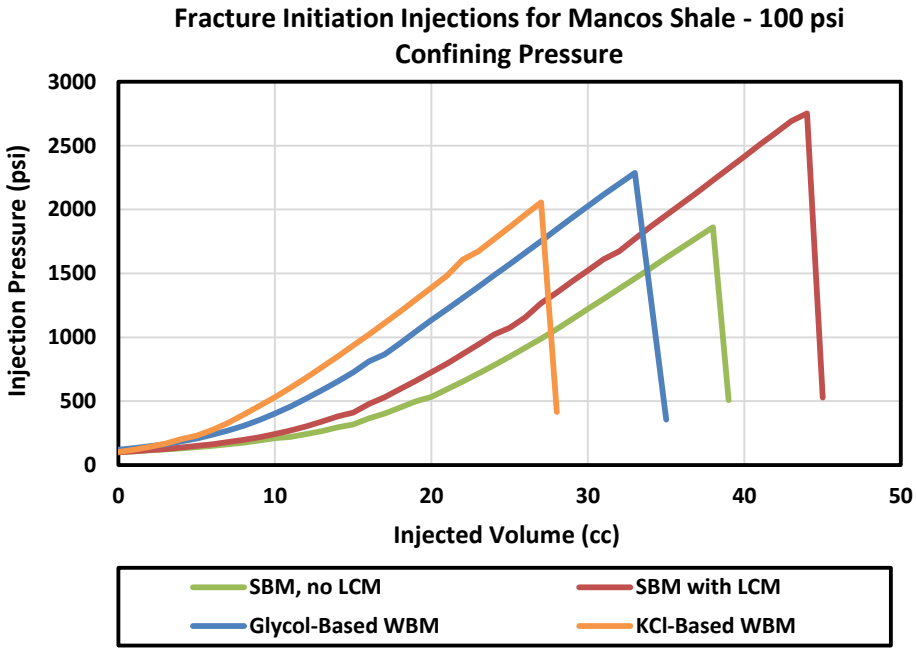

Figure 16 – Fracture initiation injections using Mancos shale samples at 100 psi confining pressure. The peaks at each injection pressure curve indicate the FIP. Note that the discrepancy in the measured FIP values are due to variation in the rock tensile strength, not the drilling fluid formulations.

(a)

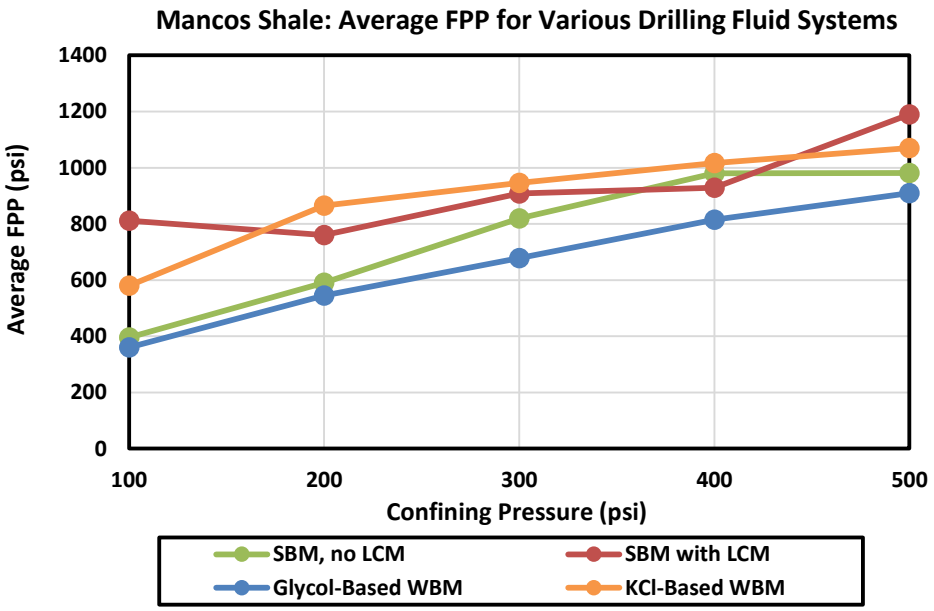

(b)

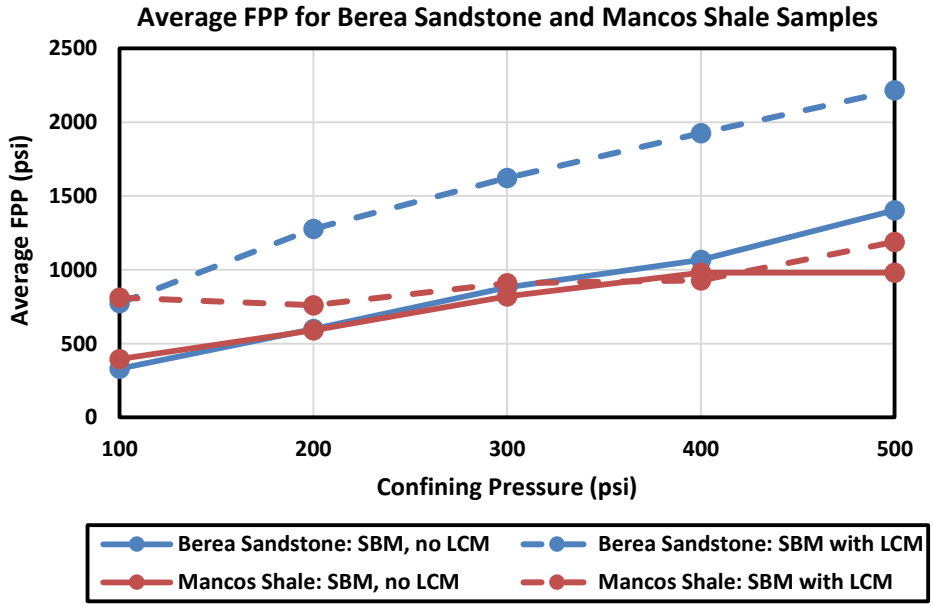

Figure 17 – Average FPP using Mancos shale samples: (a) the average FPP of Mancos shale samples using various mud systems; (b) the average FPP of Berea sandstone and Mancos shale samples using SBM with and without LCM. Note that unlike Berea sandstone, no discernable strengthening benefit was observed in Mancos shale using SBM with LCM.

5.3 FIP Analysis: Theoretical vs. Experimental Results

In this section, the results of fracture initiation injections in permeable formations (Berea and Castlegate sandstone) are compared with well-known theoretical models for FIP. The results of Mancos shale FIP are not analyzed due to sample variability, as indicated in significantly different tensile strength and fracture toughness values in each sample. Fracture initiation injections were conducted using Berea sandstone samples at 10 and 100 psi confining pressures. Also, the FIP was measured using Castlegate sandstone at 100 psi confining pressure. In order to study the effect of pre-existing fractures in the vicinity of the borehole, fracture initiation injections were conducted using two different borehole geometries: un-notched and notched. The notched samples have two similar cuts on opposite sides of the borehole, with an approximate length of 0.25 inch and width of 0.1 inch. Figure 18 shows the results of CAT scan imaging of the borehole cross section for both un-notched and notched samples, prior to fracturing experiments.

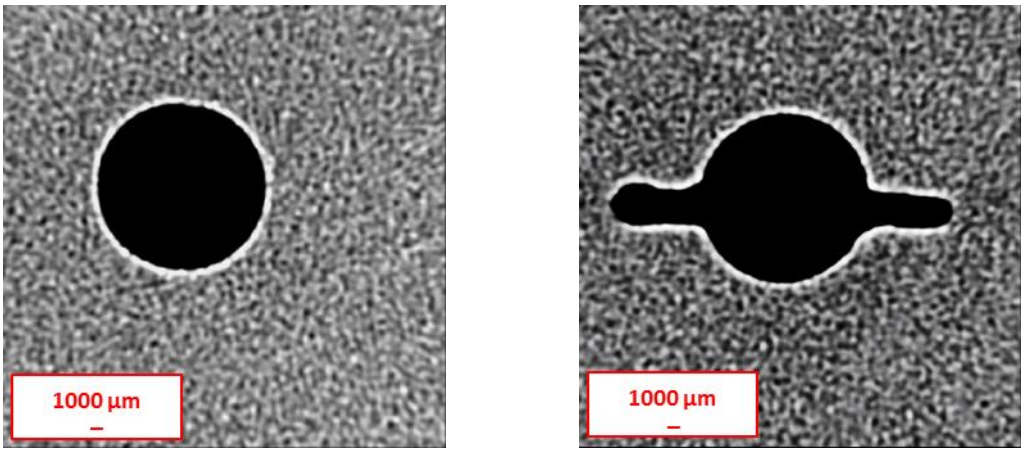

(a) (b)

Figure 18 – CAT scan imaging taken from the borehole cross section of Berea sandstone samples: (a) un-notched sample; (b) notched sample.

Figure 19 shows the results of fracture initiation injections on Berea sandstone and Castlegate sandstone. Furthermore, the values of obtained FIP are reported in Table 8. As expected, notching the samples in all tested confining pressures and rock types results in reduction of the FIP. This is because the created notches facilitate the initiation of the fractures. Moreover, inspection of the tested samples indicates that the created fracture was propagated in the notching direction. The obtained FIPs in this section are further analyzed in the following sections through comparison with theoretical models for fracture initiation.

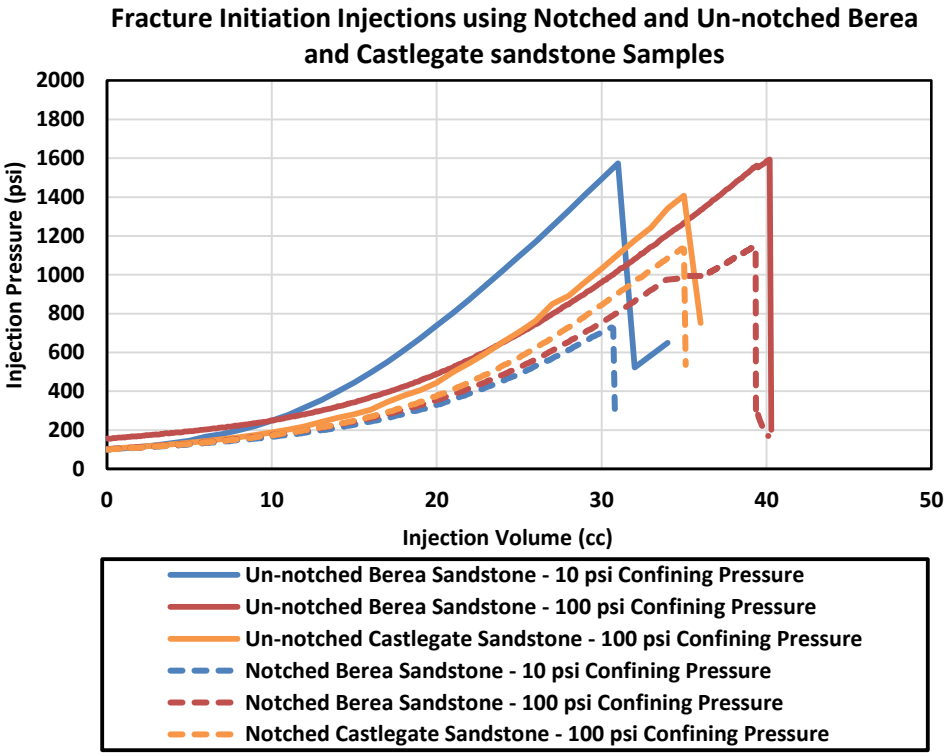

Figure 19 – Fracture initiation injection curves using Berea and Castlegate sandstone. Note that for all tested confining pressures and rock types, notched samples show a lower FIP value than the un-notched samples.

Sample Type	Confining Pressure (psi)	FIP (psi)	
		Un-notched	Notched
Berea Sandstone	10	1594	729
	100	1624	1145
Castlegate Sandstone	100	1408	1136

Table 8 – The values of the FIP using Berea and Castlegate sandstone for un-notched and notched samples

5.3.1 HUBBERT AND WILLIS' MODEL

As explained in Section 2.3.1, Hubbert and Willis (1957) employed Kirsch's (1898) solution for stress distribution around the borehole. Their model, which relies on the theory of elasticity, states that borehole fracturing occurs when the fluid pressure counterbalances the tangential stress of the borehole and exceeds the tensile strength of the rock. According to Hubbert and Willis' model, the FIP is given by:

$$\mathrm{FIP} = 3S_{\mathrm{hmin}} - S_{\mathrm{hmax}} - P_P + T_0 \qquad \text{(Eq. 1)}$$

in which S_{hmin}, S_{hmax}, P_P, and T_0 are the effective minimum horizontal stress, the effective maximum horizontal stress, pore pressure, and rock tensile strength, respectively.

Since the fracture initiation injections were conducted at isostatic confining pressure and atmospheric pore pressure in our experiments, S_{hmax} and S_{hmin} are equal to the confining pressure. Thus, Hubbert and Willis' equation can be simplified to:

$$\mathrm{FIP} = 2\sigma_{\mathrm{confining}} + T_0 \qquad \text{(Eq. 2)}$$

Table 9 compares the theoretical FIP as predicted by the Hubbert and Willis' model with the measured values. A significant discrepancy is observed between the model's

prediction and the measured FIP. This is because Hubbert and Willis' model is a relatively simplistic approach to estimate the FIP and it ignores the effects of borehole size and pre-existing fractures in the vicinity of the borehole. Furthermore, this model cannot be used to estimate the FIP for notched borehole since it does not consider the effect of the fractured borehole geometry. These results may also suggest that the measured Brazilian tensile strengths do not provide a realistic estimate of the samples resistance to fracture initiation.

Sample Type	Confining Pressure (psi)	P_P (psi)	T_0 (psi)	FIP (psi)	
				H&W Model	Measured
Berea Sandstone	10	0	404	424	1594
	100	0	404	604	1624
Castlegate Sandstone	100	0	150	350	1408

Table 9 – Comparison between the measured and theoretical FIP for un-notched samples, using Hubbert and Willis' model

5.3.2 RUMMEL'S MODEL

Rummel (1987) employed a fracture mechanics approach to derive a closed-form solution for FIP. Using the principle of superposition, his model incorporates the effects of maximum and minimum horizontal stresses, wellbore pressure, and fracture pressure (Figure 20). According to his model, FIP is given by:

$$\mathrm{FIP} = \frac{1}{h_0 + h_a}\left[\frac{K_{IC}}{\sqrt{R}} + S_{hmax}f + S_{hmin}g\right] \qquad \text{(Eq. 3)}$$

where:

h_0 is the dimensionless stress intensity factor for fluid pressure within the wellbore, and given by:

$$h_0(b) = 1.3\frac{b-1}{1+b^{\frac{3}{2}}} + 7.8\frac{\sin(\frac{b-1}{2})}{2b^{\frac{5}{2}} - 1.7} \quad \text{(Eq. 4)}$$

b is the dimensionless length parameter:

$$b = 1 + \frac{a}{R} \quad \text{(Eq. 5)}$$

h_a is the dimensionless stress intensity factor for pressure distribution within the fracture. There are contradictory hypotheses regarding the fluid pressure distribution within the pre-existing fractures prior to fracture initiation. Some sources suggest that the borehole fluid does not penetrate into the pre-existing fractures prior to fracture initiation (Morita et al., 1996). In contrast, there are models which propose that the pressure at the pre-existing fractures is disturbed by the borehole pressure prior to fracture initiation. To examine these hypotheses, Rummel's model was applied for two different cases: un-invaded pre-existing fractures and fully invaded pre-existing fractures. In the un-invaded pre-existing fracture case, it was assumed that the borehole pressure does not penetrate into the pre-existing fractures. Thus, the pressure at the pre-existing fractures is equal to the pore pressure. In the fully invaded pre-existing fracture hypothesis, full borehole pressure penetration into the pre-existing fractures was assumed. Thus, the pressure at the pre-existing fracture is equal to the borehole pressure. Since the fracture initiation injections were conducted at atmospheric pore pressure, for un-invaded pre-existing fracture assumption, h_a is given by:

$$(h_a)_{un-invaded} = 0 \quad \text{(Eq. 6)}$$

According to Rummel's model, for fully invaded pre-existing fracture assumption, h_a is given by:

$$(h_a)_{invaded} = \sqrt{\pi b}\,[1 - \frac{2}{\pi}\sin^{-1}\frac{1}{b}] \quad \text{(Eq. 7)}$$

where f and g are dimensionless stress intensity factors for maximum and minimum horizontal stresses, respectively:

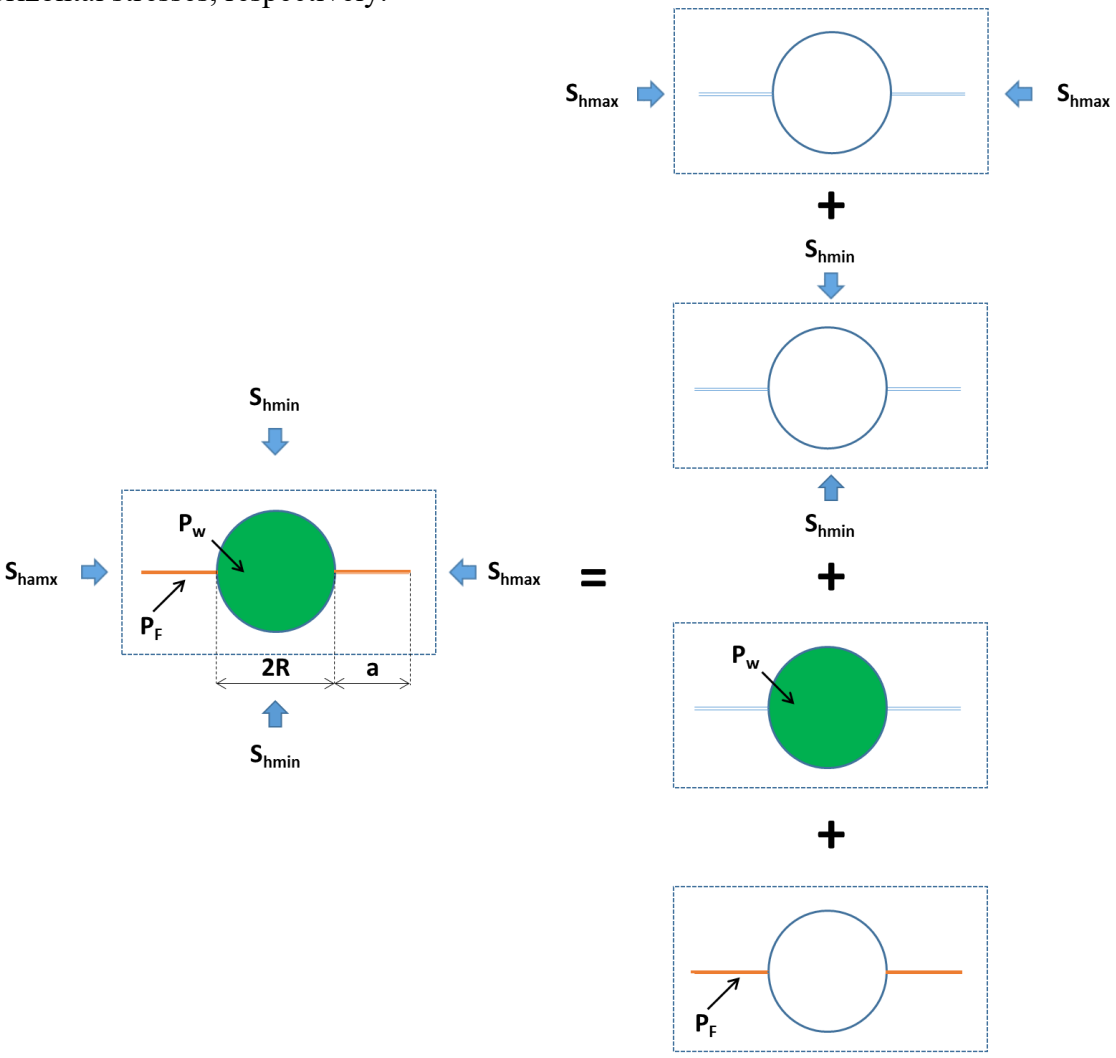

Figure 20 – Derivation of Rummel's model for FIP. The principle of superposition is employed to incorporate the effects of the S_{hmax}, the S_{hmin}, the wellbore pressure (P_W), and the pressure within the pre-existing fractures (P_F).

$$f(b) = -2\left[\frac{b^2 - 1}{\pi b^7}\right]^{\frac{1}{2}} \quad \text{(Eq. 8)}$$

$$g(b) = [\pi b]^{\frac{1}{2}}\left[1 - \frac{2}{\pi}\sin^{-1}\frac{1}{b}\right] + 2[b^2 + 1]\left[\frac{b^2 - 1}{\pi b^7}\right]^{\frac{1}{2}} \quad \text{(Eq. 9)}$$

Table 10 presents the input parameters for Rummel's model for notched boreholes. The length of pre-existing fractures for notched sample ($a_{Notched}$) is equal to the notch length (0.25 inch). Table 11 and Table 12 compare the FIP values as predicted by Rummel's with measured values for fully invaded and un-invaded pre-existing fracture cases using notched samples. For both cases, the theoretical results were compared with the measured values from the experiments. Table 11 indicates that the fully invaded pre-existing fracture assumption underestimates the FIP. This may be because the assumption of a fully invaded fracture ignores the effect of mud filter cake and rock permeability, which prevent pressure build-up in pre-existing fractures. In contrast, the un-invaded pre-existing fracture assumption provides a relatively accurate estimation of the FIP for both rock types (as indicated in small error values in Table 12). The observed discrepancies (errors) between the measured and theoretical FIPs are mainly due to variation in the sample fracture toughness and the notching dimension.

K_{IC} (psi√inch)		R (inch)	$a_{Notched}$ (inch)
Berea Sandstone	Castlegate Sandstone		
237	291	0.25	0.25

Table 10 – Input parameters used in Rummel's model for notched samples

Table 13 shows the FIP analysis using Rummel's model for un-notched Berea sandstone samples. Given the results of the validity of un-invaded pre-existing fracture assumption for notched borehole sample, the Rummel's model was applied using the same assumption for un-notched samples. Unlike notched samples, in which the length of the pre-existing fractures is equal to the notching depth, the length of pre-existing fractures in un-notched samples need to be determined by studying the near-borehole micro-fractures. In principle, the length of these pre-existing fractures may be determined using high

resolution CAT scan imaging of the borehole. However, given the relatively large diameter of the tested samples and small size of pre-existing fractures, the existing CAT scan imaging devices are not capable of producing such high resolution images. In this study, we determined the size of pre-existing fractures through an indirect method for Berea sandstone samples. First, the length of pre-existing fractures was back-calculated using the measured FIP at 100 psi confining pressure. Next, the calculated length of pre-existing fractures was verified against the theoretical value of FIP at 10 psi confining pressure. Acceptable agreement was observed between the measured and theoretical FIP of Berea sandstone at 10 and 100 psi confining pressures.

Sample	Confining Pressure (psi)	Theoretical FIP (psi)	Measured FIP (psi)	Error (%)
Berea Sandstone	10	207	729	71.6
	100	296	1145	74.2
Castlegate Sandstone	100	341	1136	70.0

Table 11 – Comparison between the measured and theoretical FIPs for notched samples, using Rummel's model with fully invaded pre-existing fractures assumption

Sample	Confining Pressure (psi)	Theoretical FIP (psi)	Measured FIP (psi)	Error (%)
Berea Sandstone	10	683	729	6.3
	100	975	1145	14.9
Castlegate Sandstone	100	1123	1136	1.1

Table 12 – Comparison between the measured and theoretical FIP for notched boreholes, using Rummel's model with un-invaded pre-existing fracture assumption

Sample	$a_{Un\text{-}Notched}$ (inch)	Confining Pressure (psi)	Theoretical FIP (psi)	Measured FIP (psi)	Error (%)
Berea Sandstone	0.01	10	1440	1594	9.7
		100	1608	1624	1.0

Table 13 – Comparison between the measured and theoretical FIP for un-notched Berea sandstone samples, using Rummel's model with un-invaded pre-existing fracture assumption

5.4 FPP Analysis: Comparison between the UT MudFrac and the DEA 13 Experiments

In this section, the FPP values obtained using the UT-MudFrac equipment are compared with the results of the DEA 13 investigation. As discussed in Section 2.2.1, the DEA 13 experiments were conducted using larger sample sizes and borehole diameters, and under polyaxial stress conditions. Thus, a comparison between the DEA 13 and the UT MudFrac experiments may be beneficial to investigate the effect of borehole diameter, sample size, and the magnitude of S_{hmin} and S_{hmax}.

5.4.1 OBM WITHOUT LCM

Fracturing experiments were conducted using 12 ppg SBM without LCM with UT MudFrac system. Fracture propagation injections were conducted at 200, 300, 400, and 500 psi confining pressures and the average FPP values were determined. Next, the obtained average FPP values were compared with the results of the DEA 13 experiments. We analyzed all the fracturing experiments which were conducted in the DEA 13 experiments (Phase I and II) using OBM without LCM. As noted in Section 2.2.1, four oil-based fluid systems were tested in the DEA 13 experiments: 10 ppg DOBM, 16 ppg DOBM, 10 ppg MOBM, and 16 ppg MOBM. For the present study, the results of oil-based

fluids with similar rheological properties to the present SBM were collected. These fluids include 10 ppg DOBM, and 10 ppg and 16 ppg MOBM. The results of highly viscous 16 ppg DOBM were discarded, since mud rheology may affect the average FPP measurements. Subsequently, using the method explained in Section 4.3, the average FPP values were extracted by digitizing the injection curves. A total number of 46 average FPP data points were obtained for base DOBM and MOBM. The extracted FPP values were then categorized based on the fluid system, borehole diameter, the S_{hmin} value, and the S_{hmax} value.

Experimental Study	Test – Injection	Fluid System	Average FPP (psi)
UT MudFrac Experiment (Isostatic Stress Conditions): $S_{hmin} = S_{hmax} = S_v = 300$ psi Borehole diameter = 0.5 inch	–	12 ppg SBM	1265
The DEA 13 Investigation (Polyaxial Stress Conditions): $S_{hmin} = 300$ psi $S_{hmax} = 2500$ psi $S_v = 3000$ psi Borehole diameter = 1.5 inch	7 – 4	16 ppg MOBM	1119
	13 – 4	16 ppg MOBM	1284
	16 – 4	10 ppg MOBM	1295
	17 – 4	10 ppg DOBM	1154
	21 – 4	10 ppg MOBM	1169
	22 – 4	10 ppg DOBM	1241
	Arithmetic Mean of the Measured Average FPP values		1210

Table 14 – Stable FPP comparison between the UT MudFrac and the DEA 13 experimental results at 300 psi S_{hmin}

In order to investigate the effect of the horizontal stress anisotropy and borehole size on the stable FPP, we compare the average FPP at 300 psi S_{hmin} from the UT MudFrac and DEA 13 experiments in Table 14. It should be noted that since both UT MudFrac and

DEA 13 experiments were conducted at atmospheric pore pressure, the applied stresses (confining pressure in the UT MudFrac experiments and vertical stress (S_v), S_{hmax}, S_{hmin} in the DEA 13 experiments) also represent the effective principal stresses. Although different borehole sizes were used in the UT MudFrac (0.5 inch) and the DEA 13 (1.5 inch) experiments, an acceptable agreement was observed in the obtained average FPP. As explained in Section 2.1, this is because the stable FPP relates to propagation of a relatively long DIF which is mainly independent of the stress concentration around the borehole, and thus does not depend on the S_{hmax} or the borehole radius. Furthermore, the results of the DEA 13 experiments, which were obtained under a very intense horizontal stress anisotropy (S_{hmax} / S_{hmin} = 8.33), are comparable with those of the UT MudFrac experiments with isostatic stress condition. This clearly indicates that the value of the stable FPP is solely affected by the magnitude of the horizontal stress applied perpendicular to the fracture plane (i.e., the S_{hmin} value) and does not depend on other principal stresses (the S_{hmax} and the S_v).

In order to further investigate the relationship between the average FPP and the S_{hmin}, the obtained stable FPP values from the UT MudFrac and the DEA 13 experiments using various S_{hmin} values are plotted in Figure 21. The average FPP values using the UT MudFrac system are plotted at 200, 300, 400, and 500 psi S_{hmin} (i.e., the confining pressures) using SBM without LCM. Also, the average FPP data points for both tested borehole sizes in the DEA 13 investigation (1.5 and 4 inches) are plotted against the S_{hmin}. Next, a regression analysis was performed on the entire data set (using the results of the UT MudFrac and DEA 13 experiments) and the coefficient of determination (R^2 factor) was calculated. Considering the significant variation of the tested borehole sizes, drilling fluid systems, and the large number of tested rock samples, the obtained R^2 factor (0.86) suggests that there exists a linear relationship between the average FPP and the S_{hmin} values.

In addition, another regression analysis was performed using the results of the UT MudFrac data solely. The obtained trend line from the UT MudFrac data is in excellent agreement with the trend line obtained from the entire data set. These results show that the propagation injections conducted using a relatively small borehole size (0.5 inch) under low confining pressures (up to 500 psi) can be used to predict the average FPP for a full-scale diameter borehole (4 inches diameter) at large in-situ stresses (2500 psi S_{hmin}). In fact, for the tested fluid system, the UT MudFrac results may be used to predict the average FPP within a reasonable accuracy for large-scale fracturing experiments, and possibly field applications.

In Figure 21, there exists a significant variation between the average FPP measured in the DEA 13 investigation at 1800 psi S_{hmin}. As explained before, this variation is mainly due to differences in the properties of the tested drilling fluid systems and rock sample. In order to better understand the observed variation, we re-assessed the results of 31 different fracture propagation injections conducted in the DEA 13 investigation using 1800 psi S_{hmin}. In Figure 22, the normal probability plot of all measured average FPP is shown. This plot clearly indicates that measured average FPP has a normal distribution. In addition, the mean value and standard deviation of the average FPP (measured at 1800 psi S_{hmin} in the DEA 13 investigation) are reported in Table 15. Next, the average FPP at 1800 psi S_{hmin} was calculated using the trend line obtained from the UT MudFrac data (shown with solid blue line in Figure 21) and compared with the mean value of the average FPP in the DEA 13 experiments. There exists a clear agreement between the measured average FPP in the DEA 13 experiments and the predicted average FPP using the UT MudFrac trend line. The results of our analysis in this section confirm that the observed variation in the average FPP at 1800 psi S_{hmin} are mainly due to differences between the sample properties, drilling fluid system, and minor experimental error. Moreover, it seems that the average FPP obtained

from the UT MudFrac trend line presents a reliable estimate of the mean value of the average FPP measured in the DEA 13 investigation at 1800 psi S_{hmin}.

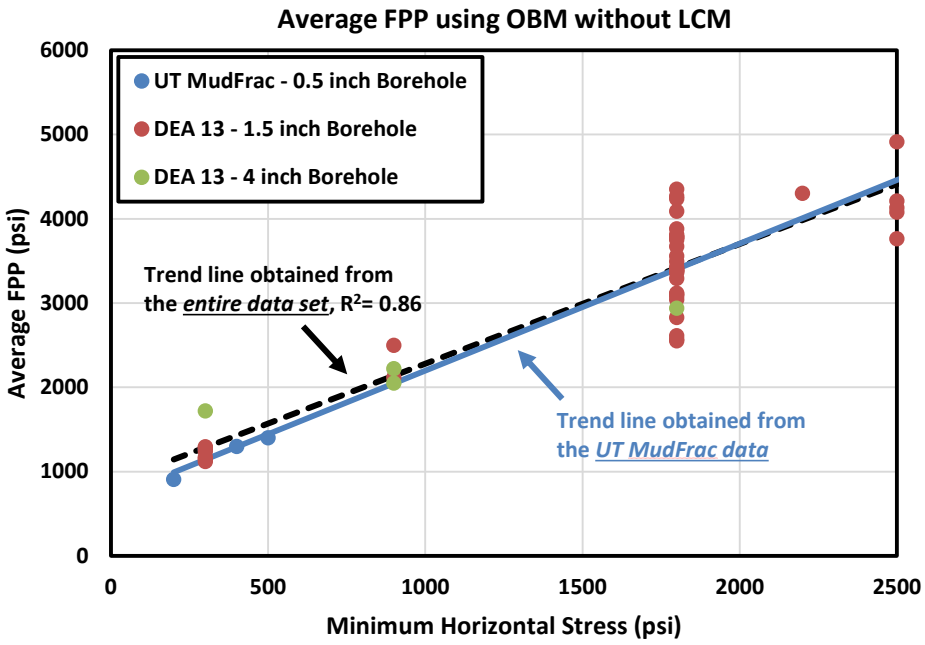

Figure 21 – Comparison between the DEA 13 and the UT MudFrac experiments using OBM without LCM. The UT MudFrac experiments were conducted using SBM without LCM. The DEA 13 experiments were conducted using either MOBM or DOBM without LCM. An average FPP trend line was obtained using the entire data set (shown with a black dashed line). Also, another trend line was obtained using the UT MudFrac experimental data solely (shown with a solid blue line). Overall, it seems that the average FPP changes linearly with the S_{hmin}. Moreover, the results from the UT MudFrac and the DEA 13 experiments closely match.

Appendix VI presents the supporting information for this section in Figure A6 and Table A1. Figure A6 illustrates the fracture propagation injection curves for SBM without LCM, using the UT MudFrac system. Table A1 lists all the average FPP values data points for the base OBMs, extracted from the DEA 13 experiments. The test number, injection

number, fluid system, the applied S_{hmin}, and the borehole size are shown for each average FPP.

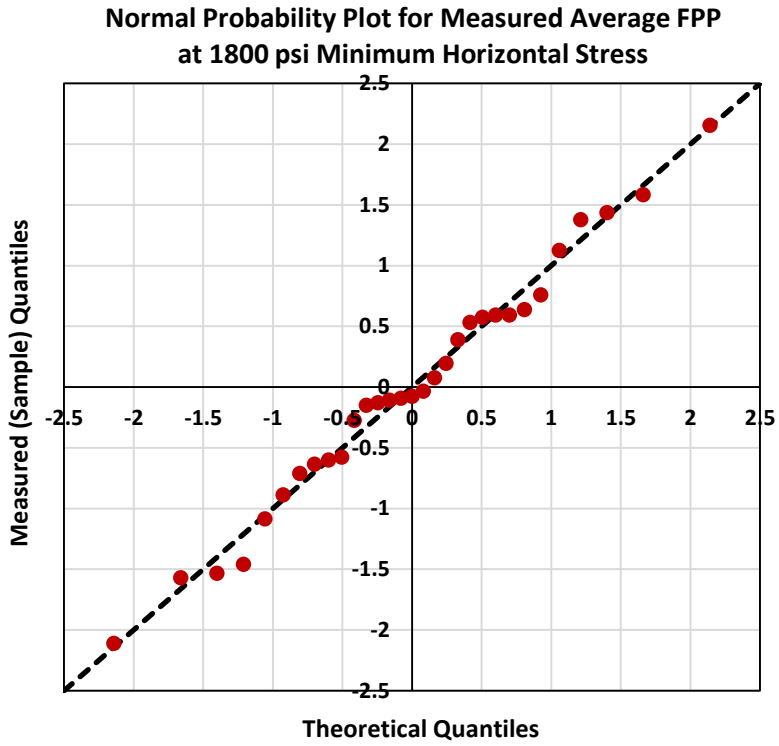

Figure 22 – The normal probability plot for the average FPP measured at the DEA 13 experiments using 1800 psi S_{hmin}. The obtained normal probability plot indicates that the measured average FPP has a normal distribution.

The DEA 13 investigation		The UT MudFrac experiments	
Measured Average FPP		Predicted Average FPP (psi)	3404
Mean Value (psi)	3448		
Standard Deviation (psi)	571		

Table 15 – Comparison between the measured average FPP at the DEA 13 investigation and the predicted average FPP values using the UT MudFrac trend line at 1800 psi S_{hmin}

5.4.2 OBM WITH GRAPHITE / CALCIUM CARBONATE-BASED LCM

In this section, the results of the UT MudFrac experiments using SBM with 20 ppb of the fine graphite-based LCM (as discussed in Section 5.1.1) are analyzed. Fracture propagation injections were conducted at 100, 200, 300, 400, and 500 psi confining pressures and the average FPP values were calculated. The results were then compared with the DEA 13 experiments, which used MOBM with a calcium carbonate-based LCM. This LCM has a PSD similar to the fine graphite-based LCM tested in this study (see Section 5.1.1). Table 16 shows the mass division diameters (D_{10}, D_{50}, D_{90}) of the fine graphite-based LCM and the calcium carbonate-based LCM. As shown in Section 5.1.2, the WBS benefits of an LCM blend are primarily determined by its PSD, not by the type of the material used. Thus, similar strengthening benefits are expected using these two LCM blends. The DEA 13 experiments were conducted using either 40 or 80 ppb of LCM concentration, whereas the UT MudFrac experiments were conducted using 20 ppb LCM concentration. As discussed in Section 5.1.3, 20 ppb is the optimum LCM concentration for Berea sandstone. This means that similar strengthening benefits are expected in concentration equal to - or above - 20 ppb. This then allows us to directly compare our results obtained at 20 ppb LCM with DEA 13 results obtained at 40 ppb or 80 ppb LCM.

Figure 23 shows the average FPP values obtained from the UT MudFrac and the DEA 13 experiments. Also, a regression analysis was conducted using the entire data set to determine the trend line and the R^2 factor. Similar to Section 5.4.1, another regression analysis was conducted using solely the UT MudFrac experimental results. Several conclusions can be obtained by comparing the average FPP measured in the DEA 13 and the UT MudFrac experiments. Similar to OBM without LCM, the average FPP for OBM with LCM changes linearly with the S_{hmin}. In fact, compared to the base fluids, the obtained stable FPP using the LCM-laden fluid shows even a higher R^2 factor. This is because when

using LCM, the effect of seal re-opening in the fracture length becomes even more dominant. In contrast, the effects of the borehole size, stress concentration around the borehole, and variation in the sample properties become even less important. Furthermore, the obtained trend line from the UT MudFrac experiments is in excellent agreement with the trend line from the entire data set. This clearly confirms that the average FPP may be extrapolated across a large range of the S_{hmin} and the borehole size. Moreover, the obtained results in this section support all of the findings of this dissertation regarding the effects of LCM PSD, type, and concentration (as discussed in Sections 5.1.1, 5.1.2, and 5.1.3). These results clearly prove that the average FPP is determined by the PSD of the LCM, not the type used, and that 20 ppb is the optimum concentration threshold for Berea sandstone.

Appendix VII presents the supporting information for this section, in Figure A7 and Table A2. Figure A7 illustrates the fracture propagation injection curves, which were used to determine the average FPP values using the UT MudFrac system. Table A2 lists all the average FPP values using the calcium carbonate-based LCM, extracted from the DEA 13 experiments. The DEA 13 test number, injection number, LCM concentration, S_{hmin}, and borehole size are shown for each average FPP value.

LCM Type	D_{10} (μm)	D_{50} (μm)	D_{90} (μm)
Fine Graphite-Based	26	91	325
Calcium Carbonate-Based	60	150	300

Table 16 – Mass division diameters for graphite-based and calcium carbonate-based LCMs

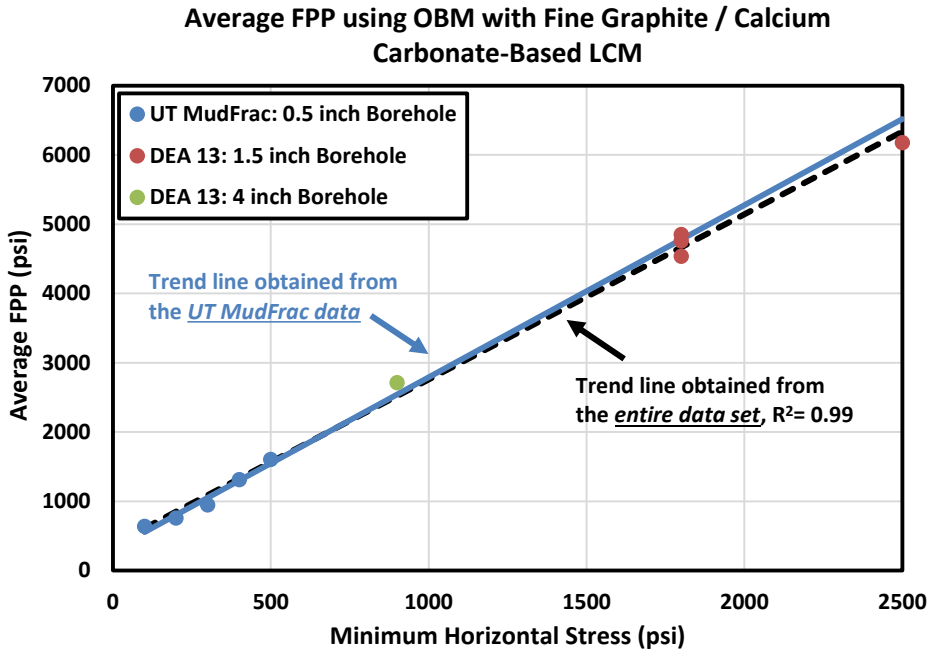

Figure 23 – Comparison between the DEA 13 and the UT MudFrac experiments using fine graphite / calcium carbonate-based LCM blends. The UT MudFrac experiments were conducted using SBM with the fine graphite-based LCM. The DEA 13 experiments were conducted using MOBM with a calcium carbonate-based LCM. An average FPP trend line was obtained using the entire data set (shown with a black dashed line). Also, another trend line was obtained using the UT MudFrac experimental data solely (shown with a solid blue line). Excellent agreement was observed between the UT MudFrac and the DEA 13 results.

5.4.3 OBM WITH GILSONITE-BASED LCM

In this section, the average FPP values obtained from the UT MudFrac and the DEA 13 experiments using Gilsonite-based LCM are compared. Fracture propagation injections were conducted using SBM with 20 ppb of Gilsonite-based LCM at 200, 300, 400, and 500 psi confining pressures and the average FPP values were calculated. The DEA 13 experiments (Phase 2) were conducted using 16 ppg MOBM with either 40 or 80 ppb

Gilsonite concentrations. Similar to Sections 5.4.1 and 5.4.2, the average FPP values using Gilsonite-based LCM were extracted and categorized.

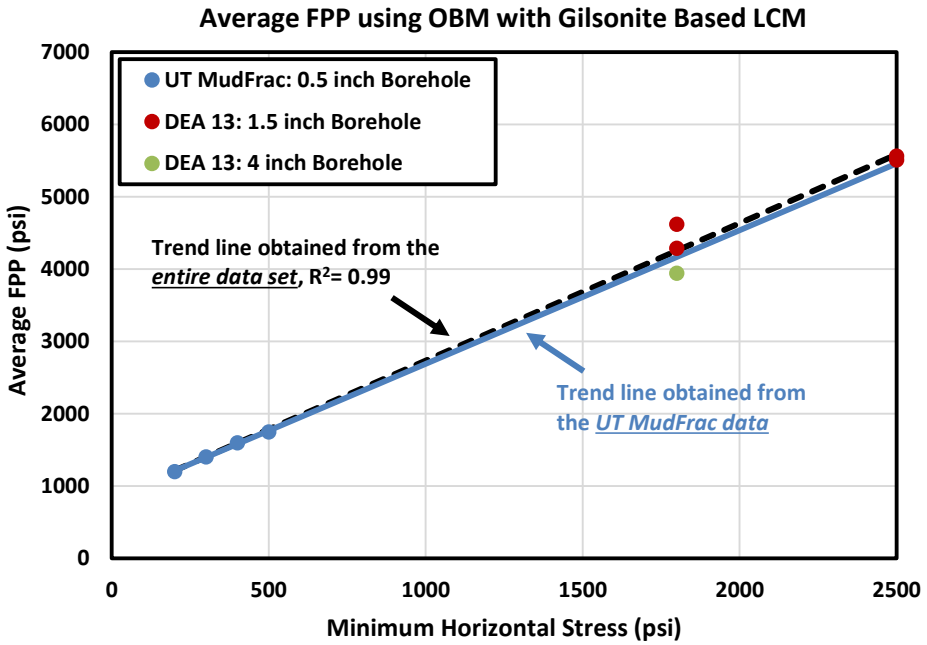

Figure 24 – Comparison between the DEA 13 and the UT MudFrac experiments using Gilsonite-based LCM. The UT MudFrac experiments were conducted using SBM with Gilsonite-based LCM. The DEA 13 experiments were conducted using MOBM with Gilsonite-based LCM. An average FPP trend line was obtained using the entire data set (shown with a black dashed line). Also, another trend line was obtained using the UT MudFrac experimental data solely (shown with a solid blue line). Excellent agreement was observed between the UT MudFrac and the DEA 13 results.

Figure 24 shows the average FPP against the S_{hmin} for Gilsonite-based LCM for both the UT MudFrac and the DEA 13 experiments. Next, average FPP trend line and R^2 coefficient were obtained using the entire data set and the UT MudFrac experiments. Similar to Sections 5.4.1 and 5.4.2, excellent agreement is observed between the UT MudFrac and the DEA 13 results. These results confirm all of our conclusions in sections

5.4.1 and 5.4.2 regarding the LCM concentration, the borehole size, and the linear relationship between average FPP and S_{hmin}.

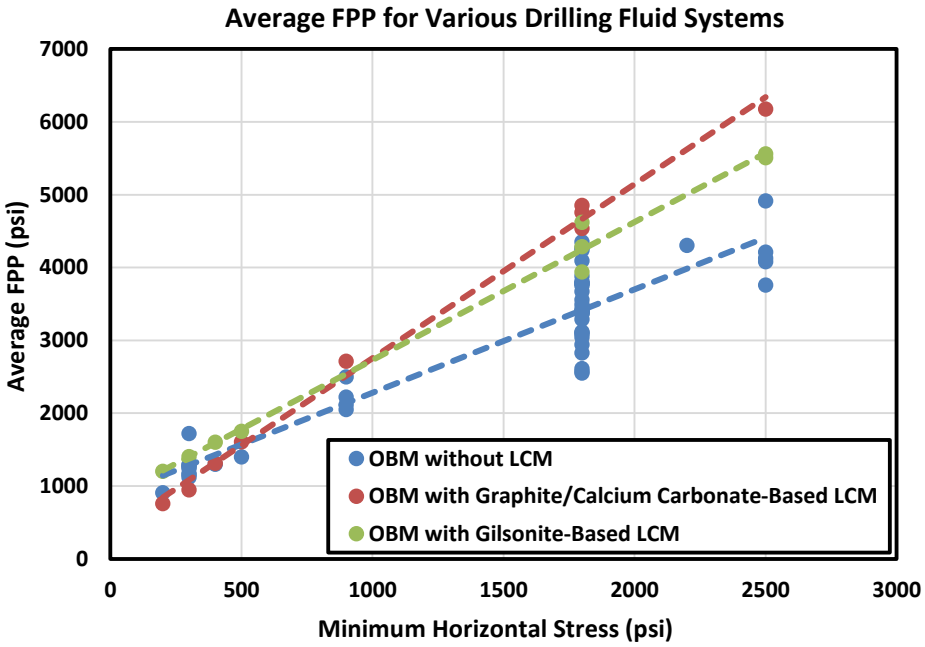

Figure 25 – Average FPP using various drilling fluid systems. Note that both LCM-laden drilling fluids have a steeper stable FPP trend line. This means strengthening effects are more pronounced at higher S_{hmin}.

In order to investigate the effect of LCM on the stable FPP trend line, the results of all stable FPP values in Sections 5.4.1 to 5.4.3 are plotted in one chart (Figure 25). In comparison with the OBM without LCM, a significant increase was observed in the slope of the trend line for OBM with LCM blends. A steeper trend line indicates a larger increase in the average FPP for an equal increment in the value of S_{hmin}. This observation suggests that strengthening effects are more pronounced at higher S_{hmin} values, since more confinement results in more effective fracture sealing. Furthermore, comparing the results of the graphite/calcium carbonate-based LCM with the Gilsonite-based LCM indicates that

optimizing the properties of the LCM blend (such as the PSD) may significantly enhance the attainable strengthening effects at higher in-situ stresses, by providing a steeper trend line.

Appendix VIII presents the supporting information for this section, in Figure A8 and Table A3. Figure A8 illustrates the fracture propagation injection curves, which were used to determine the average FPP using SBM with 20 ppb Gilsonite-based LCM. Table A3 lists the average FPP values for 16 ppg MOBM with Gilsonite-based LCM, which were extracted from the DEA 13 investigation. The corresponding test number, injection number, LCM concentration, S_{hmin}, and borehole size are shown in this table.

5.5 Design of Wellbore Strengthening Treatments

5.5.1 Post-fracturing Analysis

In this section, post-fracturing analysis techniques such as CAT scan and petrographic imaging are employed to study the fractured samples. An in-depth investigation of the fracture surface and formed seals is presented. Next, the results of the post-fracturing analyses are used to evaluate the existing theoretical models as well as the design guidelines for WBS applications. A novel design method to determine the optimum PSD is introduced.

5.5.1.1 CAT Scan Imaging of Fractured Samples

CAT scan imaging was used as a non-destructive technique to analyze the geometry of induced fractures. The CAT scan images were obtained using a 3D X-ray imaging system with an X-ray source voltage of 40 to 150 kV, and a pixel size ranging from 7 to 0.3 μm. Figure 26a shows a fractured Berea sandstone sample in which the created fracture propagated axially along the length of the sample. Since no horizontal stress anisotropy

was applied, the fracture direction was determined by material strength anisotropy and/or the orientation of pre-existing fractures. To study the deformation of the borehole due to formation of the DIF, a Berea sandstone sample was scanned before and after fracturing experiment (tested using 12 ppg SBM loaded with 30 ppb of medium graphite LCM). Figure 26b shows a CAT scan image of the borehole cross section at sample mid-length prior to fracturing experiment. The image shows a relatively smooth 1/2 inch diameter (12,700 μm) borehole. Figure 26c shows the borehole cross section of the same sample after the experiment. Two fracture wings emanated from the borehole, approximately 160 degrees apart. The width of the created fractures was measured in the vicinity of the borehole. As marked in Figure 26c, the created fractures have a relatively large width at the borehole face (approximately 1,800 in the right fracture wing and 3,000 microns in the left fracture wing). The fracture width decreases significantly as the distance from the borehole face increases (from a width of 1,800 down to 1,350 microns in the right fracture wing and from width of 3,000 down to 1,600 microns in the left fracture wing, at approximately 0.4 inch (10,000 μm) radial distance from the borehole face). For further analysis of the fracture geometry along sample diameter, another CAT scan image was taken from the entire cross section of the fractured sample (Figure 26d). The image shows that the fracture width decreases further as the distance from the borehole face increases. However, it was observed that after a certain distance (approximately 0.8 inch (20,000 μm) from the borehole face), fracture width remains relatively constant regardless of the distance from the borehole, at 700 microns in the left fracture wing and 600 microns in the right fracture wing for the image in Figure 26d. In addition to the main fracture wings a shorter fracture was also detected with a 570 microns width.

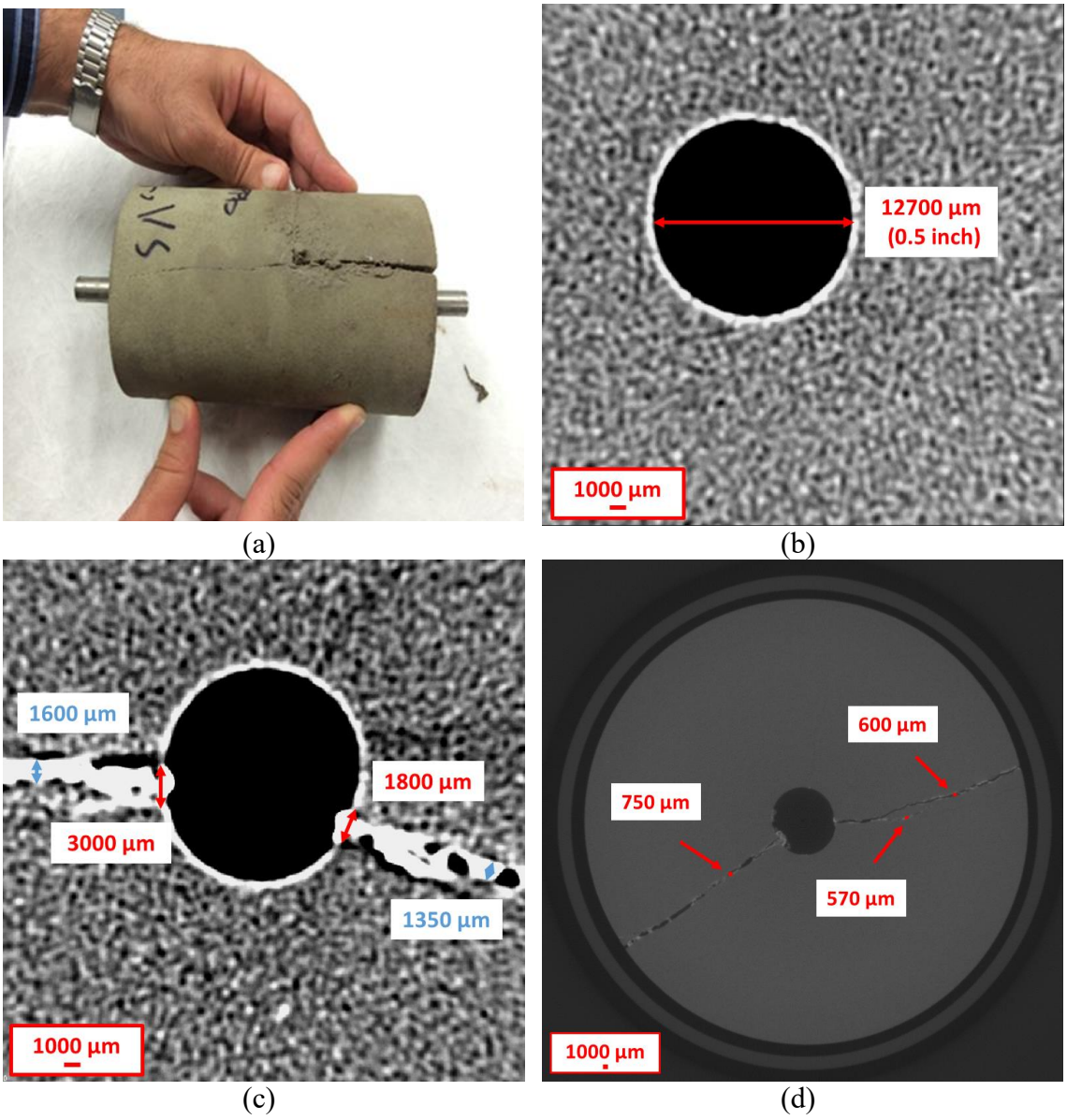

Figure 26 – Post-fracturing analysis of the fractured sample: (a) the fractured sample picture; (b) borehole CAT scan imaging of the intact (un-notched) sample prior to testing; (c) borehole CAT scan imaging of the fractured sample; (d) full cross section CAT scan imaging of the fractured sample.

It should be noted that in this study we are only presenting the images obtained from the cross section of sample at its mid height. However, it seems that the geometry of the induced fractures does not change significantly along the length of the sample. In fact,

we observed similar fracture widths in CAT scan images obtained at various heights across the sample. The measured fracture sizes were obtained from a two dimensional analysis of the sample cross section. Thus, these measured fracture sizes presents the fracture width, not the aperture. This is because the true fracture aperture is orthogonal to the fracture mid-plane and thus it may be different from the fracture width based on the fracture orientation.

The difference between the fracture width at the borehole face and along its length has important practical implication for the design of the optimum LCM PSD for WBS purposes. As discussed in Section 2.3.2, there are two main hypotheses regarding the location of seal formations in the fractures: (1) the WSA model states that the seal forms in the close vicinity of the borehole face; (2) the FPR model states that the seal forms in close proximity to the fracture tip. Given the major difference in the fracture width at the mouth and the tip, each of these hypotheses leads to significantly different PSDs for the LCM blends. In the next section, the validity of these proposed hypotheses for seal location is examined by petrographic imaging of thin-sections, which were obtained from the fracture surface.

5.5.1.2 Petrographic Imaging of Thin-Sections

Petrographic imaging of thin-section was employed to study the fractures surface and determine the location of formed seals. Fractured samples were epoxied to preserve the geometry of the induced fractures after testing. Subsequently, two thin-sections (section A and B) were extracted from the fracture surface (i.e., in the radial direction of the cylindrical samples). Next, petrographic images were then taken from these thin-sections using plane-polarized light to delineate the rock mineralogy and the presence of LCM. These images are shown in Figure 27a-d. Figure 27a-c show the petrographic images taken from section A, with different magnification factors (5X, 10X, 20X). Figure 27d shows

section B with 5X magnification factor. Note that in all images, the borehole is located on the right-hand side, whereas the fracture tip is on the left-hand side. Also, the thin-sections shown in Figure 27 represent the small fractures formed in the vicinity of main planar fracture. Due to practical considerations, it was not possible to obtain thin-sections from the main fracture, which has an average width of approximately 600 microns.

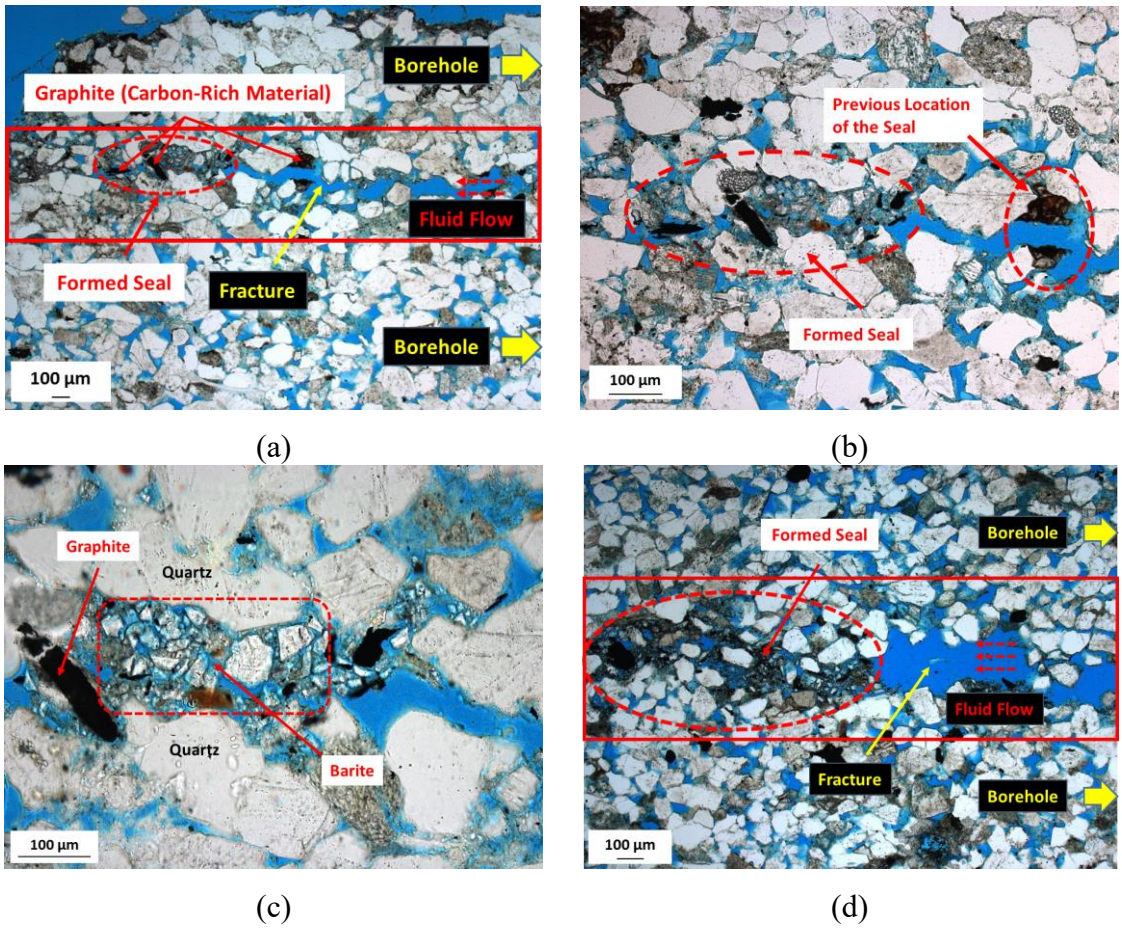

Figure 27 – Petrographic imaging of the thin-sections obtained from the fractured Berea sandstone samples: (a) section A: 5X magnification factor; (b) section A: 10X magnification factor; (c) section A: 20X magnification factor; (d) section B: 5X magnification factor.

Void spaces in the images are shown in blue. Also, clear blue regions within the rock matrix indicate the induced fractures. Berea sandstone is mostly composed of quartz and feldspar minerals, which easily can be distinguished in the images (as indicated in Figure 27c). The thin-sections were extracted from a Berea sandstone sample fractured using 12 ppg SBM loaded with 30 ppb medium graphite-based LCM blend (the same sample which is analyzed in Section 5.5.1.1). Organic (carbon-rich) LCM particles used in this sample do not reflect plane-polarized light. Therefore, the dark spots in the images indicate the presence of LCM at places where a seal was formed. To further investigate the structure of the formed seal, magnified images (Figure 27b-c) were taken from the zones with the highest concentration of carbon-rich materials. These magnified images reveal the true nature of the seal structure: in all cases, a bridge was formed by graphite-based particles which act as a "dam", while any remaining, smaller flow channels were filled in with smaller-size gray inorganic particles that were identified to be mainly composed of barium sulfate (barite). Also, several failed seals were identified along the fracture (see Figure 27b) which indicate cycles of seal formation and failure during the fracture propagation.

In summary, the conducted thin-section analysis provides several crucial insights regarding the underlying mechanics of seal formation in fractures:

(1) Formed seals are always located in close vicinity of the fracture-tip and never at the borehole face. In fact, in all of the obtained petrographic images, the highest concentration of LCM was observed close to the fracture tip and not at the fracture width at the borehole face. Such observations are in full agreement with the FPR model, which is based on the formation of pressure barriers in the vicinity of the fracture tip, and in direct contradiction with the WSA model.

(2) The presence of the compound seals made up of LCM and in-fill material behind it confirms a well-known hypothesis on fracture sealing (e.g., Dudley et al., 2000, Kageson-Loe et al., 2008). According to this hypothesis, two simultaneous mechanisms occur while sealing an induced fracture: (a) fracture bridging happens by deposition of coarser particles along the fracture width and in relatively close proximity of the fracture-tip, (b) pressure isolation of the fracture-tip happens by accumulation of finer particles behind the formed bridge/seal. The petrographic images provide experimental evidence for this hypothesis.

(3) Several zones with a high concentration of LCM and weighting material were identified (Figure 27a-b) at various locations and along the fracture length. It shows that during fracture propagation, pressure barriers will temporarily form and subsequently be compromised during fracture re-opening and propagation. This is due to repeated cycles of fracture bridging -> pressure build-up behind the bridge/seal -> breaching of the bridge followed by fracture tip propagation -> formation of a new bridge/seal, etc., as described e.g. by Morita et al. (1990 and 1996).

In order to further investigate the structure of the formed seal, an image at high magnification was taken from the thin-section shown in Figure 27d. Figure 28 shows this magnified image, with its fracture geometry and structure of the formed seal. As indicated in Figure 28:

(1) The width of the fracture near the formed seal is approximately 163 microns. This approximation for the fracture width is obtained by calculating the average of three different measurements of the fracture width in the vicinity of the formed seal in Figure 28.

(2) A bridge was formed by coarse bridging particles along the fracture width which acts similar to a dam. The size of the coarse particles is approximately 147 microns or 90 percent (≈ 147/163) of the fracture width.

(3) Fine gray particles (which are mainly composed of Barite) accumulated behind the bridge and created a low-permeability zone. These fine particles have an average size of approximately 45 microns or 30 percent (≈ 45/163) of the fracture width.

(4) In the formed seal, the concentration of fine particles is significantly higher than the coarse particles.

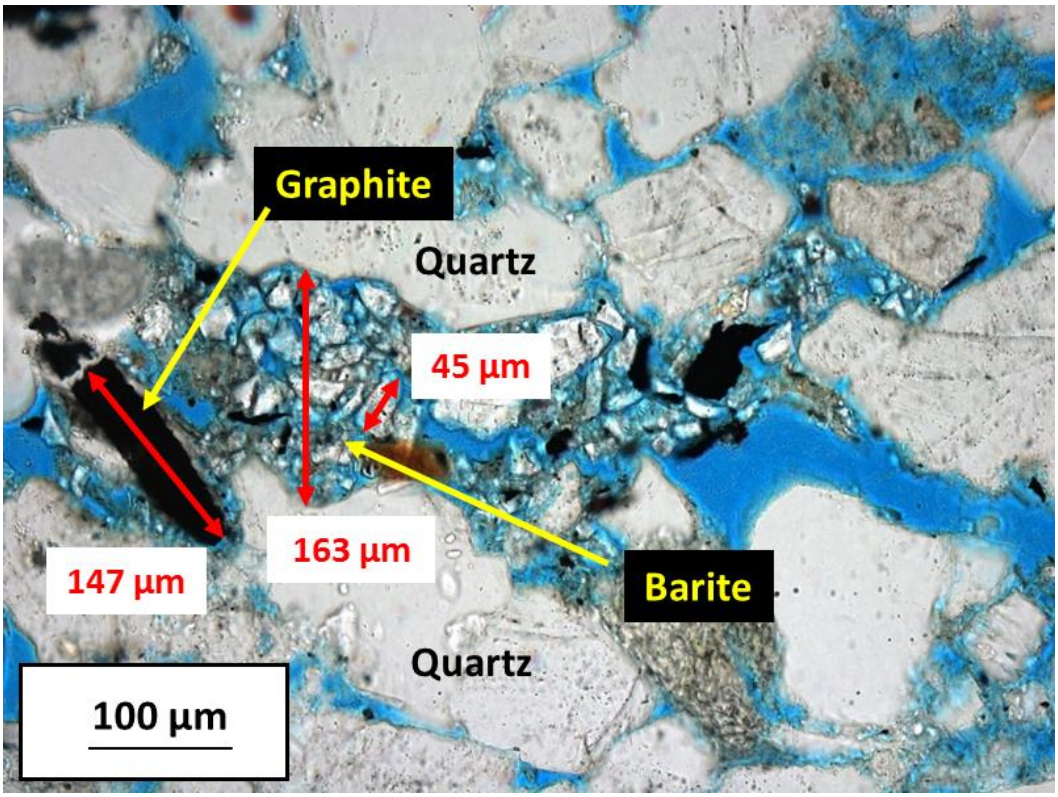

Figure 28 – Magnified petrographic image of a sealed fracture. Note that the seal is formed by a combination of coarse and fine particles. The average size of fracture width, coarse particles, and fine particles are shown in red (163, 147, and 45 microns, respectively).

Similar relationships were observed between the seal structure and the fracture size in the thin-sections obtained from other fractured samples. In fact, the thin-section analyses in this study suggest that successful fracture sealing requires sufficient concentrations of both fine and coarse particles in the LCM blend. This observation is also in full agreement with the superior strengthening benefits of the bimodal blend (medium LCM blend) over unimodal LCM blends, observed in Section 5.1.1. The results of this analysis are used later in this dissertation to introduce a novel method for designing the optimum PSD of LCM (see Section 5.5.3).

It should be noted that due to practical considerations, the presented CAT scan imaging in Section 5.5.1.1 and petrographic imaging in Section 5.5.1.2 were conducted after unloading the sample from the vessel. This means that the measured fracture width and seal dimension were obtained at zero confining pressure. However, given the relatively low applied confining pressure (up to 500 psi) and high stiffness of the rock samples (approximately 1×10^6 psi), no major variation in the size of the fracture width and seal dimension is expected during the experiment. In fact, it seems that the observed fracture geometry in Sections 5.5.1.1 and 5.5.1.2 are representative of the actual DIF geometry during our experiments.

5.5.2 Assessment of the Existing Guidelines to Design WBS Treatments

In this section, we evaluate three well-known design guidelines to determine the optimum concentration and PSD of LCM blends: the one-third rule, the Vickers criteria, and the ideal packing theory. All guidelines evaluated here propose fixed minimum concentrations of plugging particles in the drilling fluid, namely 5 percent by volume of the solids in the one-third rule (Abrams, 1977), 30 ppb in the Vickers criteria (Vickers et al., 2006), and 20 – 30 ppb in the ideal packing theory (Dick et al., 2000). This means that

these guidelines prescribe a universal optimum concentration, regardless of the formation rock type and mud density. As discussed in Section 5.1.3, our experiments show that there exists no such universal optimum which maximizes strengthening benefits for any arbitrary rock type, fluid system and density. It is clear that there exists an optimum LCM concentration which is necessary for effective WBS. However, this optimum value can significantly vary depending on the formation permeability, or the formulation and density of the drilling fluid used. For example, we showed in Section 5.1.3 that higher LCM concentrations are required for successful WBS in lower-permeability formations.

All three models require the average fracture size as an input parameter. As discussed in the previous section, there exist two distinct hypotheses for the location of seal formation (either in the vicinity of the borehole or closer to the fracture tip). We evaluated all three models using both hypotheses for the location of seal formation. Therefore, two fracture sizes were obtained from our CAT scan imaging (shown in Figure 26) and used as the input parameters:

(1) The average fracture width at the borehole face = 2400 microns (the average of 1800 and 3000 microns fracture widths, shown in near-borehole CAT scan imaging (Figure 26c)).

(2) The average fracture width along the fracture length = 640 microns (the average of 570, 600, and 750 microns fracture widths, shown in full cross section CAT scan imaging (Figure 26d)).

In the following sections (Sections 5.5.2.1 to 5.5.2.3), we evaluate each design guidelines with respect to their recommendations for the optimum PSD.

5.5.2.1 The One-Third Rule

Table 17 compares the median sizes (D_{50}) of the tested LCM blends with the average fracture width at the borehole face and along the fracture length. Two conclusions can be drawn based on the measured fracture sizes and the tested PSDs:

(1) Using the fracture width values at the borehole face requires a LCM blend with a median size of at least 800 microns (which is one-third of the average fracture width of 2400 microns). We showed in Section 5.1.1 that using the coarse graphite blend LCM (D_{50} = 373) leads to sub-optimal strengthening benefits. It is anticipated that using an LCM blend with a significantly larger median size (e.g., 800 microns) will result in even lower strengthening effects. Also, adding such coarse particles to a drilling fluid is not very practical, and can adversely affect the drilling fluid viscosity. Thus, the fracture width at the borehole face should not be used to determine the median size of the LCM blend.

(2) All three blends that yielded optimum strengthening benefits (i.e., medium graphite blend, Gilsonite 1 and 2) have median sizes close to one-third of the average fracture width along the length (640/3=213). Therefore, the one-third rule provides an acceptable estimation of the optimum median size. However, the one-third rule provides no recommendation for other related design parameters, including the PSD shape (unimodal, bimodal, etc.). As discussed in the thin-section analysis, a successful WBS treatment requires a bimodal PSD with sufficient concentrations of both fine and coarse particles. Hence, PSD curves should not be designed solely by the median size and more sophisticated design approaches are required.

LCM Blend Median Size (microns)					Average Fracture Width (microns)	
Graphite Blends			Gilsonite Blends			
Fine	Medium	Coarse	Gilsonite 1	Gilsonite 2	At the Borehole Face	Along the Fracture Length
83	217	373	157	270	2400	640

Table 17 – Comparison of the LCM blend median sizes (D_{50}) and the average fracture width

5.5.2.2 The Vickers Criteria

As discussed in Section 2.4, the Vickers criteria were developed primarily to prevent formation damage, therefore they rely on the mean pore throat size as the input parameter. For WBS applications, instead of the pore throat size, the average fracture width can be used to determine the PSD parameters. In this section, the Vickers criteria were applied to obtain the mass division diameters of the optimum PSD for two fracture widths: 640 microns (average fracture width along the length) and 2400 microns (at the borehole face). In Figure 29, the mass division diameters are plotted and compared with the optimum PSD (i.e., for medium graphite, Gilsonite 1 and 2 blends).

Similar to the one-third rule, calculating the PSD from the fracture width at the borehole (= 2400 microns) overestimates the required particle size. The obtained PSD points for 640 microns fit into the optimum range for PSD. However, similar to the one-third rule, the Vickers criteria do not incorporate the physics of seal formation in fractures, which requires a bimodal PSD for LCM blends as discussed previously.

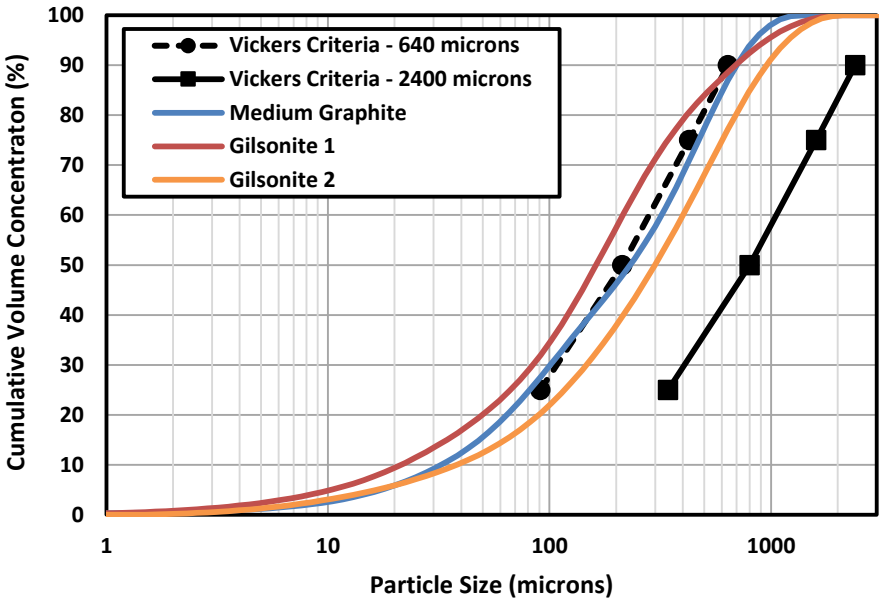

Figure 29 – Application of Vickers criteria to determine the optimum PSD. The Vickers criteria curves were generated using the fracture width along the fracture length (640 microns) and the fracture width at the borehole face (2400 microns). The generated curves were then compared with the optimum LCM PSD, tested in our experiments. Note that using the fracture width at the borehole face (i.e., 2400 microns) overestimates the required PSD. However, the curve generated using the fracture width along the length (the Vickers criteria – 640 microns) provides a reasonable estimation of the optimum PSD.

5.5.2.3 The Ideal Packing Theory

The ideal packing theory uses a power-law equation to correlate the Cumulative Volume (CV) to the particle size (D):

$$CV = 100\left[\frac{D}{D_{100}}\right]^{x} \quad \text{(Eq. 10)}$$

According to Chellappah and Aston (2012), D_{100} is given by:

$$D_{100} = \frac{100}{80} D_{mp} \quad \text{(Eq. 11)}$$

D_{mp} is the size of the maximum pore diameter (or the fracture width for WBS applications) that can be sealed by the blend. The suggested range of the exponent (x) is between 0.5 and 1. Chellappah and Aston (2012) suggested that using a linear curve ($x = 1$) provides the optimum LCM PSD. In Figure 30, several cumulative PSD curves are constructed using the power-law equation recommended by the ideal packing theory with various exponent and fracture width values:

(a) Linear PSD curve ($x = 1$) using the average fracture width at the borehole face (D – 2400 microns)

(b) Linear PSD curve ($x = 1$) using the average fracture width along the length (D – 640 microns)

(c) PSD curve with $x = \frac{1}{2}$ using the average fracture width along the length ($D^{1/2}$ – 640 microns)

(d) PSD curve with $x = \frac{2}{3}$ using the average fracture width along the length ($D^{2/3}$ – 640 microns)

Several conclusions can be drawn by comparing the PSD of the constructed design curves with the tested LCM blends:

(1) Design of the LCM blends based on the fracture width at the borehole face leads to an impractically large PSD and accordingly to sub-optimal strengthening effects.

(2) As shown in Figure 30, the D – 640 microns curve mimics the PSD of the coarse graphite blend, tested in Section 5.1.1. However, we showed that the coarse graphite blend provided sub-optimal strengthening benefits compared to the medium blend. In fact, our experiments in Section 5.1.1 indicate that changing the PSD from the coarse to the medium (the optimum blend) can enhance the strengthening benefits significantly. This finding, however, is in contradiction with

the Chellappah and Aston's (2012) recommendation for the ideal packing curve, which recommends employing a linear PSD (x = 1).

(3) The $D^{2/3}$ – and $D^{1/2}$ – 640 microns curves suggest a closer match to the optimum PSD curve (i.e., the medium graphite). However, the $D^{1/2}$ – 640 microns curve fails to mimic the optimum PSD for fine particles (<D_{50}). Overall, the $D^{2/3}$ – 640 microns curve presents the closest match to the optimum PSD.

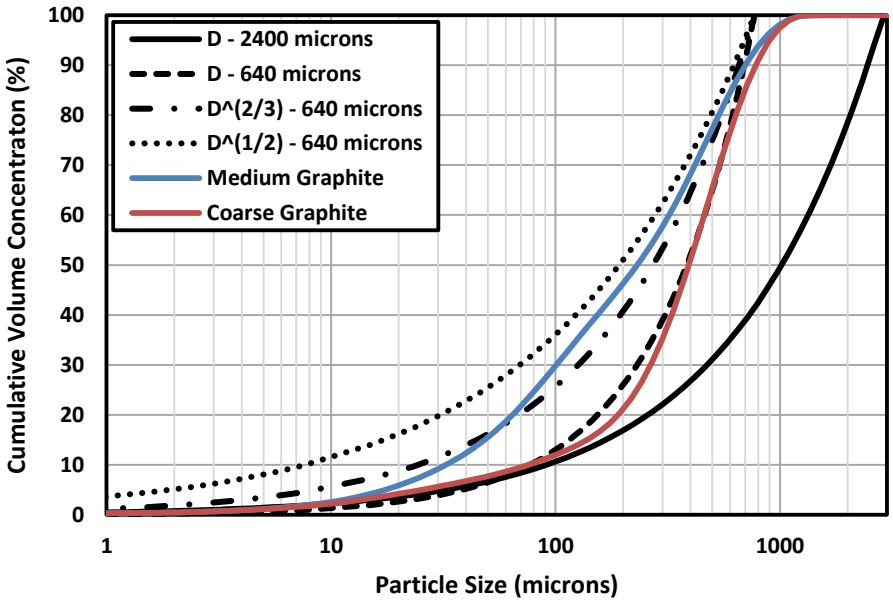

Figure 30 – Application of the ideal packing theory to determine optimum PSD. The D – 2400 microns curve overestimates the required PSD. The D – 640 microns curve provides a PSD similar to the coarse graphite blend, which shows sub-optimal strengthening benefits. Overall, $D^{2/3}$ – 640 microns curve provides the closest match to the optimum PSD (i.e., the medium graphite).

5.5.3 A Novel Design Method to Determine the Optimum PSD

The three evaluated guidelines in Section 5.5.2 are empirical methods and developed based primarily on PPA test results. Therefore, they do not realistically capture

the physics of WBS fracture sealing. Therefore, it is crucial to construct more sophisticated models for the PSD design, which take into account the underlying mechanics of the WBS phenomenon. It was shown in Section 5.5.1.2 that successful fracture sealing requires a bimodal PSD of appropriately sized fine and coarse particles. Furthermore, we determined the relationships between the fracture width and the size of these fine and coarse sealing particles by studying the formed seal in a relatively narrow fracture (163 microns width), shown in Figure 28. In this section, we use these relationships to introduce a novel design method to determine the optimum PSD for arbitrary fracture width. In order to examine this novel design method, a PSD curve is generated using the size of the average fracture width in our experiments (640 microns). The generated PSD curve is then compared with the optimum the PSD curves of the LCM blends tested in this dissertation (medium graphite, Gilsonite 1, and Gilsonite 2).

As explained earlier, the optimum PSD is bimodal and constructed by mixing fine and coarse particles. Hence, this bi-modal PSD can be generated by:

$$\mathrm{PSD}_{\mathrm{Blend}} = \omega_{\mathrm{Coarse}}\mathrm{PSD}_{\mathrm{Coarse}} + \omega_{\mathrm{Fine}}\mathrm{PSD}_{\mathrm{Fine}} \qquad \text{Eq. 12}$$

where ω_{Coarse} and ω_{Fine} are the respective concentration fractions of the coarse and fine particles in the LCM blend, and:

$$\omega_{\mathrm{Coarse}} + \omega_{\mathrm{Fine}} = 1 \qquad \text{Eq. 13}$$

To construct the PSD curve for fine and coarse particles, a probability distribution function is required. In this study, we tested various probability distributions (such as normal distribution, log-normal distribution, and Weibull distribution) and found that the PSD of the LCM particles is best approximated by using the log-normal distribution function. Moreover, this distribution has been previously used to simulate the PSD of

particulate solids (e.g., Zender, 2000). The log-normal Cumulative Distribution Function (CDF) is defined by:

$$\mathrm{CDF}_{\mathrm{M,SD}}(\mathrm{x}) = \frac{1}{2}\left[1 + \mathrm{erf}\left(\frac{\ln \mathrm{x} - \mu}{\sqrt{2}\sigma}\right)\right] \quad \text{Eq. 14}$$

where erf is the Gauss error function:

$$\mathrm{erf}(\mathrm{x}) = \frac{2}{\sqrt{\pi}}\int_0^{\mathrm{x}} \mathrm{e}^{-\mathrm{t}^2}\,\mathrm{dt} \quad \text{Eq. 15}$$

M and SD are the arithmetic mean value and standard deviation of a log-normally distributed variable (e.g., particle size) which determine the distribution's location (μ) and scale (σ) parameters:

$$\sigma = \sqrt{\ln\left(1 + \left(\frac{\mathrm{SD}}{\mathrm{M}}\right)^2\right)} \quad \text{Eq. 16}$$

$$\mu = \ln \mathrm{M} - \frac{1}{2}\sigma^2 \quad \text{Eq. 17}$$

Therefore, a PSD curve can be generated using the CDF of the log-normal distribution, which depends on the arithmetic mean value and standard deviation of the particle size:

$$\mathrm{PSD}_{\mathrm{M,SD}} = \mathrm{CDF}_{\mathrm{M,SD}}(\mathrm{D}) \quad \text{Eq. 18}$$

We used the results of the analysis in Figure 28 (Section 5.5.1.2) to determine the mean values of the fine and coarse particles. According to our analysis, the size of fine and coarse particles are approximately 30 and 90 percent of the fracture width, respectively. Thus, for a 640 microns fracture width the mean size of the fine and coarse particles will be 192 and 576 microns, respectively. Also, from the WBS experiments conducted in this dissertation, it seems that the optimum standard deviation ranges from 200 – 300 microns. Therefore, a standard deviation of 250 microns was used for both fine and coarse particles. Our analysis of the seal structure indicates that a higher concentration of fine particles is

required for effective fracture sealing. We suggest that the optimum PSD should have a concentration of 2/3 for fine particles and 1/3 for coarse particles. Table 18 presents the design parameters for fine and coarse PSD curves.

Particles	Design Parameters		
	Concentration (ω)	Mean Size (M, microns)	Standard Deviation (SD, microns)
Fine	2/3	192 ($= 0.3 \times 640$)	250
Coarse	1/3	576 ($= 0.9 \times 640$)	250

Table 18 – The design parameters used to generate the PSD curve using the log-normal distribution

The cumulative PSD design curve can then be generated by:

$$\mathrm{PSD}_{\text{Design Curve}} = \frac{1}{3}\mathrm{CDF}_{576,250} + \frac{2}{3}\mathrm{CDF}_{192,250} \qquad \text{Eq. 19}$$

In Figure 31a, the cumulative PSD curve is plotted by applying Eq. 19 and compared with the medium graphite blend. This clearly demonstrates that the design curve closely matches the cumulative PSD of the medium graphite blend. An "optimum range" for cumulative PSD was generated by the three optimum blends (the medium graphite and the Gilsonite 1 and 2 blends). As shown in Figure 31a, the design curve fits into the optimum range. We generated the PSD for the design curve by differentiating the cumulative PSD. The generated PSD is plotted in Figure 31b. The design curve has a bimodal PSD curve, similar to the tested optimum blends. Similar to Figure 31a, an optimum range was obtained from the tested optimum blends, and the constructed design curve fits into the obtained PSD optimum range.

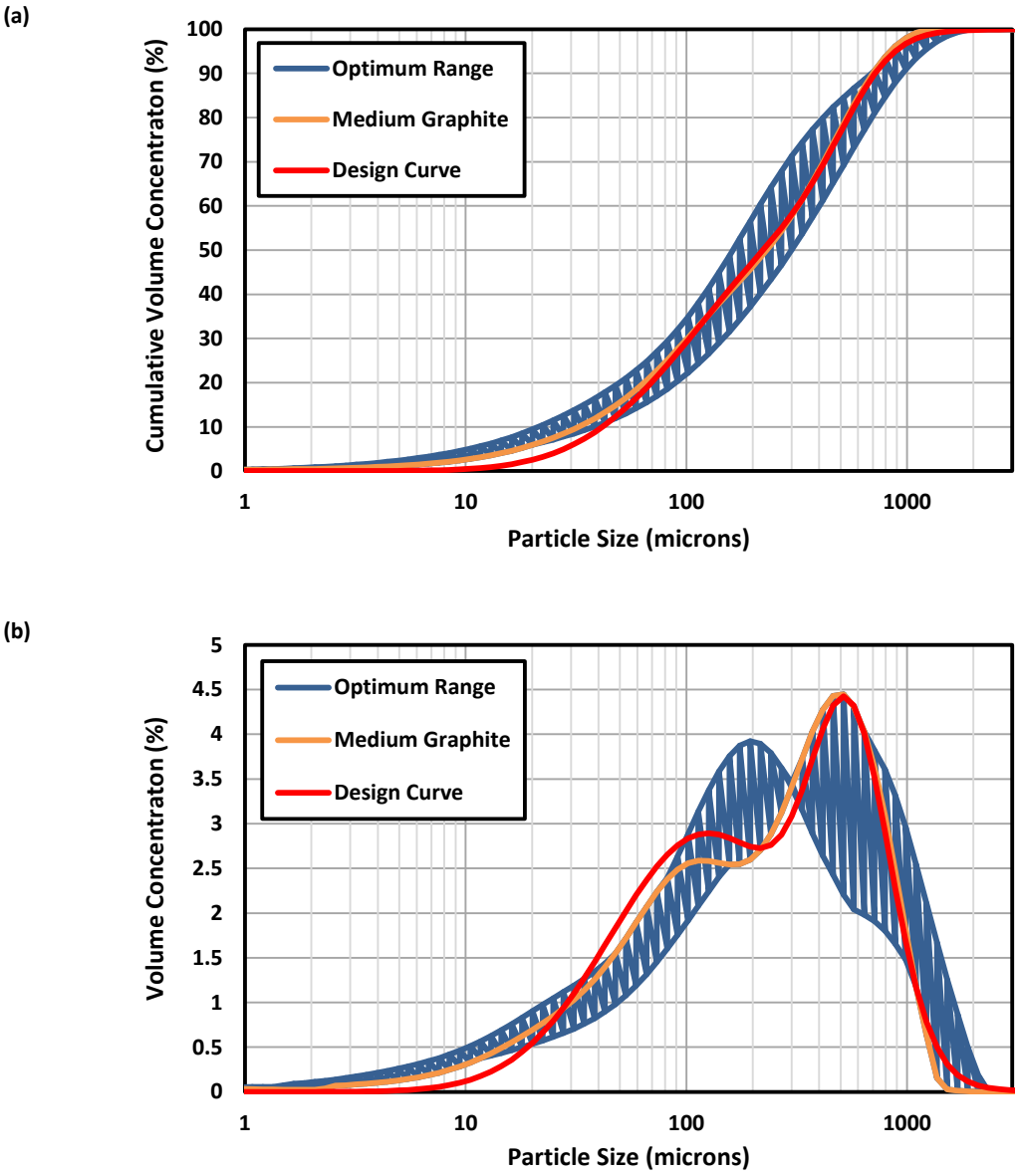

Figure 31 – Design curve constructed using the bimodal log-normal distribution. (a) Cumulative PSD of the design curve: the design curve closely matches the cumulative PSD of the medium graphite blend. Also, the generated curve fits into the optimum range for the cumulative PSD obtained from Gilsonite 1 and 2 blends. (b) The PSD curve of the design curve, as obtained by differentiating the cumulative PSD. The design curve mimics the bimodal PSD of the medium graphite blend. As before, the design curve fits into the optimum range (created by the Gilsonite blends).

The presented design method relies on the physics of the fracture sealing as observed in the WBS experiments. Furthermore, it seems that the size relationships obtained in Section 5.5.1.2 from a narrow fracture (163 microns, as shown in Figure 28) are valid in significantly wider fracture (640 microns and possibly beyond). This design method presents a general approach to determine the optimum LCM PSD for arbitrary fracture widths and PSD shapes (unimodal, bimodal, etc.). Further experiments seem necessary to examine this method for other rock types, fracture sizes, and fluid formulations. Also, it should be noted that the design method presented here is focused on the optimization of the LCM blend PSD. However, in addition to the LCM particles, the weighting agent used in the drilling fluid may significantly contribute to the attainable strengthening effects (Sanders et al., 2008). The effect of the weighting agent is typically more pronounced at higher mud density or when sealing narrow DIFs (since the weighting agents are usually finer than LCM particles). Thus, from a practical standpoint, optimizing the PSD of the used weighting agents seems necessary to maximize the strengthening effects. The finding of this dissertation regarding the mechanics of seal formation may be applied to optimize the PSD of the weighting agents.

CHAPTER SIX: SUMMARY, CONCLUSIONS AND RECOMMENDATIONS, AND FUTURE WORK

6.1 Summary

In this dissertation, a state-of-the-art experimental set-up (the UT-MudFrac system) was developed for the cost effective evaluation of WBS under realistic test conditions. The equipment offers full control over borehole mud flow and pressure, pore pressure, axial and radial confining pressures for fracturing cylindrical rock samples. Three different rock types were tested with significantly different permeability and stiffness: Berea sandstone, Castlegate sandstone, and Mancos shale. Three types of drilling fluids were used, namely KCl-based WBM, Glycol-based WBM, and SBM. Various grades of graphite-based and Gilsonite-based LCM blends were added to the drilling fluids to achieve WBS benefits. Fracturing experiments were performed to characterize the values of the FIP and the FPP and thereby characterize WBS effects. Post-fracturing analysis techniques such as CAT scan and petrographic imaging were employed to investigate the geometry of induced fractures and formed seals.

Validation experiments were performed to critically examine sample preparation and test procedure. The results of these experiment were in very good agreement with those of earlier investigations (notably the DEA 13 and GPRI studies), showing FIP to be independent of mud type, and indicating that FPP can be greatly enhanced using appropriate types and levels of LCM material. Next, parametric studies were carried out to investigate the effects of LCM PSD, LCM type, LCM concentration, injection volume, and formation stiffness on the fracturing behavior of permeable formations (i.e., Berea sandstone and Castlegate sandstone). In addition, fracturing experiments were conducted on Mancos shale samples using various drilling fluid systems to study the initiation and propagation of DIFs in impermeable formation.

The obtained FIP and FPP values were analyzed and compared with well-known theoretical and experimental studies. The value of FIP was measured using two different borehole geometries: un-notched and notched. Next, the measured FIPs were compared with theoretical models for FIP, such as Hubbert and Willis' model and Rummel's model. The variation of FPP with confining pressure was investigated. Furthermore, the measured FPP values using Berea sandstone were compared with the large-scale fracturing experiments conducted in the DEA 13 investigation to evaluate the effects of borehole diameter, sample size, minimum in-situ stress, and horizontal stress anisotropy.

The results of CAT scan and petrographic imaging were analyzed to obtain crucial insight into the geometry of the DIF and the underlying physics of fracture sealing. These results were then employed to evaluate the existing design guidelines for WBS treatments, namely the one-third rule, the Vickers criteria, and the ideal packing theory. A novel design method was introduced to determine the optimum PSD of LCM blend for WBS purposes.

6.2 Conclusions and Recommendations

- PSD appears to be of overriding importance in maximizing WBS effects and achieving elevated FPP values in permeable rocks. The type of LCM seems to be of lesser importance. This observation may explain why different parties historically have favored different WBS materials: whether one choose calcium carbonate, graphite or Gilsonite may simply be a matter of personal preference (usually inspired by prior success with a particular material or treatment) as long as the selected PSD is close to optimum. The optimum PSD is dependent on the fracture dimensions, and will therefore vary for different formation types, in-situ stresses, and borehole geometries.

- LCM blends with a bi-modal PSD distribution have a clear strengthening advantage over unimodal blends. The reason is related to the underlying mechanics of seal formation along the fractures, as indicated by petrographic imaging of the fracture surface. Analysis of the fracture surface shows that the main structure of the seal is generated by coarser bridging agents, with finer particles deposited behind these coarser solids, to reduce the permeability of the formed seal and thereby pressure-isolating the fracture tip. Thus, in order to maximize the strengthening benefits, the LCM blend should have a sufficient concentration of both coarse and fine particles with a proper size. This observation is also fully supportive of the FPR model, which states that WBS phenomenon is due to pressure isolation of the fracture tip.
- A higher concentration of LCM in the drilling fluid will generally lead to higher FPP values. However, the FPP does not significantly increase above a certain concentration threshold, which is the economic optimum concentration for field applications. Further, we found that this optimum concentration is mainly affected by the formation permeability. In fact, our experiments show that the optimum concentration value is smaller in rocks with a high permeability, which indicates that less LCM is required for successful WBS in highly permeable rocks. This is because highly permeable rocks have a faster fluid filtration rate, which facilitates solid plugging of fractures. Therefore, effective strengthening benefits can be obtained using a lower LCM concentration.
- Increasing the injection volume of an LCM-laden fluid does not result in higher FPP. The FPP value typically reaches an optimum value after a limited volume has been injected. Injecting excess fluid beyond this volume, however, may actually reduce the FPP due to enlargement of the DIF or formation of extended fracture networks which may create a severe lost circulation problem. An important implication of this

observation for field application is that WBS squeeze treatments should be delivered using lower-volume squeezes, as they are more likely to be successful in delivering meaningful WBS effects than high-volume squeezes. Moreover, no "healing" effect was observed by stopping the fluid circulation and repeating the fracture propagation injections. In general, our work shows that continuous WBS, achieved by keeping an optimum concentration of LCM with the right PSD in the mud at all times, is preferred over squeeze methods.

- When using LCMs, the obtained FPP enhancement is independent of the stiffness (Young's modulus) of the permeable rock tested. This observation clearly contradicts the WSA model for WBS, which states that strengthening is critically affected by the stiffness of the rock.
- Conventional WBS techniques based on solids plugging of fractures are not effective in impermeable formations (e.g., shale). Due to lack of fluid leak-off in these formation, the formed fractures are highly unstable and may not be sealed through solid plugging. It seems that a radically different approach is required for WBS in impermeable formations, which do not rely – or do not rely exclusively – on fracture plugging by solids.
- The experimental results indicate that elastic solutions for FIP such as Hubbert and Willis' model significantly underestimate the FIP. This is because these models, which present a simplistic approach to characterize the FIP, do not consider the effects of borehole geometry and the presence of pre-existing fractures.
- Initiation of DIFs can be more accurately characterized by models which rely on fracture mechanics theory, such as Rummel's model. Acceptable agreement was observed between the experimental and theoretical values of FIP for Berea and

Castlegate sandstone. Furthermore, our analysis indicates that the FIP values are most accurately predicted using the assumption of un-invaded pre-existing fractures.

- The conducted experiments show that fracture propagation occurs in two stages: transient and stable. During the transient stage, a sharp decline in the FPP occurs due to enlargement of the DIF near the borehole. As the fracture length grows in the radial direction, the FPP reaches a relatively constant value which we refer to as the stable FPP. It is shown that a conservative (lower-bound) estimation of the actual stable FPP may be obtained by using the designed experimental set-up and testing procedure.
- The average stable FPP changes linearly with the minimum horizontal stress, and does not depend on the maximum horizontal stress or the vertical stress. A somewhat surprising result of this study is that the small-scale UT MudFrac test results for muds with and without LCM show excellent agreement – and can be directly compared – with the results of the large scale DEA 13 experiments conducted at much higher stresses. In all cases, straightforward linear trends were observed for combined UT Mudfrac and DEA 13 datasets.
- Thin-section analysis of fractured samples shows that seals that have formed in fractures were located in the close vicinity to the fracture-tip and not at the borehole face. These observations are in contradiction with the SC model, which relies on hoop stress elevation caused by near-wellbore fracture widening and plugging. The results, however, are fully supportive of the FPR model, which indicates that WBS happens deeper within induced or natural fractures.
- Using the fracture width at the borehole face to select the size of LCM blends overestimates the required LCM particle size and results in sub-optimal strengthening effects. Thus, the fracture width at the borehole face must not be used to determine the

size of the LCM blend. Instead, the fracture width along the fracture length and closer to the tip should be used to determine the optimal PSD.

- Conventional theories for the design of plugging particles such as the one-third rule, the Vickers criteria, and the ideal packing theory may be used in a basic first approach to determine the optimum PSD for LCM blends. However, none of these theories accurately represents the physics of fracture sealing, as observed in the WBS experiments.
- A novel method was introduced to design the optimum PSD for LCM blends. This new method employs a bimodal PSD which provides appropriately sized fine and coarse particles with sufficient concentrations in the LCM blend. The design method was compared with the optimum LCM blends tested in this dissertation, and shown to closely capture the optimum PSD curve.

6.3 Future Work

In this dissertation, a methodology is developed to determine the attainable strengthening benefits of an LCM blend in drilling mud. This methodology may be applied to evaluate other LCMs that were not tested in our experiments, as well as those LCMs which may be introduced in the future. Furthermore, the designed experimental set-up may be used to study the fracturing behavior of various formation types and drilling (or fracturing) fluids.

Primary experimental studies were conducted on shale samples using various drilling fluid systems. However, given the complexity of the initiation and propagation of DIFs in impermeable formations, further experimental studies seem necessary. In order to perform successful experimental studies on shale samples, it is necessary to apply

differential (axial) stress on the sample. This is because in the absence of sufficient differential stress, shale samples typically fail in an uncontrolled manner due to lamination. In our experiments, we employed a relatively simple method to apply differential stress on shale samples using a clamping tool. This method worked acceptably for the limited number of conducted experiments in this dissertation. More sophisticated methods – such as using a triaxial load frame – seems desirable, since they provide a more effective control over the differential stress during the fracturing experiments. Due to heterogeneity of shale samples, the experimental results typically show low repeatability. To solve the repeatability problem, synthetic impermeable materials such as cement, concrete, and Johnstone (Johnston and Choi, 1986) may be used to simulate the fracturing behavior of shale samples.

As discussed in this dissertation, there exists no reliable technique for WBS in impermeable formations (e.g. shale). Our experiments indicate that conventional WBS techniques, which relies on LCM, are not effective in impermeable formations. In order to introduce an effective technique for WBS in shale other alternatives such as drilling fluids with inverted rheology (high Yield Point and high shear-thinning), silicate-based drilling fluids, or nanoparticle-based drilling fluids may be considered.

This dissertation clearly rejects the WSA approach to explain the WBS phenomenon. Instead, it shows that the FPR model is the only viable approach which properly captures the physics of WBS. Theoretical work should be focused on developing a comprehensive model for WBS using the FPR approach, which incorporates the effects of in-situ stresses, fracture geometry, drilling fluid properties, and applied LCM blends. In order to develop such a comprehensive model, it is crucial to accurately simulate the formation and failure of seals along the fracture length. Given the complexity of simulating this problem, numerical methods such as finite element analysis appear to be most suitable.

Appendices

Appendix I: Fracture Propagation Injection Curves for Berea and Castlegate Sandstone Using Various LCM PSDs

This appendix presents the supporting information for Section 5.1.1. Figure A1 illustrates the fracture propagation injection curves for SBM base fluid (without LCM), and SBM loaded with fine, medium, and coarse graphite-based LCMs. Propagation injections were conducted at 100, 200, 300, 400, and 500 psi confining pressures using Berea and Castlegate sandstone. The average FPP for each injection curve is indicated using a dashed line on each curve.

(a)

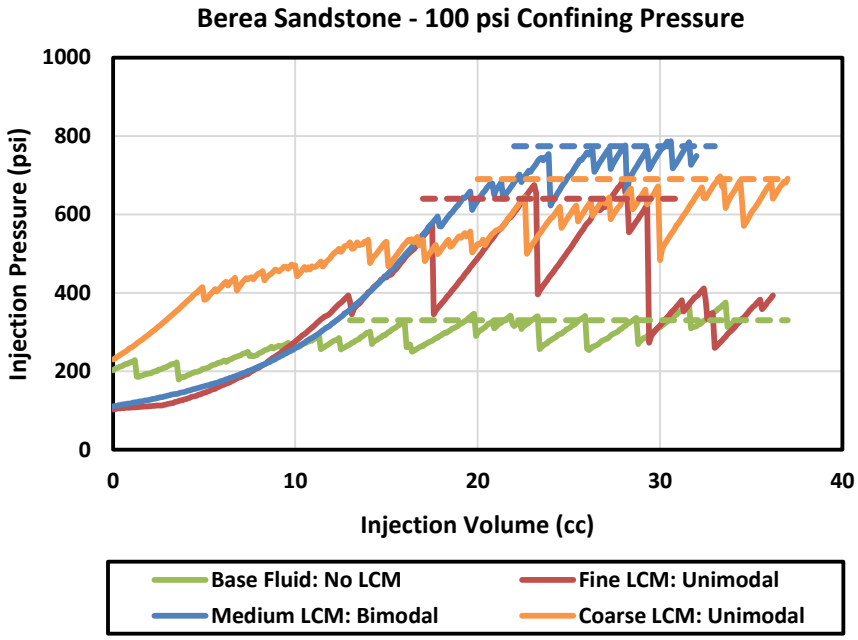

(b)

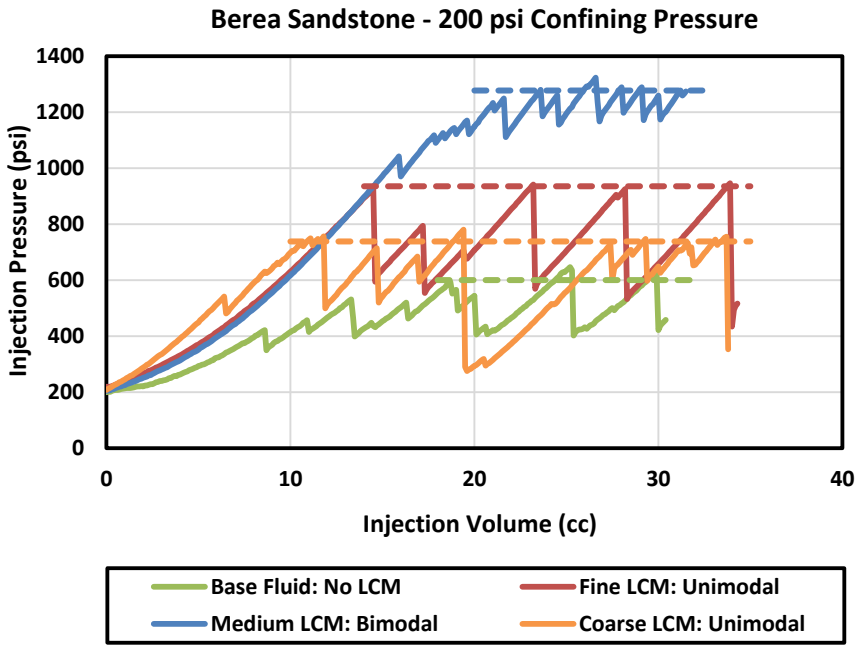
Berea Sandstone - 200 psi Confining Pressure
Injection Pressure (psi)
1400
1200
1000
800
600
400
200
0
0
10
20
30
40
Injection Volume (cc)
Base Fluid: No LCM
Fine LCM: Unimodal
Medium LCM: Bimodal
Coarse LCM: Unimodal

(c)

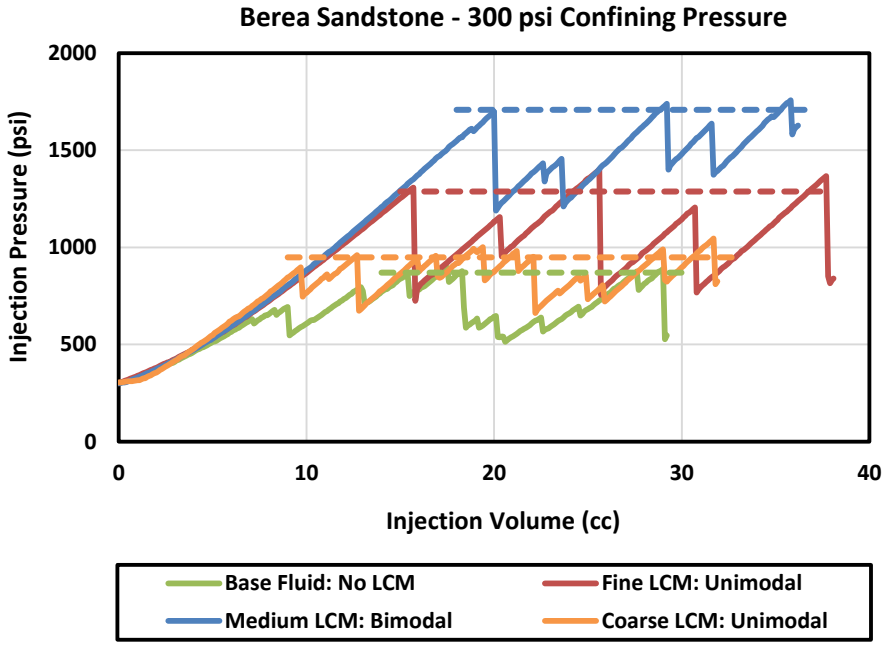
Berea Sandstone - 300 psi Confining Pressure
Injection Pressure (psi)
2000
1500
1000
500
0
0
10
20
30
40
Injection Volume (cc)
Base Fluid: No LCM
Fine LCM: Unimodal
Medium LCM: Bimodal
Coarse LCM: Unimodal

(d)

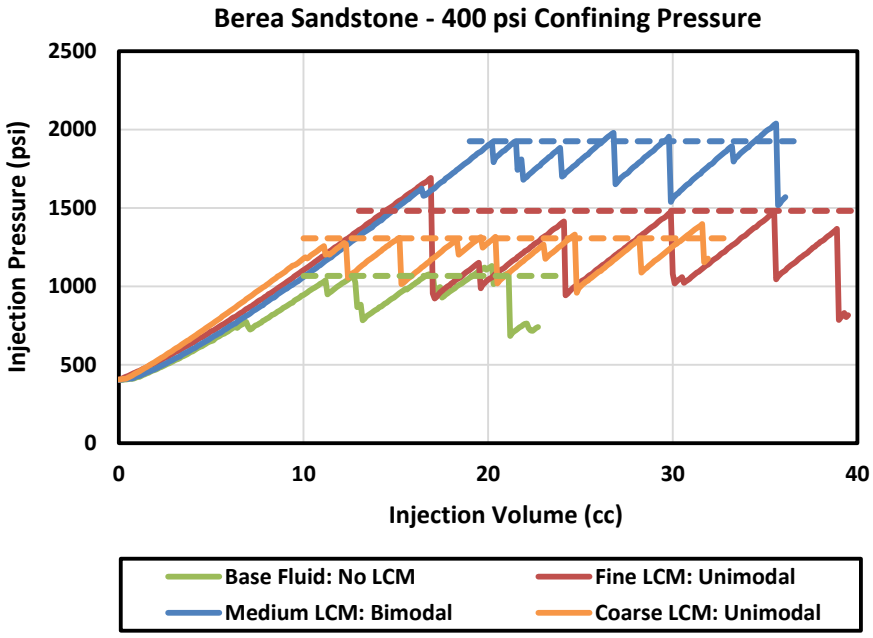
Berea Sandstone - 400 psi Confining Pressure
Injection Pressure (psi)
2500
2000
1500
1000
500
0
0
10
20
30
40
Injection Volume (cc)
Base Fluid: No LCM
Fine LCM: Unimodal
Medium LCM: Bimodal
Coarse LCM: Unimodal

(e)

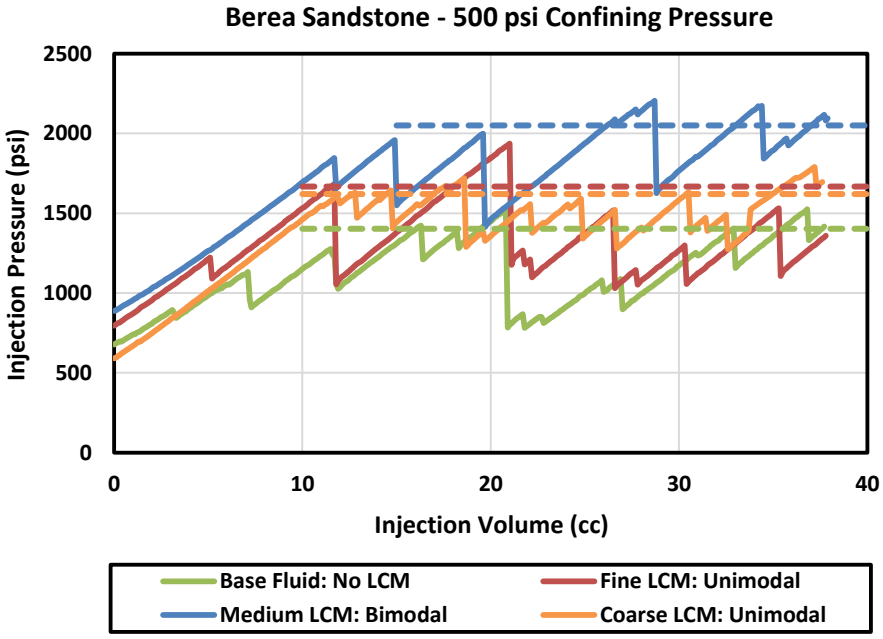
Berea Sandstone - 500 psi Confining Pressure
Injection Pressure (psi)
2500
2000
1500
1000
500
0
0
10
20
30
40
Injection Volume (cc)
Base Fluid: No LCM
Fine LCM: Unimodal
Medium LCM: Bimodal
Coarse LCM: Unimodal

(f)

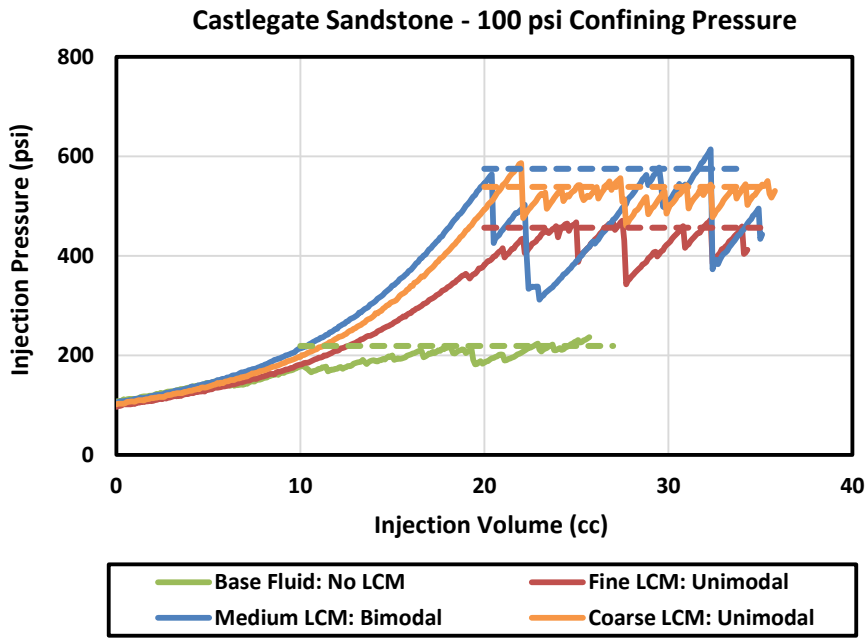
Castlegate Sandstone - 100 psi Confining Pressure
Injection Pressure (psi)
800
600
400
200
0
0
10
20
30
40
Injection Volume (cc)
Base Fluid: No LCM
Fine LCM: Unimodal
Medium LCM: Bimodal
Coarse LCM: Unimodal

(g)

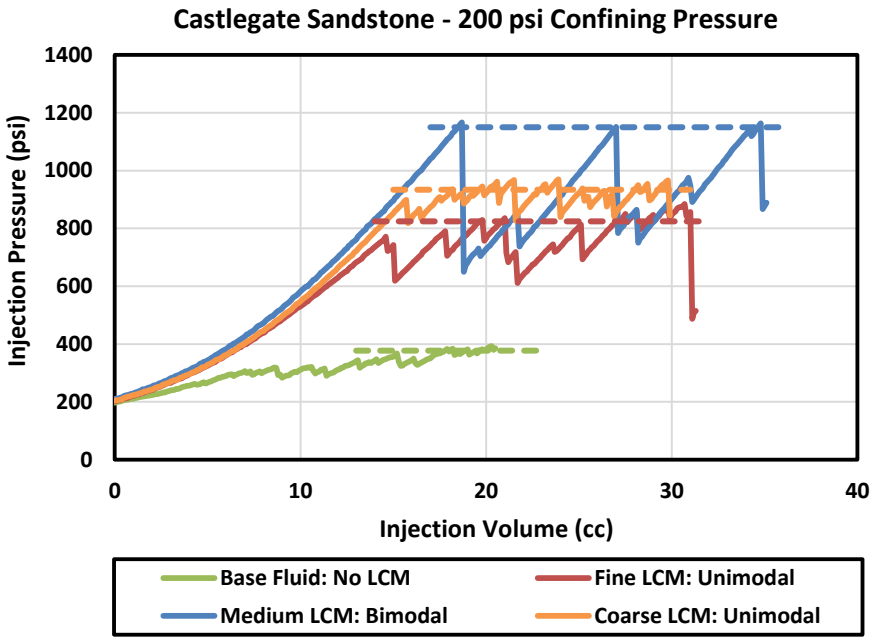
Castlegate Sandstone - 200 psi Confining Pressure
Injection Pressure (psi)
1400
1200
1000
800
600
400
200
0
0
10
20
30
40
Injection Volume (cc)
Base Fluid: No LCM
Fine LCM: Unimodal
Medium LCM: Bimodal
Coarse LCM: Unimodal

(h)

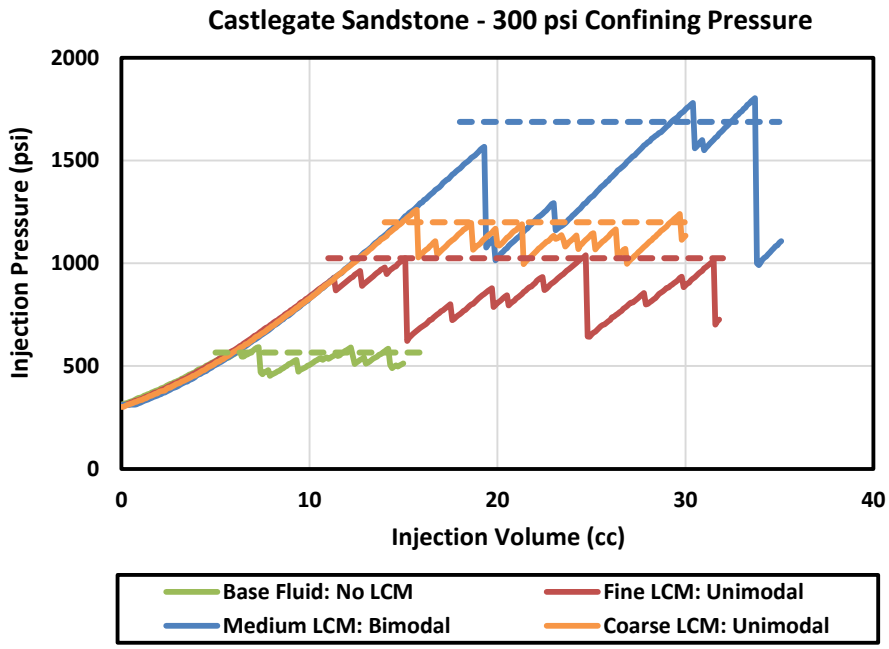
Castlegate Sandstone - 300 psi Confining Pressure
Injection Pressure (psi)
2000
1500
1000
500
0
0
10
20
30
40
Injection Volume (cc)
Base Fluid: No LCM
Fine LCM: Unimodal
Medium LCM: Bimodal
Coarse LCM: Unimodal

(i)

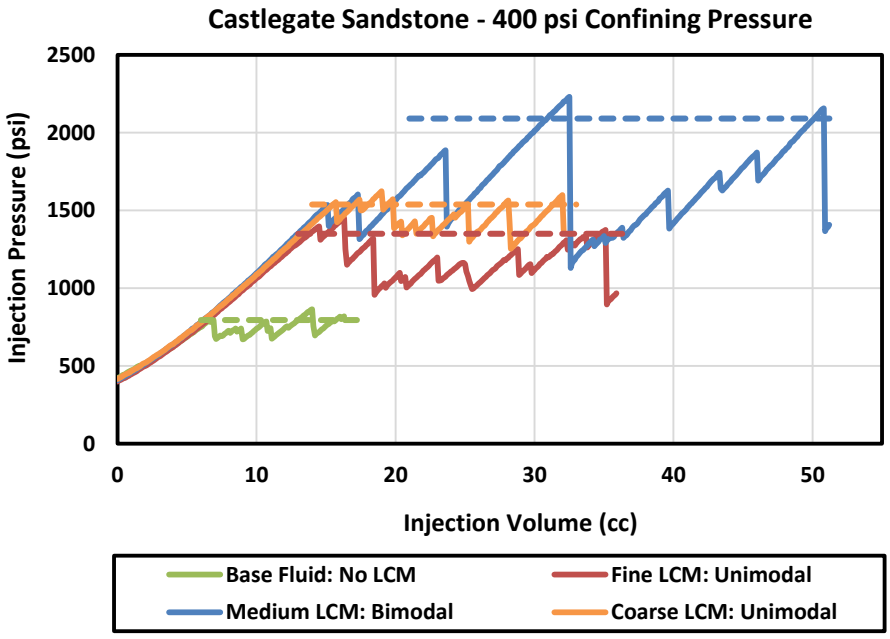
Castlegate Sandstone - 400 psi Confining Pressure
Injection Pressure (psi)
2500
2000
1500
1000
500
0
0
10
20
30
40
50
Injection Volume (cc)
Base Fluid: No LCM
Fine LCM: Unimodal
Medium LCM: Bimodal
Coarse LCM: Unimodal

(j)

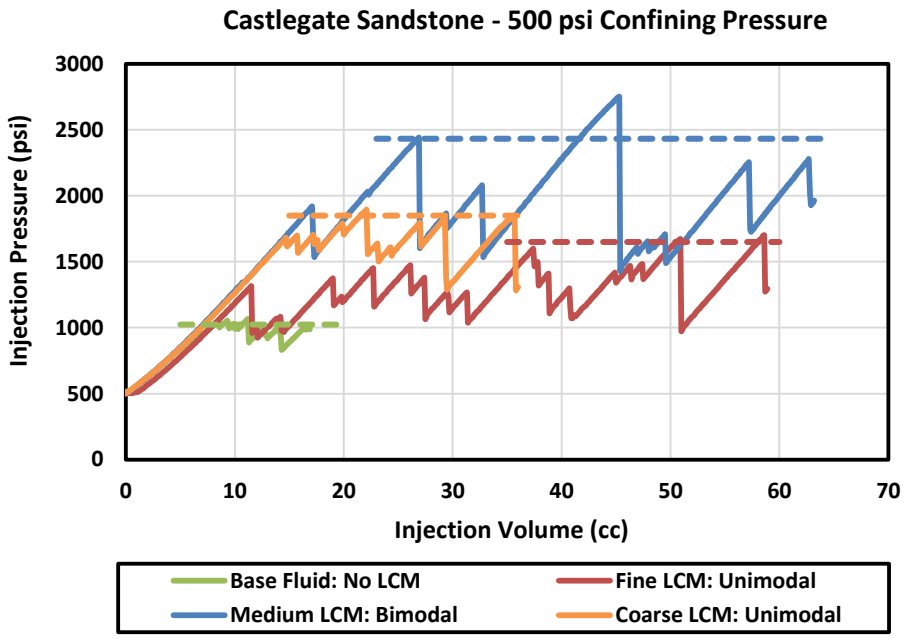

Figure A1 – Fracture propagation injections with various LCM PSDs: (a-e) fracture propagation injection curves using Berea sandstone; (f-j) fracture propagation injection curves using Castlegate sandstone. For each injection curve, the average FPP is indicated using a dashed line.

APPENDIX II: FRACTURE PROPAGATION INJECTION CURVES FOR BEREA SANDSTONE USING VARIOUS LCM TYPES

This appendix presents the supporting information for Section 5.1.2. Figure A2 illustrates the fracture propagation injection curves for SBM loaded with Gilsonite 1, Gilsonite 2, and medium graphite LCMs using Berea sandstone. The average FPP for each injection curve is indicated using a dashed line on each curve.

(a)

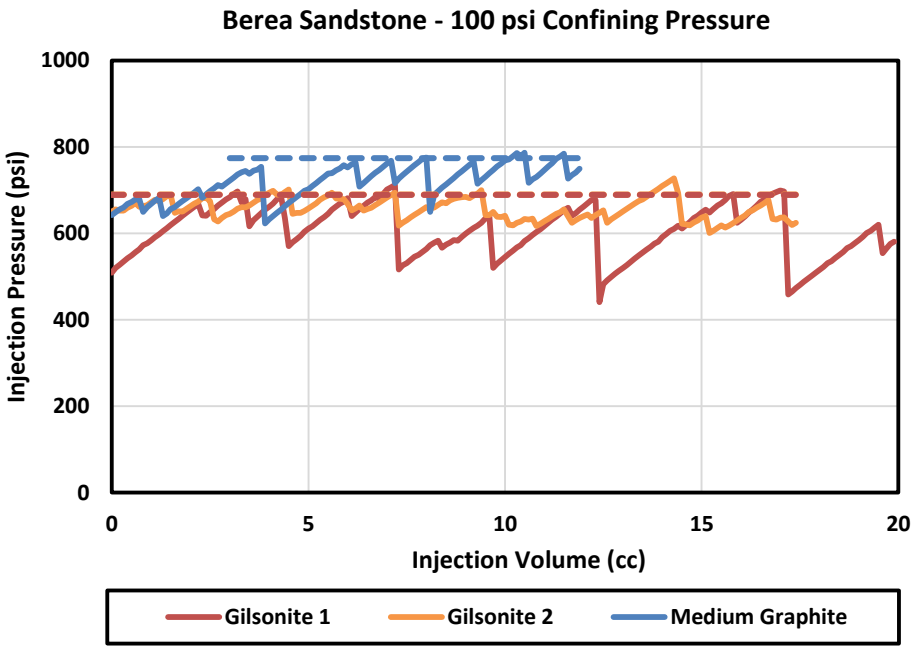

(b)

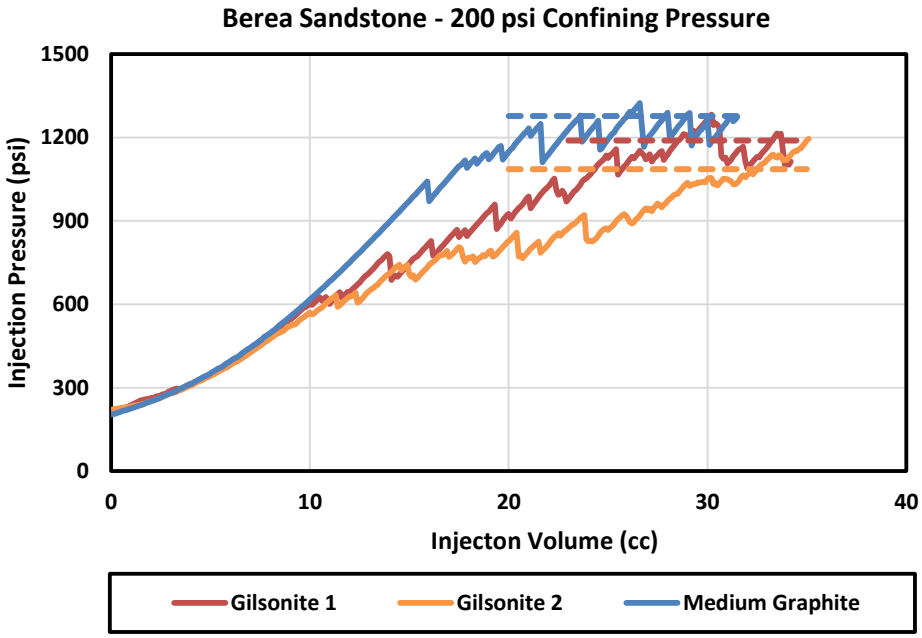
Berea Sandstone - 200 psi Confining Pressure
Injection Pressure (psi)
1500
1200
900
600
300
0
0
10
20
30
40
Injecton Volume (cc)
Gilsonite 1
Gilsonite 2
Medium Graphite

(c)

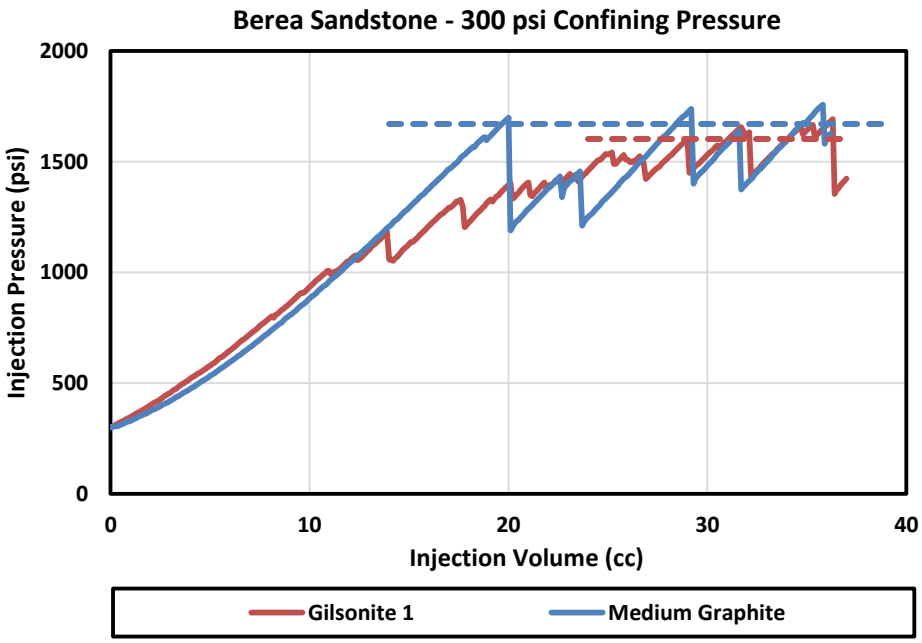
Berea Sandstone - 300 psi Confining Pressure
Injection Pressure (psi)
2000
1500
1000
500
0
0
10
20
30
40
Injection Volume (cc)
Gilsonite 1
Medium Graphite

(d)

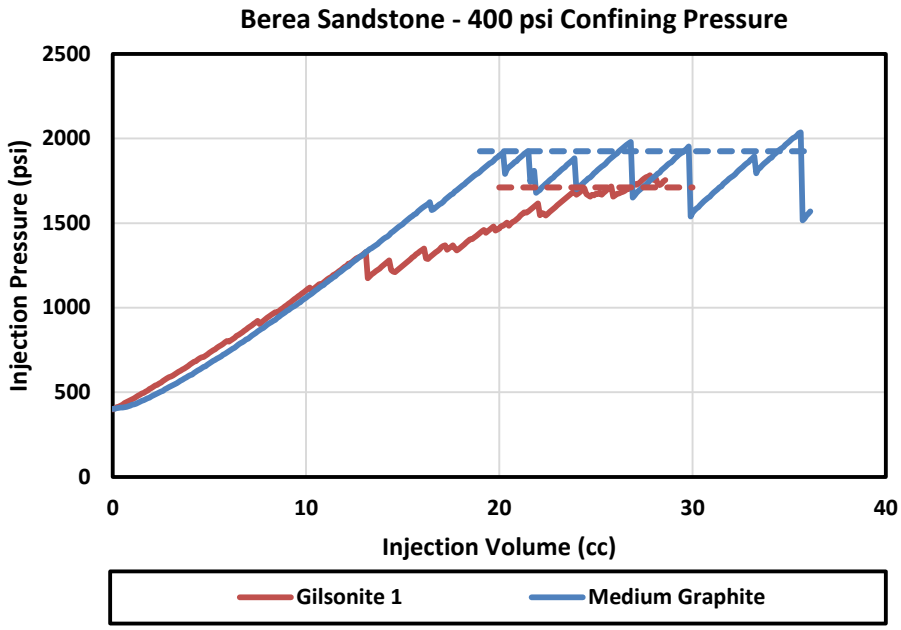

(e)

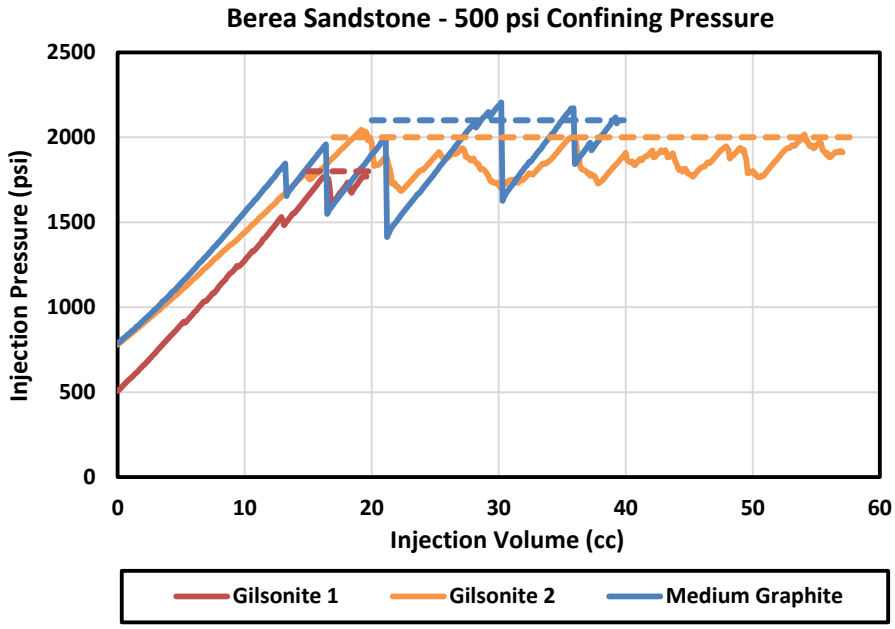

Figure A2 – Fracture propagation injections curve with various LCM type. Fracture propagation injections were conducted on Berea sandstone samples using medium graphite and Gilsonite 1 and 2. For each injection curve, the average FPP is indicated using a dashed line.

APPENDIX III: FRACTURE PROPAGATION INJECTION CURVES FOR BEREA AND CASTLEGATE SANDSTONE USING VARIOUS LCM CONCENTRATIONS

This appendix presents the supporting information for Section 5.1.3. Figure A3 illustrates the fracture propagation injection curves using SBM loaded with various levels of medium graphite LCM concentrations. Berea sandstone tests were conducted using no LCM, 10, 15, 20, and 30 ppb LCM concentration. Castlegate sandstone tests were conducted using no LCM, 5, 10, and 20 ppb LCM concentration. The average FPP for each injection curve is indicated using a dashed line on each curve.

(a)

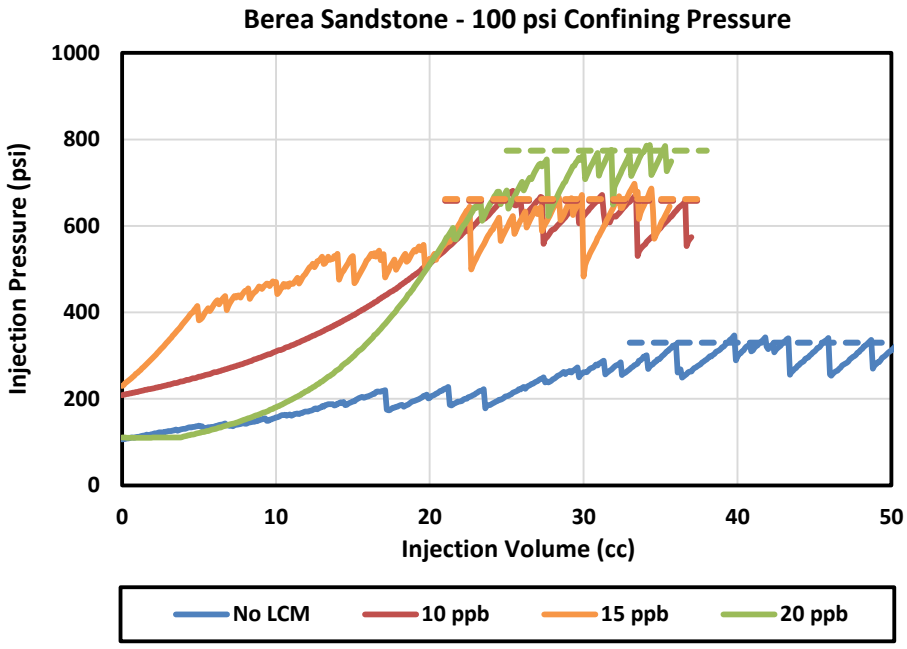

(b)

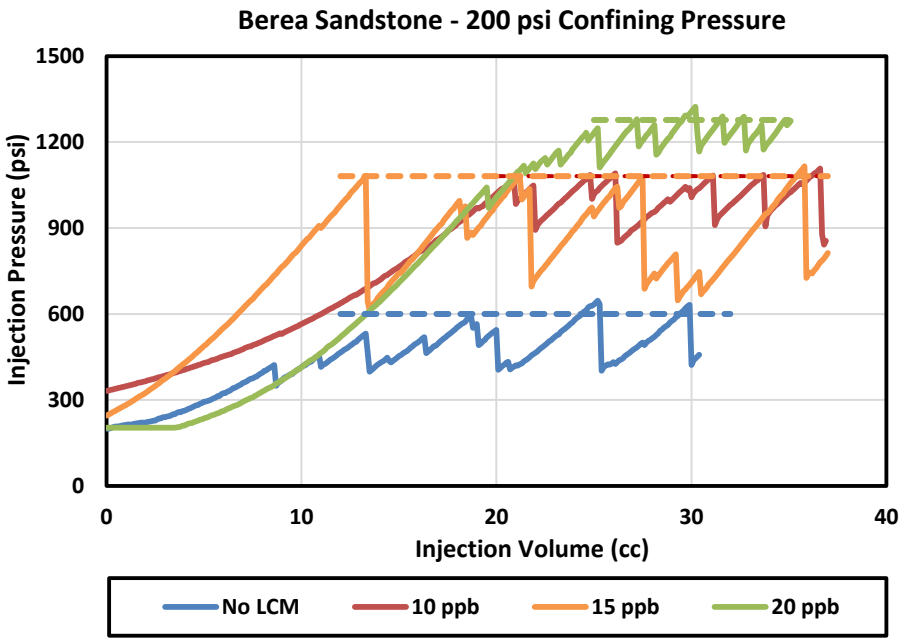
Berea Sandstone - 200 psi Confining Pressure
Injection Pressure (psi)
1500
1200
900
600
300
0
0
10
20
30
40
Injection Volume (cc)
No LCM
10 ppb
15 ppb
20 ppb

(c)

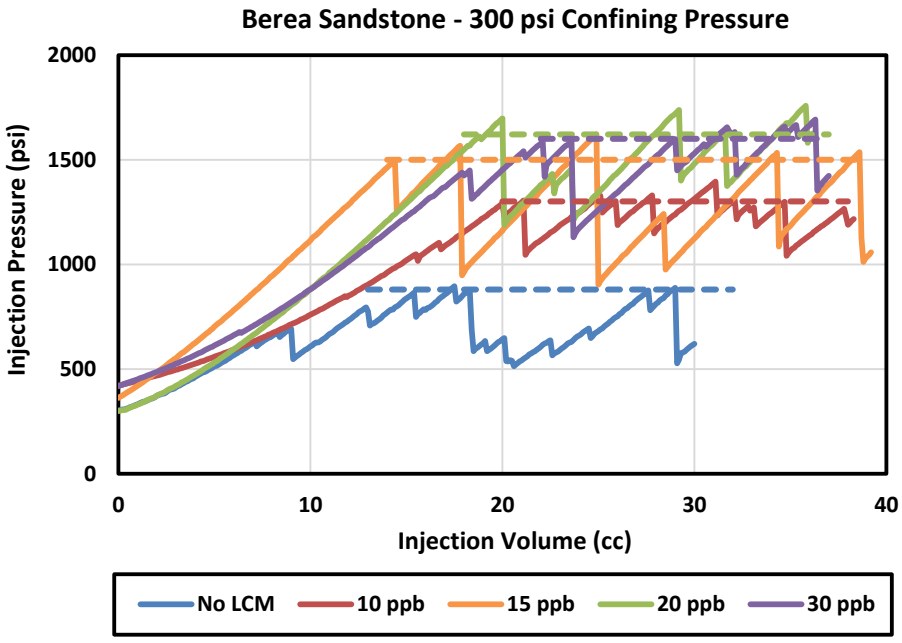
Berea Sandstone - 300 psi Confining Pressure
Injection Pressure (psi)
2000
1500
1000
500
0
0
10
20
30
40
Injection Volume (cc)
No LCM
10 ppb
15 ppb
20 ppb
30 ppb

(d)

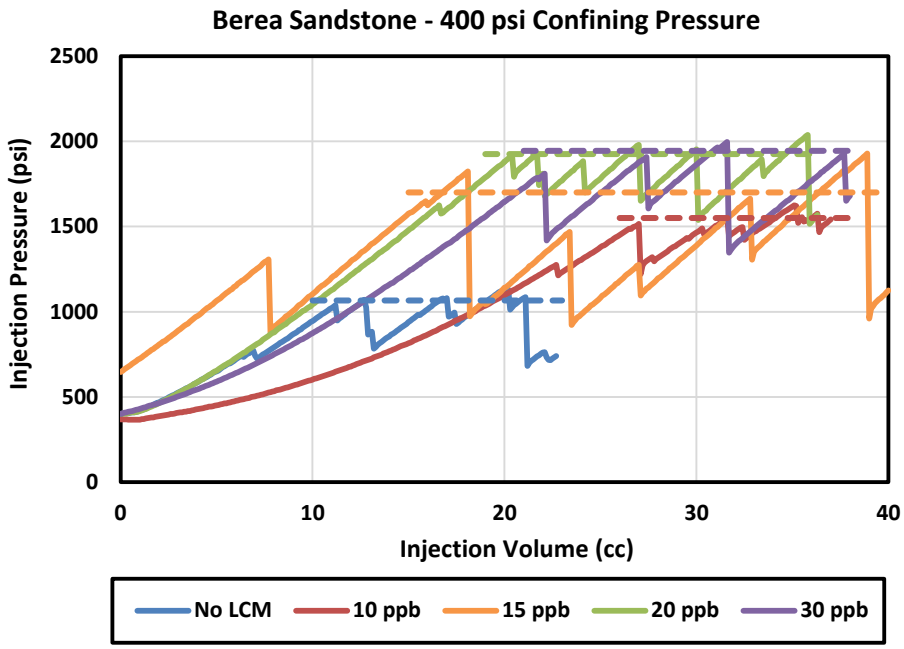
Berea Sandstone - 400 psi Confining Pressure
Injection Pressure (psi)
2500
2000
1500
1000
500
0
0
10
20
30
40
Injection Volume (cc)
No LCM
10 ppb
15 ppb
20 ppb
30 ppb

(e)

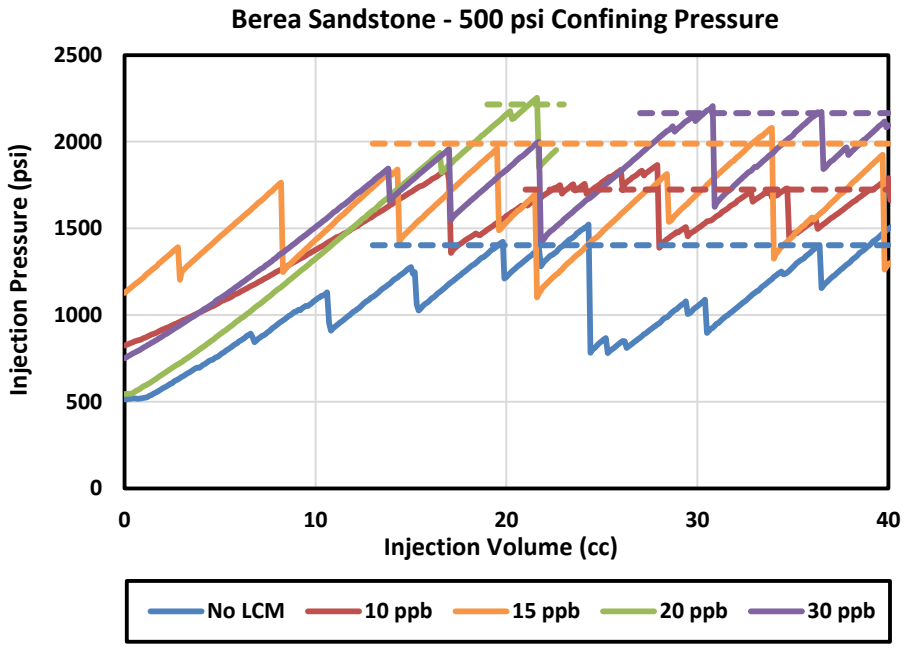
Berea Sandstone - 500 psi Confining Pressure
Injection Pressure (psi)
2500
2000
1500
1000
500
0
0
10
20
30
40
Injection Volume (cc)
No LCM
10 ppb
15 ppb
20 ppb
30 ppb

(f)

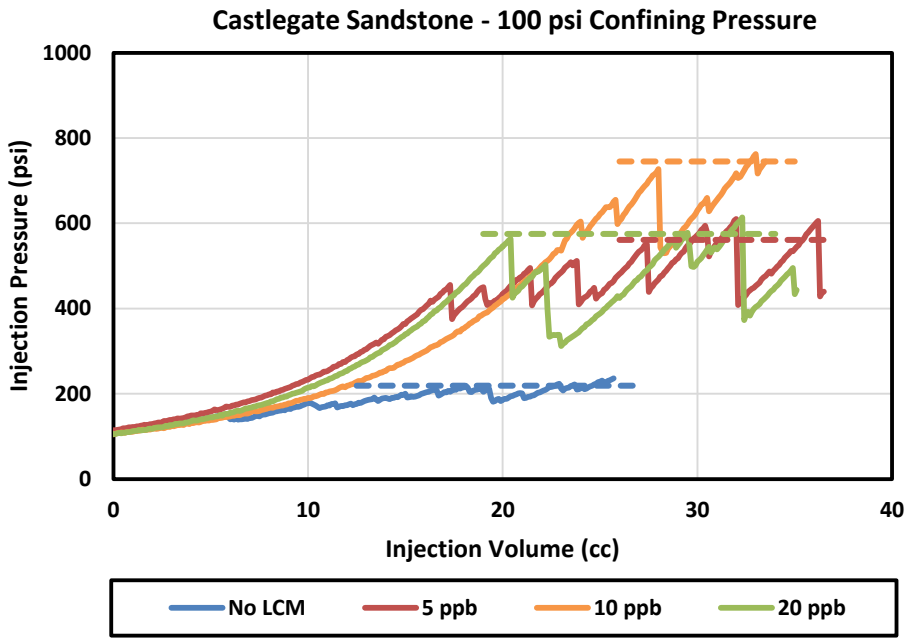
Castlegate Sandstone - 100 psi Confining Pressure
Injection Pressure (psi)
1000
800
600
400
200
0
0
10
20
30
40
Injection Volume (cc)
No LCM
5 ppb
10 ppb
20 ppb

(g)

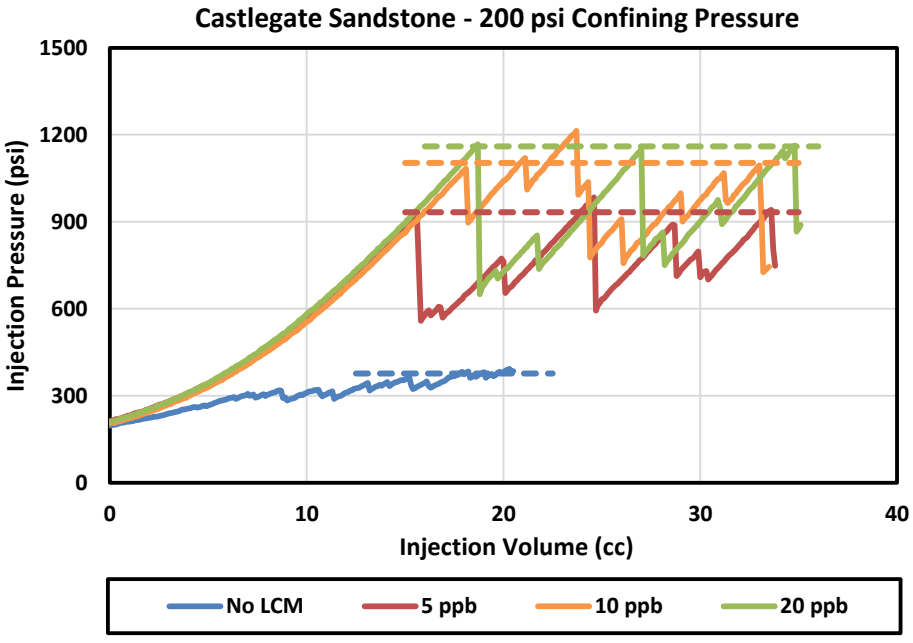
Castlegate Sandstone - 200 psi Confining Pressure
Injection Pressure (psi)
1500
1200
900
600
300
0
0
10
20
30
40
Injection Volume (cc)
No LCM
5 ppb
10 ppb
20 ppb

(h)

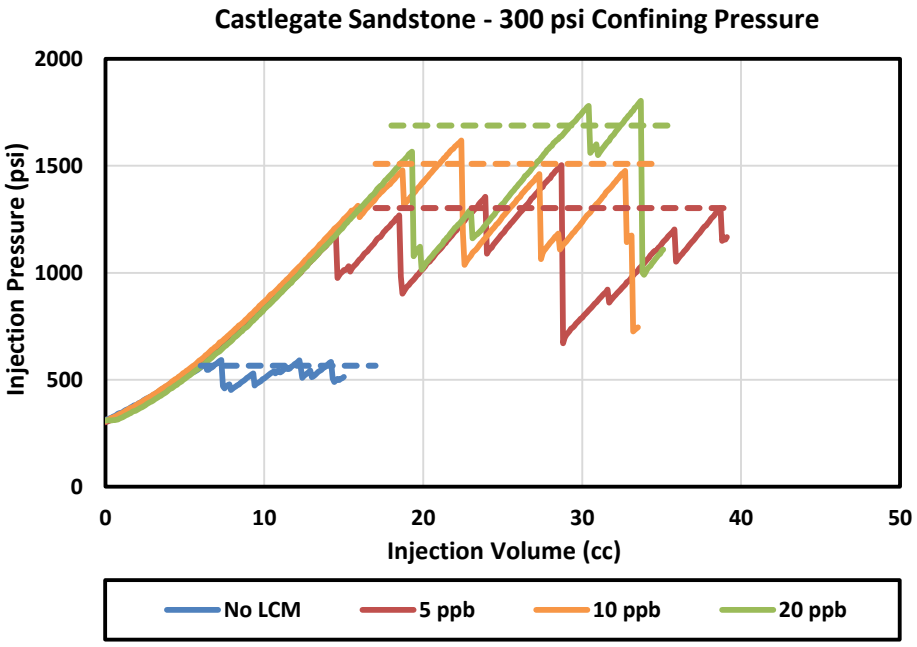
Castlegate Sandstone - 300 psi Confining Pressure
Injection Pressure (psi)
2000
1500
1000
500
0
0
10
20
30
40
50
Injection Volume (cc)
No LCM
5 ppb
10 ppb
20 ppb

(i)

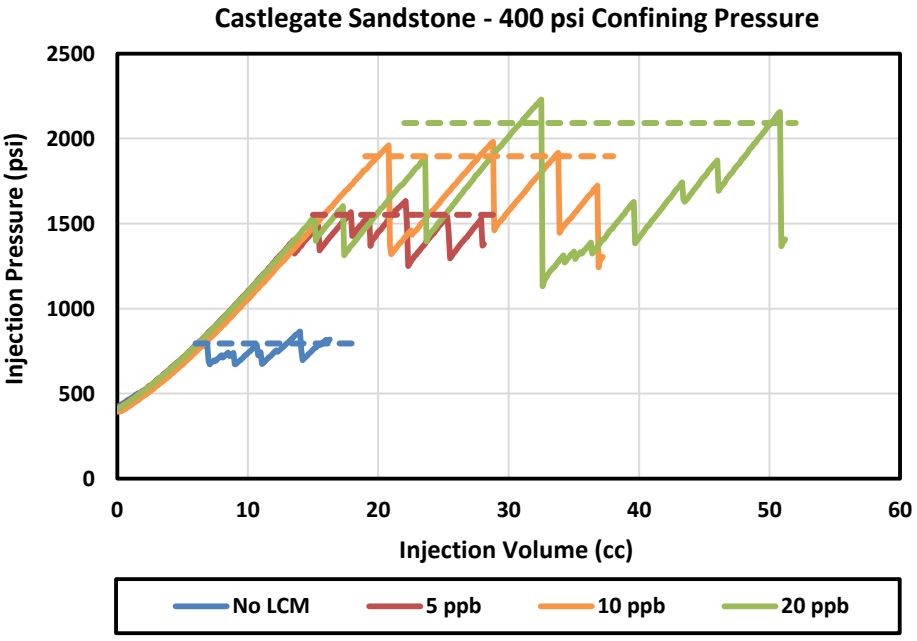
Castlegate Sandstone - 400 psi Confining Pressure
Injection Pressure (psi)
2500
2000
1500
1000
500
0
0
10
20
30
40
50
60
Injection Volume (cc)
No LCM
5 ppb
10 ppb
20 ppb

(j)

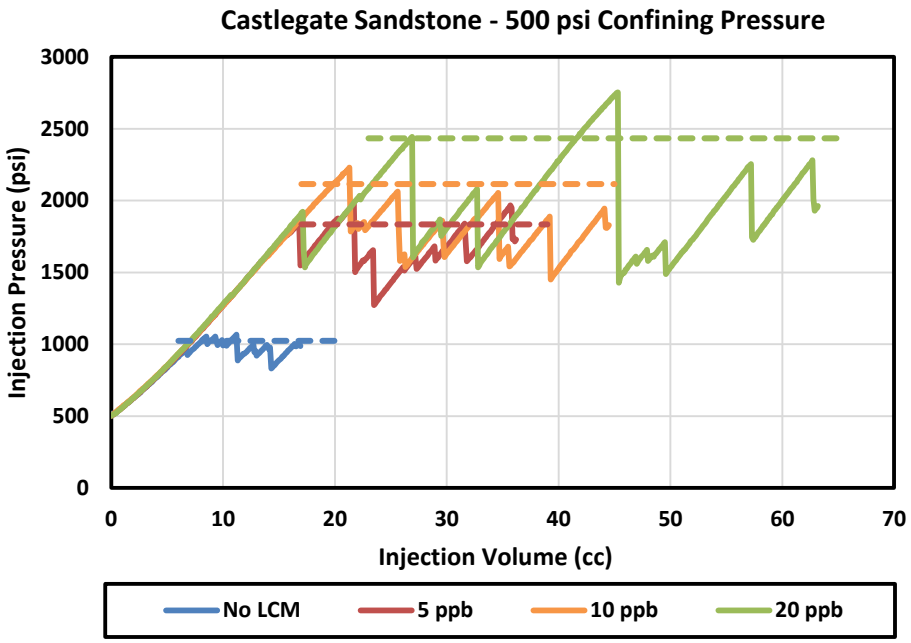

Figure A3 – Fracture propagation injections with various LCM concentrations: (a-e) fracture propagation injection curves using Berea sandstone for various LCM concentrations; (f-j) fracture propagation injection curves using Castlegate sandstone for various LCM concentration. For each injection curve, the average FPP is indicated using a dashed line.

APPENDIX IV: FRACTURE PROPAGATION INJECTION CURVES FOR BEREA AND CASTLEGATE SANDSTONE USING SBM WITH AND WITHOUT LCM

This appendix presents the supporting information for Section 5.1.5. Figure A4 illustrates the fracture propagation injection curves for Berea and Castlegate sandstone samples tested using SBM without LCM and SBM loaded with 20 ppb of medium graphite-based LCM. Fracture propagation injections were conducted at 100, 200, 300, 400, and 500 psi confining pressure. The average FPP for each injection curve is indicated using a dashed line on each curve.

(a)

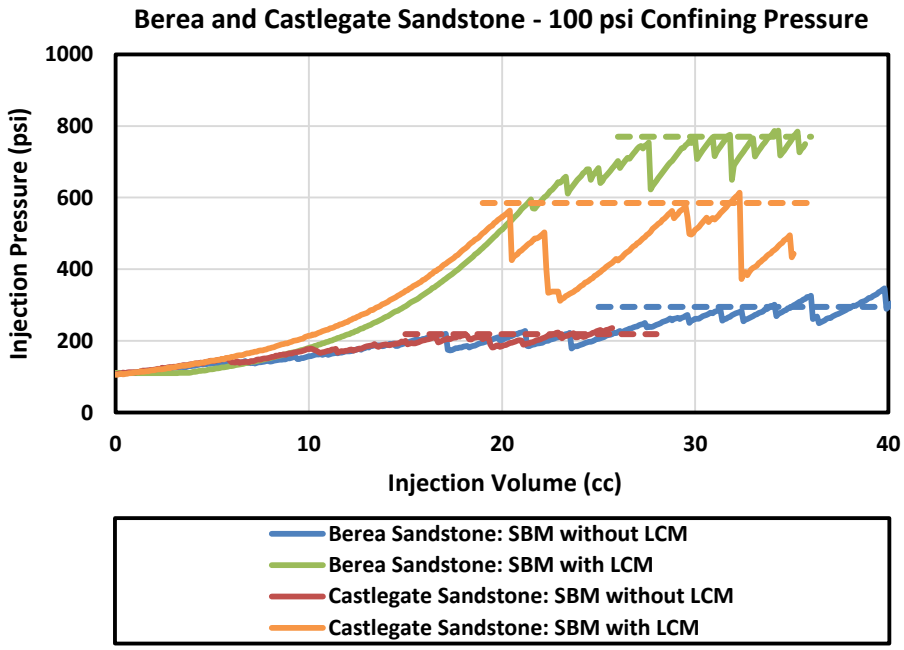

(b)

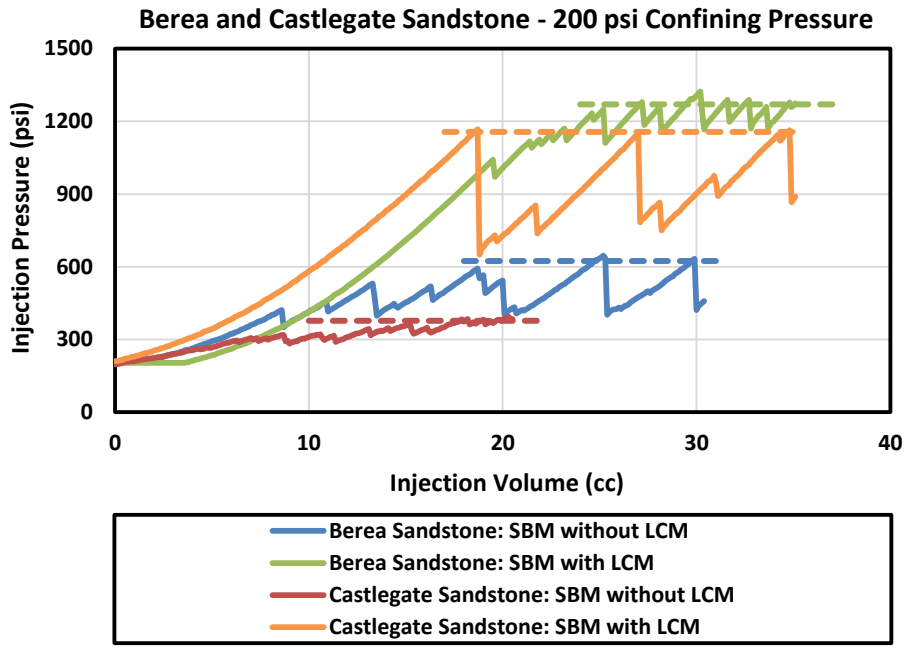
Berea and Castlegate Sandstone - 200 psi Confining Pressure
Injection Pressure (psi)
1500
1200
900
600
300
0
0
10
20
30
40
Injection Volume (cc)
Berea Sandstone: SBM without LCM
Berea Sandstone: SBM with LCM
Castlegate Sandstone: SBM without LCM
Castlegate Sandstone: SBM with LCM

(c)

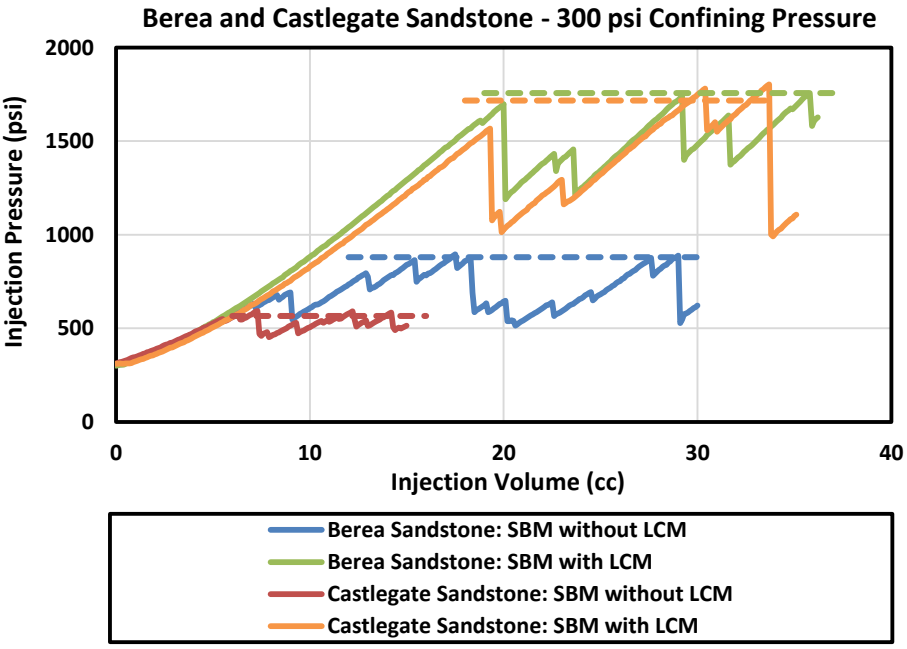
Berea and Castlegate Sandstone - 300 psi Confining Pressure
Injection Pressure (psi)
2000
1500
1000
500
0
0
10
20
30
40
Injection Volume (cc)
Berea Sandstone: SBM without LCM
Berea Sandstone: SBM with LCM
Castlegate Sandstone: SBM without LCM
Castlegate Sandstone: SBM with LCM

(d)

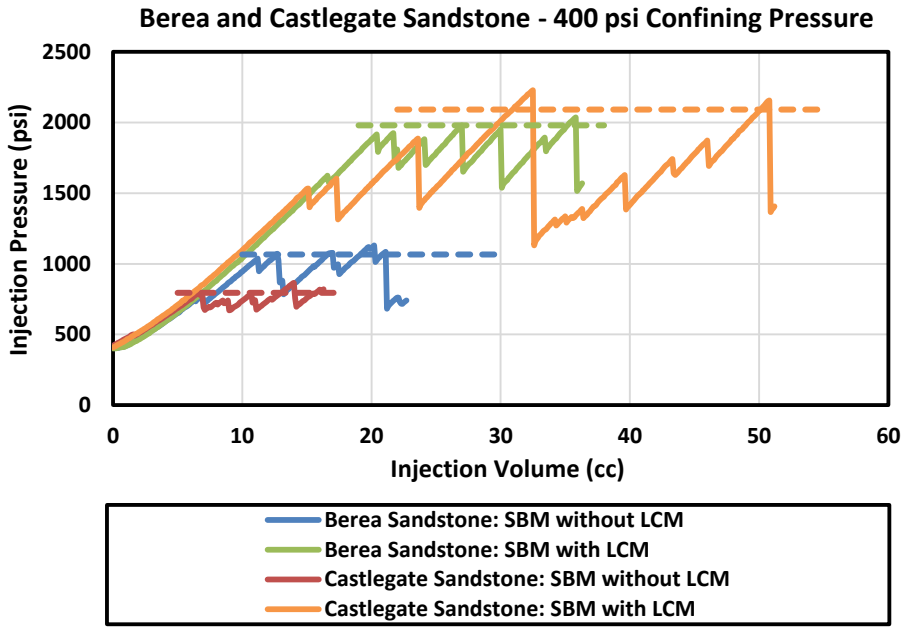

(e)

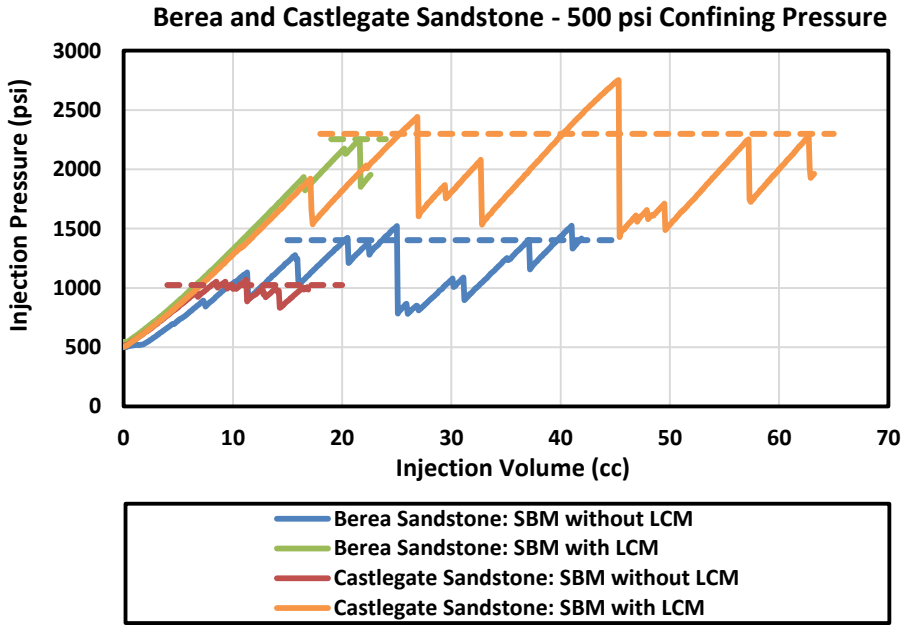

Figure A4 – Fracture propagation injections conducted on Berea and Castlegate sandstone using SBM without LCM and SBM with 20 ppb medium graphite-based LCM. For each injection curve, the average FPP is indicated using a dashed line.

APPENDIX V: FRACTURE PROPAGATION INJECTION CURVES FOR MANCOS SHALE USING VARIOUS DRILLING FLUID SYSTEMS

This appendix presents the supporting information for Section 5.2. Figure A5 illustrates the fracture propagation injection curves for Mancos shale samples tested using SBM without LCM, SBM loaded with 20 ppb of medium graphite-based LCM, Glycol-based WBM, and KCl-based WBM. Fracture propagation injections were conducted at 100, 200, 300, 400, and 500 psi confining pressure. The average FPP for each injection curve is indicated using a dashed line on each curve.

(a)

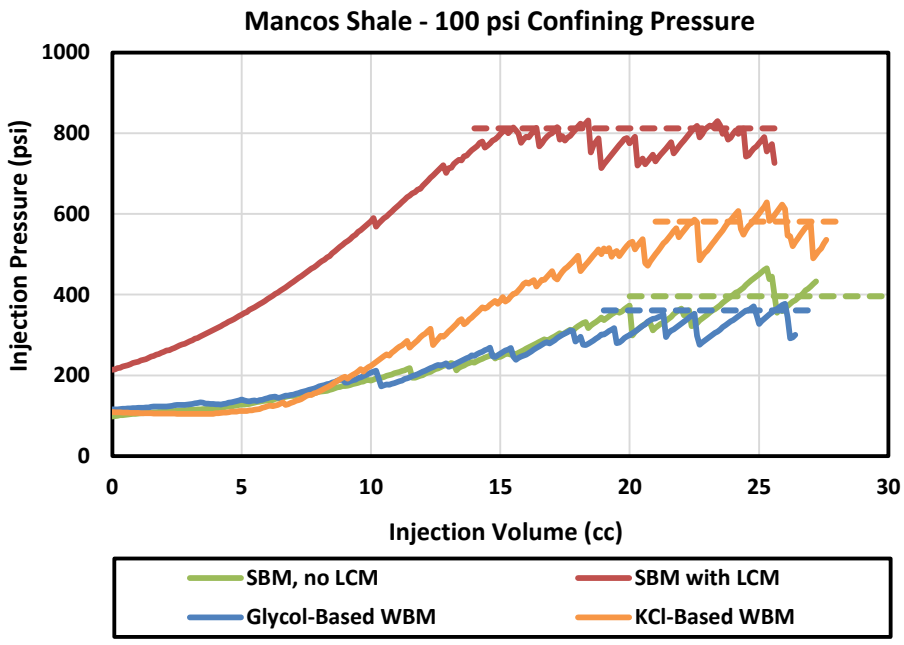

(b)

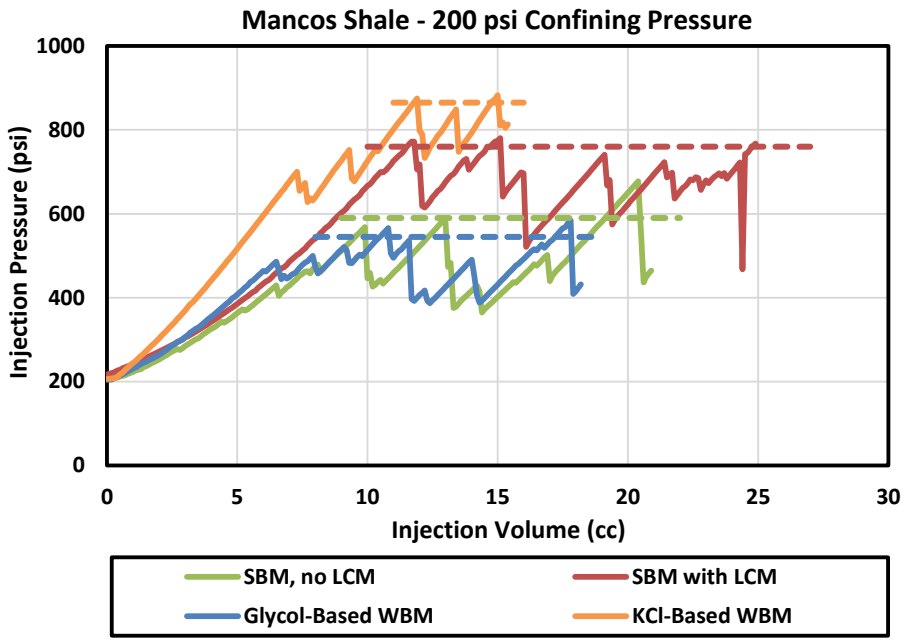
Mancos Shale - 200 psi Confining Pressure
Injection Pressure (psi)
1000
800
600
400
200
0
0
5
10
15
20
25
30
Injection Volume (cc)
SBM, no LCM
SBM with LCM
Glycol-Based WBM
KCl-Based WBM

(c)

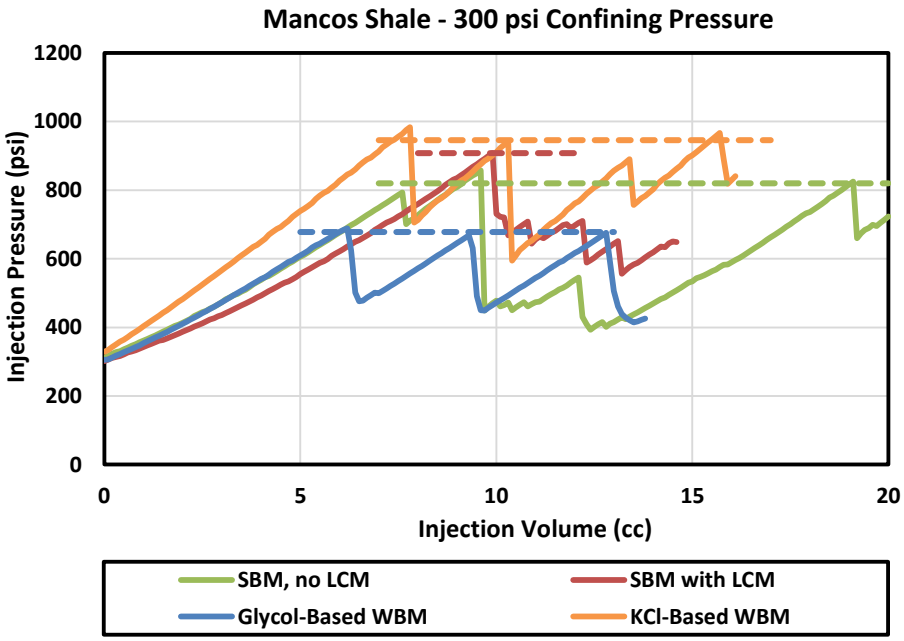
Mancos Shale - 300 psi Confining Pressure
Injection Pressure (psi)
1200
1000
800
600
400
200
0
0
5
10
15
20
Injection Volume (cc)
SBM, no LCM
SBM with LCM
Glycol-Based WBM
KCl-Based WBM

(d)

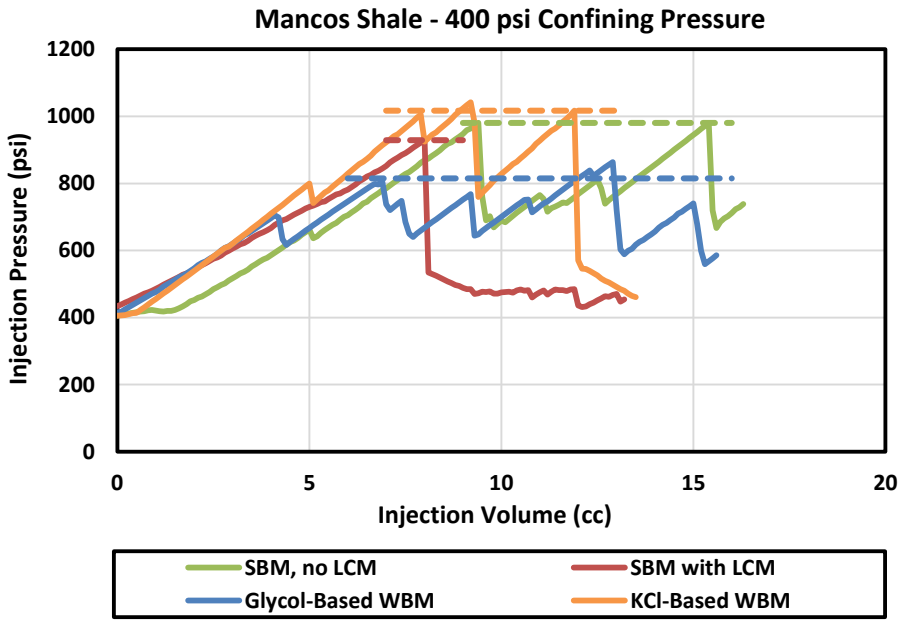

(e)

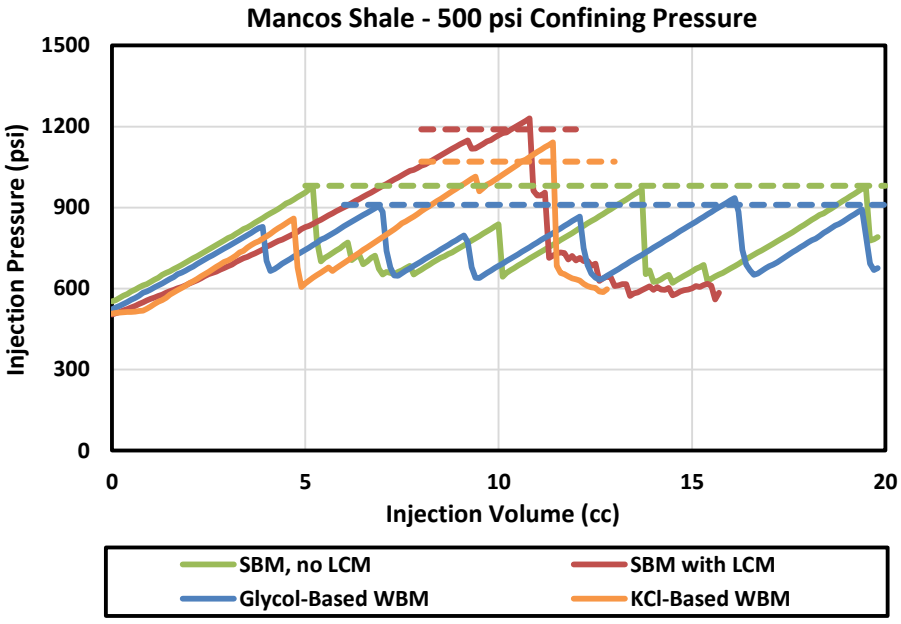

Figure A5 – Fracture propagation injections on Mancos shale samples using SBM without LCM, SBM with 20 ppb medium graphite-based LCM, Glycol-based WBM, KCl-based WBM. For each injection curve, the average FPP is indicated using a dashed line.

APPENDIX VI: ANALYSIS OF THE FPP USING OBM WITHOUT LCM

This appendix presents the supporting information for Section 5.4.1. Figure A6 illustrates the fracture propagation injection curves for SBM without LCM at 200, 300, 400, and 500 confining pressures. The average FPP for each confining pressure is marked by a dashed line on the injection pressure curve. Table A1 lists the average FPP extracted from the DEA 13 experiments (phase 1 and 2) for OBM without LCM.

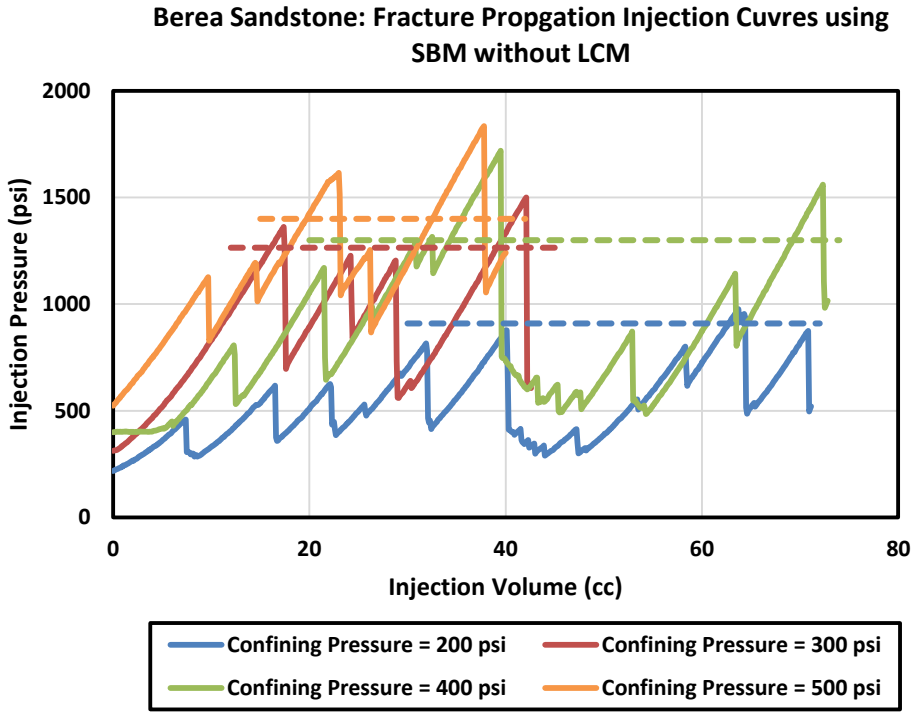

Figure A6 – Fracture propagation injections for SBM without LCM, conducted using the UT MudFrac system. The average FPP is marked by a dashed line on the corresponding injection pressure curve.

Test – Injection	Fluid System	Borehole Diameter (inch)	S_{hmin} (psi)	Average FPP (psi)
4 – 3	16 ppg MOBM	1.5	1800	2827
4 – 4	16 ppg MOBM	1.5	2500	4211
7 – 2	16 ppg MOBM	1.5	1800	2551
7 – 3	16 ppg MOBM	1.5	1800	3105
7 – 4	16 ppg MOBM	1.5	300	1119
13 – 1	16 ppg MOBM	1.5	1800	3362
13 – 2	16 ppg MOBM	1.5	1800	3812
13 – 3	16 ppg MOBM	1.5	1800	3786
13 – 4	16 ppg MOBM	1.5	300	1284
16 – 1	10 ppg MOBM	1.5	1800	3404
16 – 2	10 ppg MOBM	1.5	1800	3671
16 – 3	10 ppg MOBM	1.5	1800	3429
16 – 4	10 ppg MOBM	1.5	300	1295
17 – 1	10 ppg DOBM	1.5	1800	3041
17 – 2	10 ppg DOBM	1.5	1800	3291
17 – 4	10 ppg DOBM	1.5	300	1154
21 – 2	10 ppg MOBM	1.5	1800	3085
21 – 3	10 ppg MOBM	1.5	1800	3118
21 – 4	10 ppg MOBM	1.5	300	1169
22 – 2	10 ppg DOBM	1.5	1800	3386
22 – 3	10 ppg DOBM	1.5	1800	3776
22 – 4	10 ppg DOBM	1.5	300	1241
23 – 2	10 ppg DOBM	1.5	1800	3786

Table A1 – The average FPP measured in the DEA 13 experiments using OBM without LCM

Test – Injection	Fluid System	Borehole Diameter (inch)	S_{hmin} (psi)	Average FPP (psi)
23 – 3	10 ppg DOBM	1.5	1800	2613
27 – 1	16 ppg MOBM	1.5	1800	4091
27 – 2	16 ppg MOBM	1.5	1800	3752
27 – 3	16 ppg MOBM	1.5	1800	3374
27 – 8	16 ppg MOBM	1.5	2500	4130
33 – 1	16 ppg MOBM	1.5	1800	4236
33 – 3	16 ppg MOBM	1.5	1800	3559
33 – 7	16 ppg MOBM	1.5	2500	3761
34 – 3	16 ppg MOBM	1.5	1800	3492
35 – 1	16 ppg MOBM	1.5	1800	2571
35 – 3	16 ppg MOBM	1.5	1800	3395
37 – 1	16 ppg MOBM	1.5	1800	4268
37 – 4A	16 ppg MOBM	1.5	2200	4302
37 – 4B	16 ppg MOBM	1.5	2500	4913
39 – 1	16 ppg MOBM	1.5	1800	4353
39 – 3	16 ppg MOBM	1.5	1800	3882
39 – 4B	16 ppg MOBM	1.5	2500	4078
39 – 8	16 ppg MOBM	1.5	900	2114
39 – 10	16 ppg MOBM	1.5	900	2500
41 – 2B	16 ppg MOBM	4	1800	2940
41 – 4A	16 ppg MOBM	4	300	1719
41 – 4B	16 ppg MOBM	4	900	2223
41 – 6A&B	16 ppg MOBM	4	900	2051

Table A1 – The average FPP measured in the DEA 13 experiments using OBM without LCM (continued)

APPENDIX VII: ANALYSIS OF THE FPP USING OBM WITH GRAPHITE / CALCIUM CARBONATE-BASED LCM

This appendix presents the supporting information for Section 5.4.2. Figure A7 illustrates the fracture propagation injection curves using SBM with 20 ppb of the fine graphite-based LCM at 100, 200, 300, 400, and 500 confining pressures. The average FPP for each confining pressure is marked by a dashed line on the injection pressure curve. Table A2 shows the average FPP extracted from the DEA 13 experiments (phase 2) using 16 ppg MOBM with 40 or 80 ppb of calcium carbonate-based LCM.

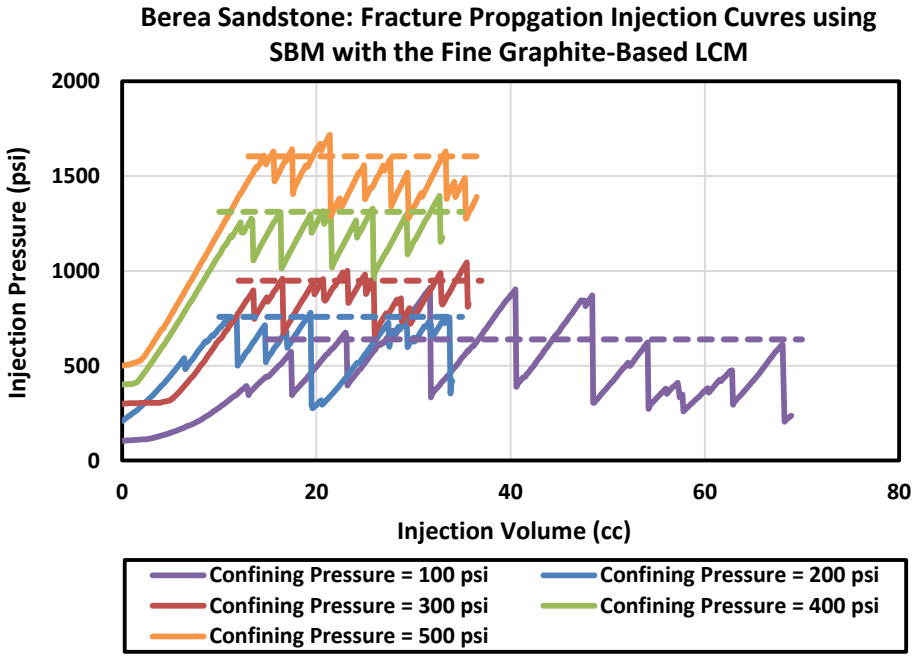

Figure A7 – Fracture propagation injections for SBM with 20 ppb of fine graphite-based LCM, conducted using the UT MudFrac system. The average FPP is marked by a dashed line on the corresponding injection pressure curve.

Test – Injection	LCM Concentration (ppb)	Borehole Diameter (inch)	S_{hmin} (psi)	Average FPP (psi)
27 – 4	40	1.5	1800	4852
27 – 7	40	1.5	2500	6178
34 – 2	80	1.5	1800	4758
35 – 4	40	1.5	1800	4538
41 – 5	80	4	900	2713

Table A2 – The average FPP measured in the DEA 13 experiments using 16 ppg MOBM with calcium carbonate-based LCM

APPENDIX VIII: ANALYSIS OF THE FPP USING OBM WITH GILSONITE-BASED LCM

This appendix presents the supporting information for Section 5.4.3. Figure A8 illustrates the fracture propagation injection curves using SBM with 20 ppb of the Gilsonite-based LCM at 200, 300, 400, and 500 confining pressures. The average FPP for each confining pressure is marked by a dashed line on the injection pressure curve. Table A3 shows the average FPP extracted from the DEA 13 experiments (phase 2) for 16 ppg MOBM loaded with 40 or 80 ppb of Gilsonite-based LCM.

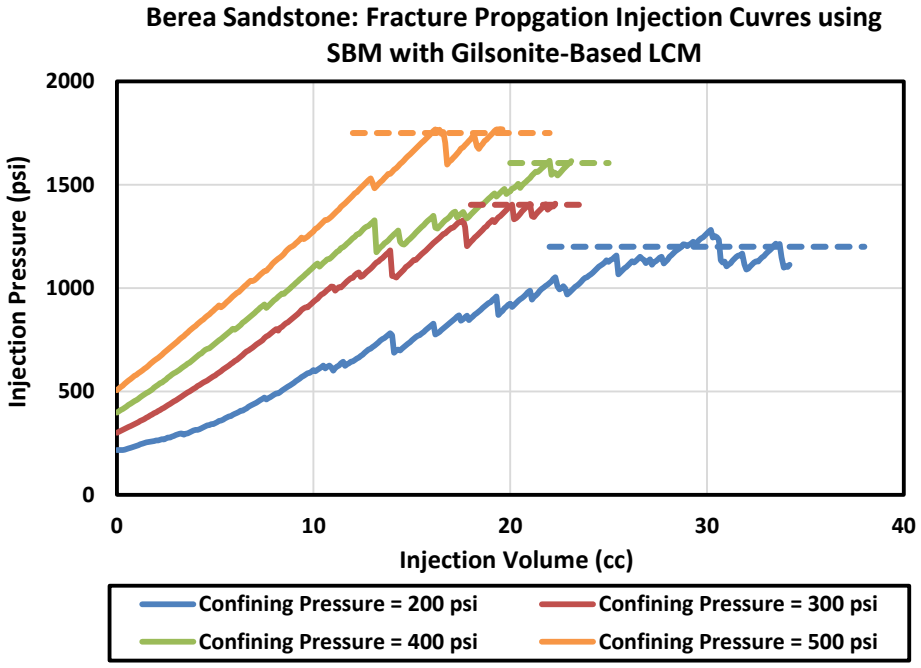

Figure A8 – Fracture propagation injections using SBM with 20 ppb of Gilsonite-based LCM, conducted using the UT MudFrac system. The average FPP is marked by a dashed line on the corresponding injection pressure curve.

Test – Injection	LCM Concentration (ppb)	Borehole Diameter (inch)	S_{hmin} (psi)	Average FPP (psi)
38 – 2	40	1.5	1800	4620
38 – 3	40	1.5	1800	4288
38 – 4A	80	1.5	2500	5509
38 – 4E	80	1.5	2500	5562
41 – 3 A&B	80	4	1800	3941

Table A3 – The average FPP extracted from the DEA 13 experiments using 16 ppg MOBM loaded with Gilsonite-based LCM

Glossary

CAT	Computerized Axial Tomography
CV	Cumulative Volume
DEA	Drilling Engineering Association
DGD	Dual Gradient Drilling
DIF	Drilling Induced Fracture
DOBM	Diesel Oil Based Mud
FBP	Formation Breakdown Pressure
FCS	Fracture Closure Stress
FIP	Fracture Initiation Pressure
FPP	Fracture Propagation Pressure
FPR	Fracture Propagation Resistance
GPRI	Global Petroleum Research Institute
JIP	Joint Industry Project
LCM	Lost Circulation Material
LOT	Leak-Off Testing
MOBM	Mineral Oil Based Mud
MPD	Managed Pressure Drilling
OBM	Oil Based Mud
PPA	Pore Plugging Apparatus
ppb	pounds per barrel
ppg	pounds per gallon
PSD	Particle Size Distribution
S_{hmin}	Minimum Horizontal Stress
S_{hmax}	Maximum Horizontal Stress
S_v	Vertical Stress
SBM	Synthetic Based Mud

SC	Stress Caging
SD	Standard Deviation
UCS	Unconfined Compressive Strength
UFP	Uncontrolled Fracture Pressure
WBM	Water Based Mud
WBS	Wellbore Strengthening
WSA	Wellbore Stress Augmentation

Nomenclature

a	Length of the pre-existing fracture (inches)
b	Dimensionless length parameter
CDF	Cumulative distribution function
CV	Cumulative volume
D	Particle size (microns)
D_{10}	Mass division diameter greater than 10 percent of the sample particles (microns).
D_{25}	Mass division diameter greater than 25 percent of the sample particles (microns).
D_{50}	Mass division diameter greater than 50 percent of the sample particles (microns).
D_{75}	Mass division diameter greater than 75 percent of the sample particles (microns).
D_{90}	Mass division diameter greater than 90 percent of the sample particles (microns).
D_{100}	Mass division diameter greater than 100 percent of the sample particles (microns).
D_{mp}	Maximum pore diameter (microns)
F	Dimensionless stress intensity factor for the maximum horizontal stress
FIP	Fracture initiation pressure (psi)
G	Dimensionless stress intensity factor for the minimum horizontal stress
h_a	Dimensionless stress intensity factor for the pressure distribution within the fracture
h_0	Dimensionless stress intensity factor for the pressure distribution within the borehole
K_{IC}	Fracture toughness ($psi\sqrt{inch}$)
M	The arithmetic mean value (microns)
P_P	Pore pressure (psi)
PSD	Cumulative particle size distribution
R	Borehole radius (inches)
SD	Standard deviation (microns)

S_{hmax}	Effective maximum horizontal stress (psi)
S_{hmin}	Effective minimum horizontal stress (psi)
T_0	Tensile strength (psi)
x	The exponent value in the power-law model used in the ideal packing theory
σ	Scale parameter of the log-normal distribution
$\sigma_{Confining}$	Confining pressure (psi)
μ	Location parameter of the log-normal distribution
ω	Concentration

References

Abrams, A. Mud Design to Minimize Rock Impairment Due to Particle Invasion. Journal of Petroleum Technology, Volume 29, Issue 05, pp. 586 – 592, May 1977.

Abou-Sayed, A. S., Brechtel, C. E., and Clifton, R. J. In Situ Stress Determination by Hydrofracturing: a Fracture Mechanics Approach. Journal of Geophysical Research: Solid Earth, Volume 83, Issue B6, pp. 2851-2862, 1978.

Alberty, M.W and McLean, M.R. A Physical Model for Stress Cages. Paper presented at the SPE Annual Technical Conference and Exhibition, Houston, Texas, USA. September 26 – 29, 2004.

Alberty, M.W., Aston, M.S. and McLean, M.R. Drilling Method, Patent US 7431106. Oct.7, 2008

Andreasen, A.H.M., and Andersen, J. Ueber die Beziehung zwischen Kornabstufung und Zwischenraum in Produkten aus losen Körnern (mit einigen Experimenten). Kolloid-Zeitschrift 50, pp. 217 – 228, 1930.

Aston, M.S., Alberty, M.W, McLean, M.R., de Jong, H.J., and Armagost, K. Drilling Fluids for Wellbore Strengthening. Paper presented at the SPE/IADC Drilling Conference and Exhibition, Dallas, Texas, USA. March 2 – 4 2004.

Aston, M., Alberty, M.W, Duncum, S., Bruton, J.R., Friedheim, J.E. and Sanders, M.W. A New Treatment for Wellbore Strengthening in Shale. Paper presented at the SPE Annual Technical Conference and Exhibition, Anaheim, California, USA. November 11 – 14, 2007.

Chellappah, K., and Aston, M. S. A New Outlook on the Ideal Packing Theory for Bridging Solids. Paper Presented at the SPE International Symposium and Exhibition on Formation Damage Control, Lafayette, Louisiana, USA. February 15 – 17, 2012.

DEA 13 (Phase I) Final Report. Investigation of Lost Circulation Problems and Apparent Fracture Gradient Reduction Encountered in the Field with Oil-Based Drilling Fluids during Large-Scale Laboratory Fracturing Experiments. Prepared by Drilling Research Laboratory, Inc. December 1985.

DEA 13 (Phase II) Final Report. Investigation of Lost Circulation Problems with Oil-Base Drilling Fluids. Prepared by Drilling Research Laboratory, Inc. March 1988.

Dick, M.A., Heinz, T.J., Svoboda, C.F., and Aston, M. Optimizing the Selection of Bridging Particles for Reservoir Drilling Fluids. Paper presented at the SPE International Symposium and Exhibition on Formation Damage, Lafayette, LA, USA. February 23 – 24, 2000.

Dudley, J.W., Fehler, D.F., and Zeilinger, S. Final Project Report of GPRI 2000 Project DC3: Minimizing Lost Circulation in Synthetic Mud. Shell International Exploration and Production, Inc. Bellaire Technology Center. 2000.

Dupriest, F.E. Fracture Closure Stress (FCS) and Lost Returns Practices. Paper presented at the SPE/IADC Drilling Conference and Exhibition, Amsterdam, The Netherlands. February 23 – 25, 2005.

Dupriest, F.E., Smith, M.V., Zeilinger, C.S., Shoykhet, I.N. Method to Eliminate Lost Returns and Build Integrity Continuously With High-Filtration-Rate Fluid. Paper presented at the IADC/SPE Drilling Conference and Exhibition, Orlando, Florida, USA. March 4 – 6, 2008.

Fuh, G.F, Morita, N., Boyd, P.A., McGoffin, S.J. A New Approach to Preventing Lost Circulation While Drilling. Paper presented at the SPE Annual Technical Conference and Exhibition, Washington D.C., USA. October 4 – 7, 1992.

Fuh, G.F., Morita, N., Whitfill, D.L., Strah, D.A. Method for inhibiting the initiation and propagation of formation fractures while drilling and casing a well. US Patent 5180020 A. Jan 19, 1993.

Gradishar, J., Ugueto, G., and van Oort, E. Setting Free the Bear: The Challenges and Lessons of The Ursa A-10 Deepwater ERD Well. Paper presented at the SPE/IADC Conference and Exhibition, Amsterdam, The Netherlands. March 5 – 7, 2013.

Guo, Q., Roy, S., Simpkins, D., and Zamora, M. A Practical Design Tool for Wellbore Strengthening. Paper presented at the AADE Fluid Conference and Exhibition, New Orleans, Louisiana, USA. April 8 – 9, 2009.

Guo, Q., Cook, J., Way, P., Ji, L., and Friedheim, J. E. A Comprehensive Experimental Study on Wellbore Strengthening. Paper presented at the IADC/SPE Drilling Conference and Exhibition, Fort Worth, Texas, USA. March 4 – 6, 2014.

Hardy, M.P. Fracture Mechanics Applied to Rocks. PhD Dissertation, University of Minnesota. 1973.

Haimson, B., and Fairhurst, C. In-Situ Stress Determination at Great Depth by Means of Hydraulic Fracturing. Proceedings of the Eleventh Symposium on Rock Mechanics, University of California, p. 559. June 1969.

Hubbert, M. K. and D. G. Willis. Mechanics of Hydraulic Fracturing, Trans. AIME. Volume 210, pp. 153 – 166, 1957.

Jacobs, T. Pushing the Frontier through Wellbore Strengthening. Journal of Petroleum Technology, Volume 66, Issue 11, pp. 64 – 73. November 2014.

Johnston, I. W., and S. K. Choi. A synthetic soft rock for laboratory model studies. Géotechnique, Volume 36, Issue 2, pp. 251-263, 1986.

Kaeuffer, M. Determination de L'Optiumum de Remplissage Granulometrique et Quelques Proprietes S'y Rattachant. Paper presented at Congres International de I'A.F.T.P.V., Rouen, pp. 1-12. October 1973.

Kageson-Loe, N. M., Sanders, M. W., Growcock, F., Taugbol, K., Horsrud, P., Singelstad, A. V., and Omland, T. H. Particulate Based Loss-Prevention Material—The Secrets of Fracture Sealing Revealed! Paper presented at the IADC/SPE Drilling Conference and Exhibition, Orlando, Florida, USA. March 4 – 6, 2008.

Karimi Vajargah, A. and van Oort, E. Automated Drilling Fluid Rheology Characterization with Downhole Pressure Sensor Data. Paper presented in the IADC/SPE Drilling Conference and Exhibition, London, England, UK. March 17 – 19, 2015.

Kirsch, G. Z. Verein Deutscher Ing. VDI. 42, p. 113. 1898.

Mehrabian, A., Jamison, D. E., and Teodorescu, S. G. Geomechanics of Lost-Circulation Events and Wellbore-Strengthening Operations. SPE Journal, Volume 20, Issue 6, pp. 1305 – 1316, December 2015.

Mehrabian, A. The Stability of Inclined and Fractured Wellbores. SPE Journal. March 2016.

Mehrabian, A and Abousleiman, Y.N. Wellbore Geomechanics of Extended Drilling Margins and Engineered Lost Circulation Solutions. Paper presented in the ARMA Geomechanics Symposium, Houston, Texas, USA. June 26 – 29, 2016.

Morita, N., Black, A.D., Guh, G.F. Theory of Lost Circulation Pressure. Paper presented at the SPE Annual Technical Conference and Exhibition, New Orleans, Louisiana, USA. September 23 – 26, 1990.

Morita, N., Black, A.D., Fuh, G.F. Borehole breakdown pressure with drilling fluids - I. Empirical results. International Journal of Rock Mechanics and Mining Sciences and Geomechanics Abstracts, Volume 33, Issue 1, pp. 39 – 51, January 1996.

Morita, N., Black, A.D., Fuh, G.F. Borehole breakdown pressure with drilling fluids - II. Semi-analytical solution to predict borehole breakdown pressure. International Journal of Rock Mechanics and Mining Sciences and Geomechanics Abstracts, Volume 33, Issue 1, pp. 53 – 69, January 1996.

Morita, N., and Fuh, G.F. Parametric Analysis of Wellbore-Strengthening Methods From Basic Rock Mechanics. SPE Journal of Drilling and Completion, Volume 27, Issue 2, pp. 315 – 327, June 2012.

Okland, D., Gabrielsen, G. K., Gjerde, J., Koen, S., and Williams, E. L. The Importance of Extended Leak-Off Test Data for Combatting Lost Circulation. Paper presented at the SPE/ISRM Rock Mechanics Conference, Irving, Texas, USA. 20 – 23 October, 2002.

Onyia, E.C. Experimental Data Analysis of Lost Circulation Problems During Drilling With Oil-Based Mud. SPE Journal of Drilling and Completion. Volume 9, Number 1, pp. 25 – 31, March 1994.

Postler, D. P. Pressure Integrity Test Interpretation. Paper presented at the SPE/IADC Drilling Conference and Exhibition, Amsterdam, Netherlands. March 4 – 6, 1997.

Razavi, O., Vajargah, A. K., van Oort, E., Aldin, M., and Patterson, R. How to Effectively Strengthen Wellbores in Narrow Drilling Margin Wells: An Experimental Investigation. Paper presented at the SPE Annual Technical Conference and Exhibition, Houston, Texas, USA. September 28 – 30, 2015.

Razavi, O., Vajargah, A. K., van Oort, E., Aldin, M., and Govindarajan, S. Optimization of Wellbore Strengthening Treatment in Permeable Formations. Paper presented at the SPE Western Regional Meeting, Anchorage, Alaska, USA. May 23 – 26, 2016a.

Razavi, O., Vajargah, A. K., van Oort, E., Aldin, M., and Govindarajan, S. Initiation and Propagation of Drilling Induced Fractures. Paper presented at the ARMA Geomechanics Symposium, Houston, Texas, USA. June 26 – 29, 2016b.

Rummel, F. and Winter, R. B. Fracture Mechanics as Applied to Hydraulic Fracturing Stress Measurements. Journal of Earthquake Prediction Research. Volume 2, pp. 33 – 45, 1983.

Rummel, F. Fracture Mechanics Approach to Hydraulic Fracturing Stress Measurements. Fracture Mechanics of Rock, edited by B. K. Atkinson, pp. 217 – 239. 1987.

Sanders, M., Young, S. and Friedheim, J.E. Development and Testing of Novel Additives for Improved Wellbore Stability and Reduced Losses. Paper presented at the AADE Fluids Conference and Exhibition, Houston, Texas, USA. April 8 – 9, 2008.

van Oort, E., Browning, T., Butler, F., Lee, J. and Friedheim, J. Enhanced Lost Circulation Control through Continuous Graphite Recovery. Paper presented at the AADE National Technical Conference and Exhibition, Houston, Texas, USA. April 10 – 12, 2007.

van Oort, E. and Vargo, R. Improving Formation Strength Tests and Their Interpretation. SPE Journal of Drilling and Completion. Volume 23, Number 3, pp. 284 – 294. September 2008.

van Oort, E., Friedheim, J., Pierce, T., and Lee, J. Avoiding Losses in Depleted and Weak Zones by Constantly Strengthening Wellbores. SPE Journal of Drilling and Completion. Volume 26, Number 4, pp. 519 – 530. December 2011.

van Oort, E. and Razavi, S. O. Wellbore Strengthening and Casing Smear: The Common Underlying Mechanism. Paper presented at the IADC/SPE Drilling Conference and Exhibition, Fort Worth, Texas, USA. March 4 – 6, 2014.

van Oort, E., Hoxha, B. B., Yang, L., and Hale, A. Automated Drilling Fluid Analysis using Advanced Particle Size Analyzers. Paper presented at the IADC/SPE Drilling Conference and Exhibition, Fort Worth, Texas, USA. March 1 – 3, 2016.

Vickers, S., Cowie M., Jones T., Twynam A. A new methodology that surpasses current bridging theories to efficiently seal a varied pore throat distribution as found in natural reservoir formations. Paper presented at the AADE Fluids Conference and Exhibition, Houston, Texas, USA. April 11 – 12, 2006.

Zender, C. Particle Size Distributions: Theory and Application to Aerosols, Clouds, and Soils. 2000.

Zhang, J., Alberty, M., Blangy, J.P. A Semi-Analytical Solution for Estimating the Fracture Width in Wellbore Strengthening Applications. Paper presented at the SPE Deepwater Drilling and Completion Conference, Galveston, Texas, USA. September 14 – 15, 2016.

List of Publications

Conference Papers

1. Razavi, O., Vajargah, A. K., van Oort, E., Aldin, M., and Govindarajan, S. Initiation and Propagation of Drilling Induced Fractures. Paper presented at the ARMA Geomechanics Symposium, Houston, Texas, USA. June 26 – 29, 2016.
2. Razavi, O., Vajargah, A. K., van Oort, E., Aldin, M., and Govindarajan, S. Optimization of Wellbore Strengthening Treatment in Permeable Formations. Paper presented at the SPE Western Regional Meeting, Anchorage, Alaska, USA. May 23 – 26, 2016.
3. Razavi, O., Vajargah, A. K., van Oort, E., Aldin, M., and Patterson, R. How to Effectively Strengthen Wellbores in Narrow Drilling Margin Wells: An Experimental Investigation. Paper presented at the SPE Annual Technical Conference and Exhibition, Houston, Texas, USA. September 28 – 30, 2015.
4. van Oort, E. and Razavi, S. O. Wellbore Strengthening and Casing Smear: The Common Underlying Mechanism. Paper presented at the IADC/SPE Drilling Conference and Exhibition, Fort Worth, Texas, USA. March 4 – 6, 2014.

Journal Papers

1. Razavi, O., Vajargah, A. K., van Oort, E., Aldin, M., and Govindarajan, S. Optimum Particle Size Distribution Design for Lost Circulation Control and Wellbore Strengthening. Paper submitted to the Journal of Natural Gas Science and Engineering.
2. Razavi, O., Vajargah, A. K., van Oort, E., Aldin, M., and Patterson, R. How to Effectively Strengthen Wellbores in Narrow Drilling Margin Wells: An Experimental Investigation. Paper submitted to the SPE Drilling and Completion Journal.

3. Razavi, O., Vajargah, A. K., van Oort, E., Aldin, M., and Govindarajan, S. Optimization of Wellbore Strengthening Treatment in Permeable Formations. Paper submitted to the SPE Drilling and Completion Journal.

Vita

Seyed Omid Razavi graduated from Kamal High School in Tehran, Iran, in 2003. Subsequently, he was admitted to Sharif University of Technology in Tehran, Iran. He received a Bachelor of Science in 2008 and a Master of Science in 2011 in Civil Engineering. In the fall of 2011, he entered the Graduate School of The University of Texas at Austin to pursue his Doctor of Philosophy in Civil Engineering.

Permanent Address: omid.razavi@utexas.edu

This dissertation was typed by Seyed Omid Razavi.